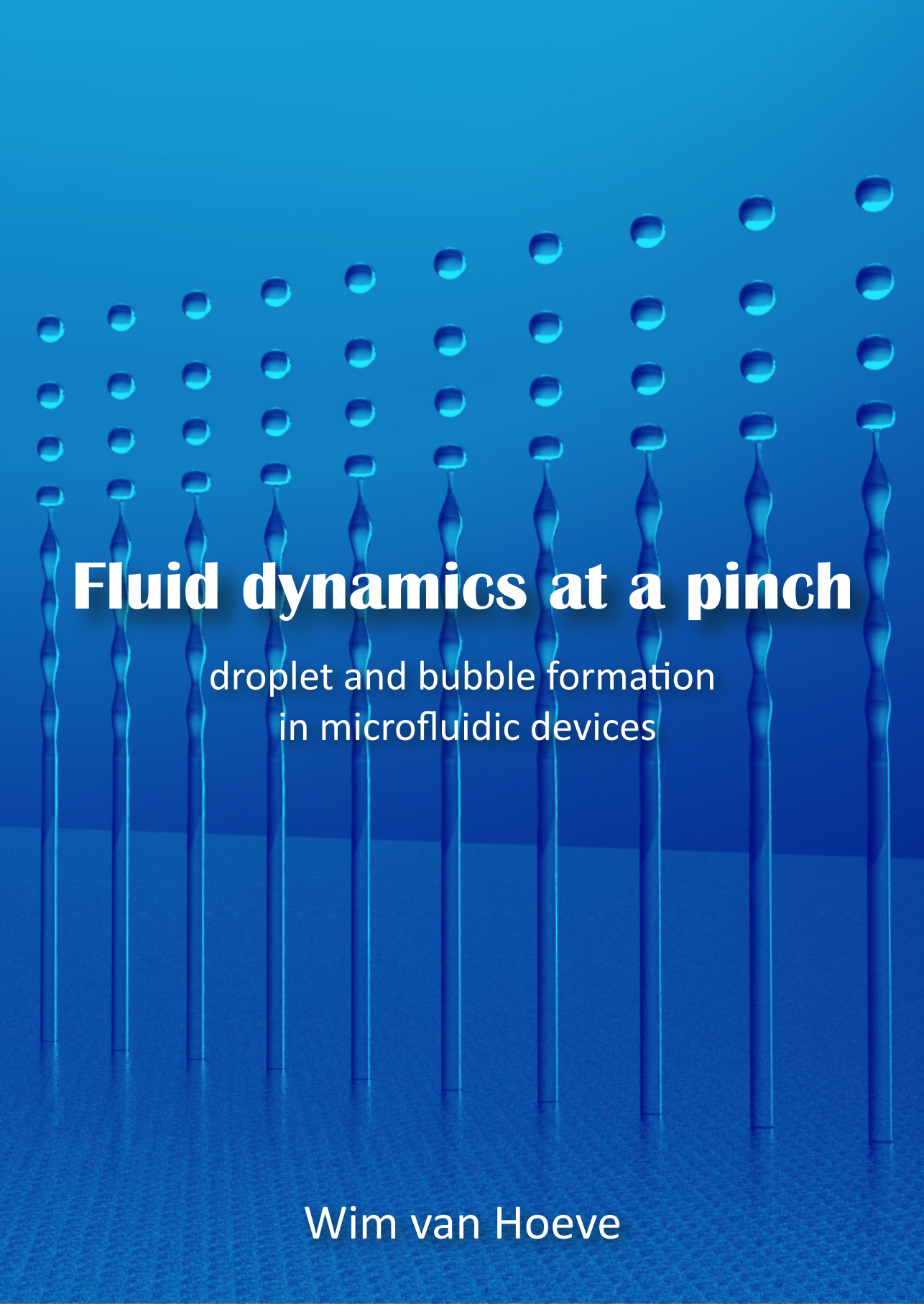

Fluid dynamics at a pinch

droplet and bubble formation
in microfluidic devices

Wim van Hoeve

FLUID DYNAMICS AT A PINCH: DROPLET AND BUBBLE FORMATION IN MICROFLUIDIC DEVICES

Wim van Hoeve

Ph.D. committee

Chairman and secretary	
prof. dr. G. van der Steenhoven	University of Twente
Supervisor	
prof. dr. D. Lohse	University of Twente
Assistant-supervisor	
dr. A. M. Versluis	University of Twente
Members	
prof. dr. ir. A. van den Berg	University of Twente
prof. dr. M. C. Elwenspoek	University of Twente
prof. dr. M. P. Brenner	Harvard University
dr. ir. J. C. M. Marijnissen	Delft University of Technology
ir. J. M. Wissink	Medspray XMEMS bv

The research described in this thesis was performed at the Physics of Fluids group of the Faculty of Science and Technology of the University of Twente. It was partially funded by the MicroNed technology program of the Dutch Ministry of Economic Affairs through its agency SenterNovem under grant Bsik-03029.5, and by the Netherlands Organisation for Scientific Research (NWO) via the Spinoza Prize awarded to prof. dr. Detlef Lohse in 2005.

Cover:
A stylized visualization of the breakup of liquid microjets into droplets (see Chap. 6).

Dutch title:
Vloeistof dynamica in het klein: druppel- en belformatie in microfluïdische systemen

Publisher:
Wim van Hoeve, Physics of Fluids, University of Twente
P.O. Box 217, 7500 AE Enschede, The Netherlands
w.vanhoeve@gmail.com

Ph.D. Thesis, University of Twente
Printed by Gildeprint Drukkerijen
ISBN 978-90-365-3161-0

FLUID DYNAMICS AT A PINCH: DROPLET AND BUBBLE FORMATION IN MICROFLUIDIC DEVICES

PROEFSCHRIFT

ter verkrijging van
de graad van doctor aan de Universiteit Twente,
op gezag van de rector magnificus,
prof. dr. H. Brinksma
volgens besluit van het College voor Promoties
in het openbaar te verdedigen
op 23 maart 2011 om 16:45 uur

door

Willem van Hoeve

geboren op 27 april 1980
te Noordoostpolder

Dit proefschrift is goedgekeurd door de promotor:

prof. dr. D. Lohse

en de assistent-promotor:

dr. A. M. Versluis

Contents

Chapter 1 Introduction

A liquid jet emanating from an orifice, such as a kitchen faucet, spontaneously breaks up into droplets by the action of surface tension forces. This phenomenon has fascinated scientists for many centuries. As early as 1833 Savart[1] experimentally studied droplet formation from the breakup of a liquid jet and obtained a remarkably accurate picture of this process using his naked eye alone (see Fig. 1.1). Savart was the first to recognize that the shape of a droplet in air is preferentially spherical because of mutual attraction between molecules that force the liquid in its most compact shape, a sphere. A basic understanding of the action of surface tension forces was already present since the work of Young and Laplace, yet its crucial role in driving the breakup was only recognized by Plateau in 1849. Plateau found that a cylindrical liquid jet, that is affected by surface tension forces, is unstable against surface perturbations whose wavelength exceed the jet's circumference. Rayleigh treated the breakup of the jet as a dynamical problem and showed that, based on a linear stability analysis, the breakup of an inviscid liquid jet under laminar flow conditions is controlled by the fastest growing wave perturbation.[3] The fastest growing wave with wavelength $\lambda_{\mathrm{opt}} = 2\sqrt{(2)}\pi r_{\mathrm{j}}$ is the optimum wavelength for jet breakup and governs the droplet size $(4/3)\pi r_{\mathrm{d}}^3 = \lambda_{\mathrm{opt}}\pi r_{\mathrm{j}}^2$, with r_{d} and r_{j} the radius of the droplet and the radius of the jet respectively. Hence, for a given liquid, the size of the droplets can be predicted based on the systems dimensions

Figure 1.1: A figure from Savart's original paper of 1833 is reproduced here.[1,2] This sketch depicts the spontaneous breakup of a 6 mm diameter water jet into droplets. The time scale on which the breakup takes place is very short $\tau_{\mathrm{cap}} \approx 20$ ms. The arrow indicates the location of droplet pinch-off.

only, namely $r_\mathrm{d} = 1.89 r_\mathrm{j}$.

There is substantial academic and industrial interest in the mechanisms that lead to the production of precisely controlled droplets (and bubbles) with a narrow size distribution. In inkjet printing monodisperse microdroplets are required for high-resolution printing of various materials in patterns on a substrate, *e.g.* for graphics printing, printing of flexible electronics, microdispensing of biochemicals, and 3D rapid prototyping.[4] In the food industry the production of powders with a monodisperse particle size distribution through spray-drying results in a reduction of transportation and energy costs. In drug inhalation technology microdroplets with a narrow size distribution can be more efficiently targeted to the smallest alveoli in the lungs which improves therapeutic efficiency. This has the advantage that the total dose can be lowered, reducing potential side-effects. In diagnostic ultrasound imaging, the resonance frequency of the contrast bubble and the insonation frequency are matched to increase the total acoustic response. The resonance frequency of a (medical) bubble is strongly governed by its size—a narrow size distribution results in a narrow bandwidth of the acoustic response, and consequently, leads to an improved contrast between the blood flow through the vessels and the surrounding tissue.

Various microfluidic techniques exist to produce these sophisticated dispersions. Microfluidics deals with the precise control of fluids flowing through minuscule channels, typically the thickness of a human hair ($100\,\mu$m). In general, it can be classified in two different groups: continuous flow and two-phase microfluidics. Two-phase microfluidic networks offer convenient methods to disperse a fluid, a liquid or a gas, into a continuous fluid to generate monodisperse microdroplets or microbubbles.[5] The dispersion can be classified based on the nature of the dispersed and the continuous fluid in sprays, emulsions, or gas dispersions, for droplets in air, liquid droplets in an immiscible liquid, or gas bubbles in a liquid respectively.

An elegant way to generate a fine spray of droplets is to force a liquid through a microscopically small orifice to form a liquid jet that spontaneously breaks up into monodisperse microdroplets. One of the great advantages of this passive process is its ease of use and its low production costs, which means it is used as a disposable device in a wide variety of consumer products. An example of such an atomizer chip can be seen in Fig. 1.2. More sophisticated techniques exist, where the breakup of the jet is stimulated by applying a periodic perturbation imposed by, for example, a

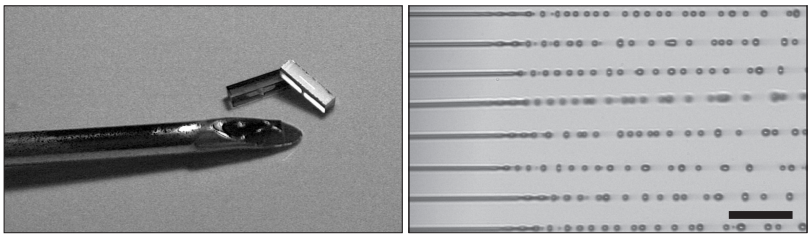

Figure 1.2: (left) The Medspray atomizer chip is fixed in the tip of a needle for experimental flow visualization purposes. The atomizer chip consists of a row of 1 μm-radius orifices from which liquid jets emanate that break-up into droplets. (right) High-speed microscope photograph of the breakup of the jets captured with a high-resolution camera and ultra-short flash illumination with a 10 ns pulse duration. The relevant time scale $\tau_{\mathrm{cap}} = 200$ ns. The scale bar denotes 50 μm.

pressure pulse from a piezoelectric actuator or a thermal shock from a heating element. These techniques can be found in continuous inkjet technology to produce a continuous stream of droplets. In drop-on-demand technology a precisely controlled amount of liquid is forced through an orifice by means of a piezoelectric element to form a single droplet. In electrospray atomization high voltage is applied to form a Taylor cone from which a tiny jet emanates and breaks up into a continuous stream of charged droplets.

Microfluidic devices with a T-shaped,[6–9] co-flow,[10] or flow-focusing geometry[11–14] have proven to be a versatile tool for highly controlled formation of monodisperse gas dispersions and emulsions utilizing passive processes.[14–19] T-shaped microfluidic devices allow for a dispersed phase to be injected into an immiscible cross-flow. In co-flow devices the inner phase is injected in a co-flowing liquid stream, whereas in flow-focusing both streams are focused through a narrow constriction in which droplet pinch-off occurs. Examples of these three geometries used in experiments are depicted in Fig. 1.3.

The use of planar microfluidic devices made of polydimethylsiloxane (PDMS) has become standard since the work of Duffy *et al.*[22] and McDonald *et al.*[23] Soft-lithography and micromolding techniques offer convenient and fast methods to imprint networks of rectangular microchannels with uniform channel depth in PDMS. One of the great advantages of the use of PDMS is the material's transparency that makes direct visualization of the droplet or bubble formation process possible. However, direct visualization of the formation process, *i.e.* the dynamics of the pinch-off, is extremely difficult due to the small length and time scales typically in-

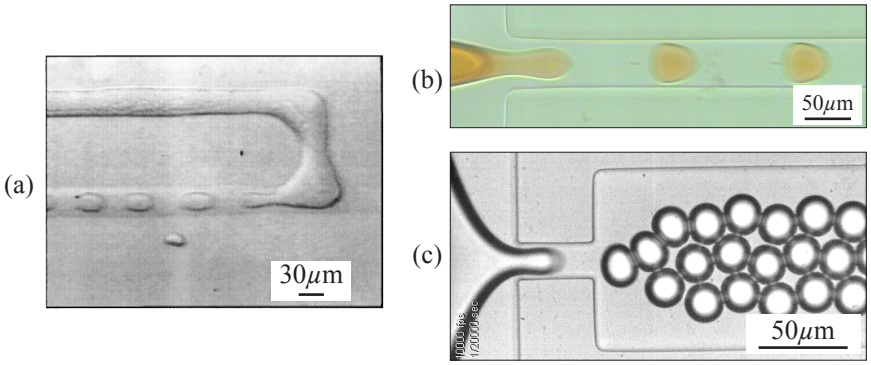

Figure 1.3: The three most frequently used microfluidic systems for the formation of droplet and bubbles. Water-in-oil droplet formation at a T-shaped junction [6] and in a co-flow structure [20] in (a) and (b) respectively. Bubble formation in a flow-focusing device in (c). [21]

volved in microfluidic research. Whereas the detachment of a macroscopic droplet, *e.g.* from a dripping faucet, can be observed with the naked eye, dedicated high-speed imaging systems are required to capture the pinch-off of a microscopically small droplet. Experimental observations of the actual pinch-off of a droplet is very difficult, since the time scale involved in the breakup dynamics is extremely short. The relevant time scale for the breakup of a liquid jet is given by the capillary time $\tau_{\mathrm{cap}} = \sqrt{\rho r_{\mathrm{d}}^3/\gamma}$, with liquid density ρ and surface tension γ. This implies that for the formation of a 0.5 pl droplet (equivalent to a 5-μm radius droplet) the relevant time scale is as small as 1 μs. Note that this is four orders of magnitude smaller than compared to the time scale involved in Savart's experiments back in the year 1833.

The two key questions addressed in this thesis concern ultra high-speed microscopic imaging of microbubble pinch-off in planar microfluidic devices and droplet formation from the breakup of microscopically small liquid jets. The ultimate goal is to understand the physical mechanisms that lead to controlled droplet and bubble formation.

1.1 Guide through the thesis

The aim of the various studies described in this thesis is to investigate passive methods that lead to the controlled formation of monodisperse mi-

crodroplets and microbubbles in microfluidic devices.

In *Chapter 2* we study the role of the channel geometry on the bubble pinch-off in flow-focusing devices. This was done through the fabrication of PDMS devices with different channel dimensions. The time evolution of the minimum radius of the gaseous neck was obtained experimentally using high-speed imaging. For low aspect ratio channels, where the channel height is much smaller than the channel width, we uncover two regimes of the collapse, namely, a quasi two-dimensional lateral collapse followed by an extremely fast 3D pinch-off.

In *Chapter 3* we study the ultimate stage of bubble pinch-off at higher spatial and temporal resolution within a square cross-sectional flow-focusing channel. The camera's wide field of view enabled us to capture the complete shape of the bubble. We show that both the radial and axial length scales of the neck play an important role during the final stage of pinch-off.

A new regime of microbubble formation through jetting in co-flow devices is shown in *Chapter 4*. The strong pressure gradient in the entrance region of the channel gives rise to thin gaseous jet that breaks up into bubbles with a size that is typically much smaller than the channel dimensions. We show that the size of the bubbles can be accurately predicted based on the flow development in the channel.

In *Chapter 5* a prediction for the size of droplets and bubbles formed from the breakup of the inner jet in a co-flowing stream is presented. We study two distinct cases. In the first case we study droplet formation in two fully developed co-flowing liquid streams with finite viscosity. In the second case we consider bubble formation from the breakup of a 'hollow jet' where the inner gas viscosity is neglected.

In *Chapter 6* we study the phenomena of jet breakup and droplet formation for fluids that are jetted from an array of micron-sized orifices. We characterize the fluidic behavior of the jet during breakup and beyond using high-speed imaging. We also model the behavior of the jet during breakup and beyond using a 1D mathematical model that is based on the lubrication approximation. We validate the model and demonstrate that it accurately predicts the size and velocity of the primary droplets as well as the existence of satellite droplets.

A synopses of each chapter's results and the general conclusions of this thesis can be found in *Chapter 7*.

References

[1] F. Savart, "Mémoires sur la constitution des veines liquides. lancées par des orifices circulaires en mince paroi," *Annal. Chim.* **53**, 337–386 (with additional plates in vol. 54) (1833).

[2] J. Eggers, "A brief history of drop formation," in *Nonsmooth Mechanics and Analysis*, Advances in Mechanics and Mathematics, Vol. 12, edited by P. Alart, O. Maisonneuve, and R. T. Rockafellar (Springer, US, 2006) pp. 163–172.

[3] Lord Rayleigh, "On the capillary phenomena of jets," *Proc. R. Soc. London* **29**, 71–97 (1879).

[4] M. Singh, H. M. Haverinen, P. Dhagat, and G. E. Jabbour, "Inkjet printing-process and its applications," *Adv. Mater.* **22**, 673–685 (2010).

[5] T. Squires and S. R. Quake, "Microfluidics: Fluid physics at the nanoliter scale," *Rev. Mod. Phys.* **77**, 977–1026 (2005).

[6] T. Thorsen, R. W. Roberts, F. H. Arnold, and S. R. Quake, "Dynamic pattern formation in a vesicle-generating microfluidic device," *Phys. Rev. Lett.* **86**, 4163–4166 (2001).

[7] P. Garstecki, M. J. Fuerstman, H. A. Stone, and G. M. Whitesides, "Formation of droplets and bubbles in a microfluidic T-junction-scaling and mechanism of break-up," *Lab Chip* **6**, 437–446 (2006).

[8] V. van Steijn, C. R. Kleijn, and M. T. Kreutzer, "Flows around confined bubbles and their importance in triggering pinch-off," *Phys. Rev. Lett.* **103**, 214501 (2009).

[9] V. van Steijn, C. R. Kleijn, and M. T. Kreutzer, "Predictive model for the size of bubbles and droplets created in microfluidic T-junctions," *Lab Chip* **10**, 2513–2518 (2010).

[10] E. Castro-Hernández, W. van Hoeve, D. Lohse, and J. M. Gordillo, "Microbubble generation in a co-flow device operated in a new regime," Under review.

[11] A. M. Gañán-Calvo and J. M. Gordillo, "Perfectly monodisperse microbubbling by capillary flow focusing," *Phys. Rev. Lett.* **87**, 274501 (2001).

[12] S. L. Anna, N. Bontoux, and H. A. Stone, "Formation of dispersions using "flow focusing" in microchannels," *Appl. Phys. Lett.* **82**, 364–366 (2003).

[13] R. Dreyfus, P. Tabeling, and H. Willaime, "Ordered and disordered patterns in two-phase flows in microchannels," *Phys. Rev. Lett.* **90**, 144505 (2003).

[14] P. Garstecki, H. A. Stone, and G. M. Whitesides, "Mechanism for flow-rate controlled breakup in confined geometries: A route to monodisperse emulsions," *Phys. Rev. Lett.* **94**, 164501 (2005).

[15] E. Talu, M. M. Lozano, R. L. Powell, P. A. Dayton, and M. L. Longo, "Long-term stability by lipid coating monodisperse microbubbles formed by a flow-focusing device," *Langmuir* **22**, 9487–9490 (2006).

[16] K. Hettiarachchi, E. Talu, M. L. Longo, P. A. Dayton, and A. P. Lee, "On-chip generation of microbubbles as a practical technology for manufacturing contrast agents for ultrasonic imaging," *Lab Chip* **7**, 463–468 (2007).

[17] G. F. Christopher and S. L. Anna, "Microfluidic methods for generating continuous droplet streams," *J. Phys. D: Appl. Phys.* **40**, R319–R336 (2007).

[18] A. Nazir, C. G. P. H. Schroën, and R. M. Boom, "Premix emulsification: A review," *J. Membr. Sci.* **362**, 1–11 (2010).

[19] C. N. Baroud, F. Gallaire, and R. Dangla, "Dynamics of microfluidic droplets," *Lab Chip* **10**, 2032–2045 (2010).

[20] A. G. Marín, W. van Hoeve, L. Shui, J. C. T. Eijkel, A. van den Berg, and D. Lohse, "The microfluidic thunderstorm," in *Bull. Am. Phys. Soc.* **55**, BAPS.2010.DFD.GM.3 (2010).

[21] Benjamin Dollet, Wim van Hoeve, Jan-Paul Raven, Philippe Marmottant, and Michel Versluis, "Role of the channel geometry on the bubble pinch-off in flow-focusing devices," *Phys. Rev. Lett.* **100**, 034504 (2008).

[22] D. C. Duffy, J. C. McDonald, O. J. A. Schueller, and G. M. Whitesides, "Rapid prototyping of microfluidic systems in poly(dimethylsiloxane)," *Anal. Chem.* **70**, 4974–4984 (1998).

[23] J. C. McDonald, D. C. Duffy, J. R. Anderson, D. T. Chiu, H. Wu, O. J. A. Schueller, and G. M. Whitesides, "Fabrication of microfluidic systems in poly(dimethylsiloxane)," *Electrophoresis* **21**, 27–40 (2000).

Chapter 2 Role of the channel geometry on the bubble pinch-off in flow-focusing devices[§]

Abstract

The formation of bubbles by flow focusing of a gas and a liquid in a rectangular channel is shown to depend strongly on the channel aspect ratio. Bubble breakup consists in a slow linear 2D collapse of the gas thread, ending in a fast 3D pinch-off. The 2D collapse is predicted to be stable against perturbations of the gas/liquid interface, whereas the 3D pinch-off is unstable, causing bubble polydispersity. During 3D pinch-off, a scaling $w_{\mathrm{m}} \propto \tau^{1/3}$ between the neck width w_{m} and the time τ before breakup indicates that breakup is driven by the inertia of both gas and liquid, not by capillarity.

2.1 Introduction

The production of monodisperse microbubbles is a crucial issue in microfluidics,[1,2] driven by applications in food processing, pharmaceutical sciences, and medicine, for example for targeted drug delivery with ultrasound contrast agent microbubbles.[3] Flow-focusing techniques have proven to be powerful and versatile tools to achieve monodisperse drops and bubbles. Their working principle is based on a co-flow of an internal gas phase and an external liquid phase through a constriction, where the gas is pinched off by the co-flowing liquid to release bubbles. Various groups have used flow-focusing to produce monodisperse bubbles[4–7] and foams.[8,9] In most cases, low-cost soft lithography techniques[10,11] are used: the produced channels are then rectangular.

Despite the wide use of flow focusing, the precise influence of the channel

[§]Published as: B. Dollet, W. van Hoeve, J.-P. Raven, P. Marmottant, and M. Versluis, "Role of the channel geometry on the bubble pinch-off in flow-focusing devices," *Physical Review Letters* **100**, 034504 (2008).

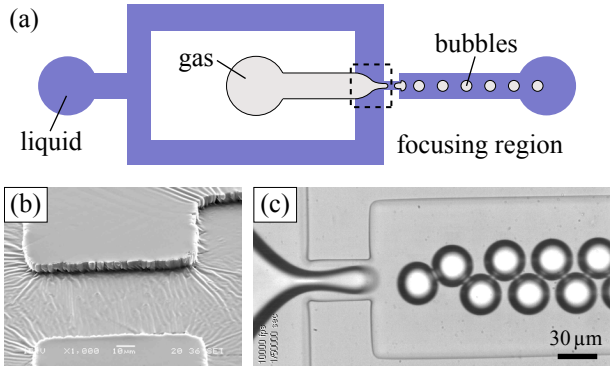

Figure 2.1: (a) Sketch of the flow-focusing setup. (b) Scanning Electron Micrograph of the imprint in the PDMS slab of the channel of width 30 μm and height 6 μm. (c) Snapshot of the flow-focusing process: the central gas thread is squeezed by the surrounding liquid flow, releasing monodisperse microbubbles, shaped almost as disks because of the confinement in the third dimension.

geometry on the bubble formation process remains unexplored, even though it ultimately determines the bubble characteristics: size, polydispersity and formation frequency. In this chapter, we clarify this issue by characterizing in detail the various stages of the formation process, notably the fast final breakup, for different rectangular channel cross-sections, from an elongated rectangle to a square.

2.2 Experimental results

Flow-focusing devices consists of two inlet channels, one for the liquid and one for the gas, which converge to a narrow channel followed by an outlet channel (Fig. 2.1a). We produced the devices by soft lithography techniques: a mold was created from a negative photosensitive material (SU-8 GM1060, Gersteltec SARL) spin-coated on a silicon oxide substrate, to imprint (Fig. 2.1b) a reticulable polymer layer (PDMS, Sylgard 184, Dow Corning), which was then bonded to a glass cover plate in a plasma cleaner. Two holes of diameter 1.0 mm were drilled in the glass, to connect the inlet channels with teflon tubes of outer diameter 1.06 mm, through which gas and liquid were supplied. Pressurized nitrogen was used, and its overpressure, kept constant at 0.7 bar, was controlled by a pressure regulator (PRG101-25, Omega, regulation accuracy 0.1%) connected to a pressure sensor (DPG1000B-30G, Omega). The liquid used was a 10% solution of

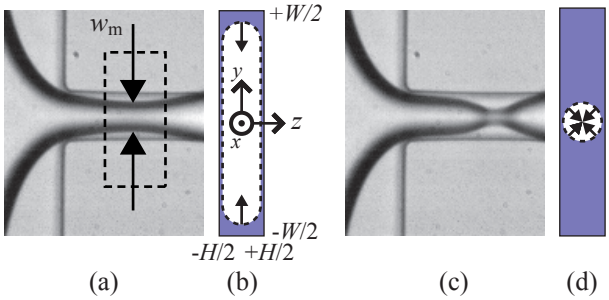

Figure 2.2: Snapshots of the gas thread in two regimes of collapse described in the text.[†] (a) The gas thread is first squeezed inwards from the sides by the surrounding liquid; w_m is its minimal width in the processed region (white dashed rectangle). This regime is sketched in cross-section in (b). The gas thread experiences finally a fast pinch-off (c), where it is squeezed radially in the cross-section (d).

dish-washing liquid (Dreft, Procter & Gamble) in deionized water, which wets optimally the channel walls.[8] It has a volumetric mass $\rho = 10^3\,\mathrm{kg/m^3}$, a surface tension $\gamma = 0.03\,\mathrm{N/m}$ and a viscosity $\eta = 10^{-3}\,\mathrm{Pa{\cdot}s}$. The liquid flow rate was controlled by a syringe pump (PHD 22/2000, Harvard Apparatus, flow rate reproducibility 0.05%). The setup was placed under a microscope (Axiovert 40 CFL, Carl Zeiss) with a 40× objective, which was connected to a high-speed camera (Photron Ultima APX-RS). The camera provides 512×512 pixel images (field of view $240 \times 240\,\mu\mathrm{m}$) at 10,000 frames per second (fps), to image the bubbles in the outlet channel (Fig. 2.1c), and 32×128 pixel images (field of view $15 \times 60\,\mu\mathrm{m}$) at $180,000\,\mathrm{fps}$ (with an exposure time of $5.6\,\mu\mathrm{m}$), to resolve the bubble formation and the pinch-off in the channel (Fig. 2.2). We quantified the collapse leading to breakup by the minimum width w_m of the gas thread (Fig. 2.2a) and we followed its decrease until pinch-off. Actually, the collapse is preceded by a phase during which the gas thread penetrates and fills the channel; we do not study this phase in this chapter. We used three different channels of length $50\,\mu\mathrm{m}$, with different aspect ratios for the rectangular cross-section: a long rectangle (case a, width $W = 30\,\mu\mathrm{m}$ and height $H = 6\,\mu\mathrm{m}$, see Fig. 2.1b), a short rectangle (case b) with a width ($W = 30\,\mu\mathrm{m}$) comparable to its height ($H = 20\,\mu\mathrm{m}$), and a square (case c, $W = H = 20\,\mu\mathrm{m}$).

[†]See EPAPS Document No. E-PRLTAO-100-059802 for a recording at 50,000 frames per second of a single collapse of the gas thread in the orifice of a flow-focusing device. For more information on EPAPS, see http://www.aip.org/pubservs/epaps.html.

We plot for the three geometries the variation of w_m during collapse, until breakup, in Fig. 2.3. We identify two regimes: first, w_m decreases linearly with time. We call this regime the 2D collapse, since w_m remains bigger than the channel height, which means that the gas thread is squeezed inwards from the sides (Fig. 2.2b). The linear decrease has been studied before:[7] at this stage, the gas thread constricts the channel, and the liquid flowing at imposed flow rate Q_ℓ is forced to squeeze the gas thread at speed $\mathrm{d}w_\mathrm{m}/\mathrm{d}t \propto Q_\ell$, independently from the gas pressure, the liquid viscosity and the surface tension. Second, there is a transition from the linear decrease of w_m to a fast final pinch-off (Fig. 2.2c). This happens precisely for $w_\mathrm{m} = H$ (within less than 5%): hence, we call this regime the 3D collapse, since the gas thread can be squeezed along any direction (Fig. 2.2d). Fig. 2.3 also shows that the duration of the 3D collapse is about $20\,\mu$s, with no significant dependence on the cross-section dimensions, contrary to the 2D collapse which, as expected, becomes longer with increasing aspect ratio W/H, and is absent for the square channel (Fig. 2.3c).

Garstecki *et al.*[7] have suggested that the collapse proceeds through a series of equilibria, and justified it on one example, by proving the agreement between experiment and the corresponding computation with surface energy minimization. We now propose a more general stability analysis against perturbations of the gas/liquid interface, suggesting that the 2D collapse is *always* stable, whereas the 3D collapse is *always* unstable. To determine qualitatively the influence of the channel confinement on the stability of both 2D and 3D collapses, we study the linear stability of the gas thread against perturbations of its interface in two simplified channel cross-sections: a rectangle with $W \gg H$, and a circular tube, simpler than a square channel and allowing for squeezing of the gas thread along any direction, which is the essential ingredient of the 3D collapse.

In the rectangular geometry, we assume that the cross-section of the gas thread is, as depicted in Fig. 2.2b, a rectangle of dimensions $w_0 \times H$, bounded with two half-circles of radius $H/2$. We thus neglect the thickness of the lubrication films between the gas thread and the channel walls,[12] which is equivalent to assume $\mathrm{Ca}^{2/3} \ll 1$ with the capillary number $\mathrm{Ca} = \eta v_0/\gamma$. In our experiments, the typical velocity v_0 is lower than 3 m/s, thus $\mathrm{Ca}^{2/3} < 0.2$. We also assume that the fluid flow follows the Hele-Shaw approximation: the spatial variations in the flow along z are much faster than along x and y (see Fig. 2.2b for the definition of the axes), which holds if $W - w_0 \gg H$. Then the velocity becomes $\vec{v}(x, y, z) =$

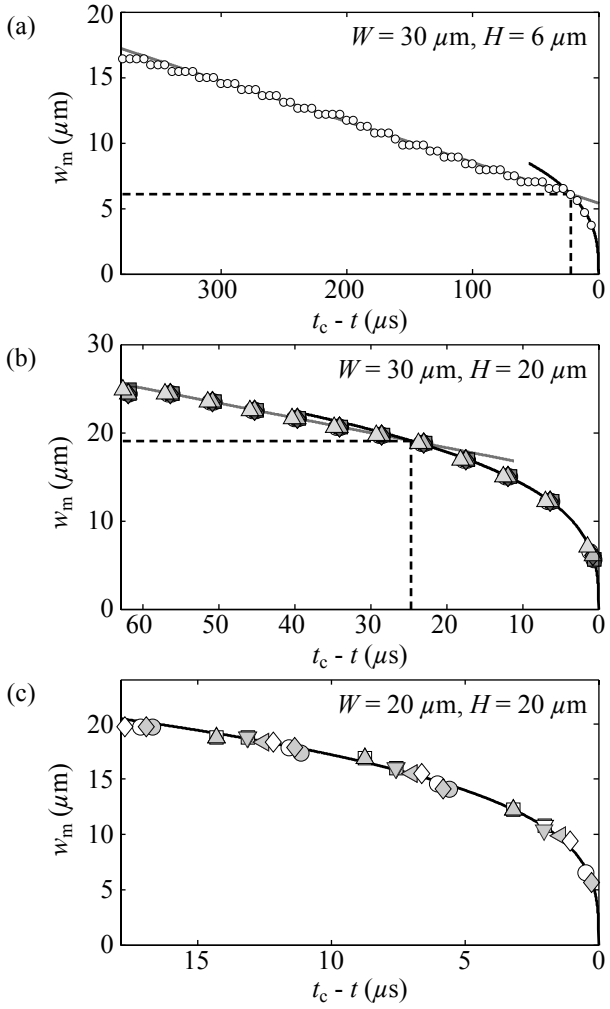

Figure 2.3: Evolution of the minimum width of the gas thread w_{m} as a function of the time $\tau = t_{\mathrm{c}} - t$ remaining until final breakup, for the following cross-sections ($W \times H$, both in μm) (a) 30×6, (b) 30×20, (c) 20×20. The liquid flow rates are (a) 20, (b) 20 and (c) $70\,\mu$l/min. Each curve results from the superposition of independent events (indicated by different symbols in cases b and c), which collapse on the same master curve, showing the excellent reproducibility of the system. The two regimes described in the text correspond to different fits: first a linear one, and then a power law. Dashed lines in (a) and (b) indicate the transition between the two regimes, where the fitting curves intersect. The transition value between 2D and 3D collapses is $6.1\,\mu$m in case a ($H = 6\,\mu$m), and $19.1\,\mu$m in case b ($H = 20\,\mu$m). The instant of this transition gives the duration $\tau_{3\mathrm{D}}$ of the 3D collapse: $22\,\mu$s in case a, $25\,\mu$s in case b and $19\,\mu$s in case c.

$(1-4z^2/H^2)\vec{u}(x,y)$, and averaging the Navier-Stokes equation in the gap gives:[13] $\rho\frac{\partial\vec{u}}{\partial t}+\frac{6}{5}\rho(\vec{u}\cdot\vec{\nabla})\vec{u}=-\vec{\nabla}p-\frac{12\eta}{H^2}\vec{u}$. Without the convection term, this equation is the well-known Darcy law. The ratio between the convective and viscous terms gives a Reynolds number $\mathrm{Re}\approx H^2u/10\nu W$, with W the characteristic length for the spatial variations of the gap-averaged velocity, and $\nu=\eta/\rho$ the kinematic viscosity. We evaluate Re for the dimensions of our elongated rectangular channel: $H=6\,\mu$m, $W=30\,\mu$m, and since $u<3\,$m/s in our experiments, we compute $\mathrm{Re}<0.4$. We thus use Darcy law in the subsequent analysis.

We assume that the unperturbed flow is at constant velocity $\vec{u}=u_0\vec{e}_x$, and compute the growth rate of a small perturbation of the interface of the form: $w(x,t)=w_0+\varepsilon\,\mathrm{Re}(e^{ikx+\sigma t})$, with k real.[‡]For this, we express $\vec{u}$ and p, using as boundary conditions the continuity of velocity at the interface: $\partial w/\partial t=v_y-v_x\partial w/\partial x$, and the continuity of normal stresses: $p=-\gamma\mathcal{C}$ (Laplace pressure), with $\mathcal{C}\simeq 2/H-\partial^2w/\partial x^2$ the interfacial curvature, assuming $k\varepsilon\ll 1$. To close the system, we express mass conservation as: $\partial Q_\ell/\partial x=2H\partial w/\partial t$, with the flow rate $Q_\ell=2\int_{-H/2}^{H/2}\mathrm{d}z\int_{w_0/2}^{W/2}\mathrm{d}y\,\vec{v}$. The growth rate is then the solution of the dispersion relation:

$$\left(\sigma+\frac{12\nu}{H^2}\right)\left[\frac{\sigma}{k}(1+\xi^2)-2iu_0\xi^2\right]+\frac{2\gamma k^2\xi}{\rho}=0, \tag{2.1}$$

where $\xi=\tanh k(W-w_0)$. It is easy to prove from this relation that the real part of the growth rate is always negative: hence, the 2D collapse is always stable.

To study the stability analysis in a 3D, axisymmetric case, we start from a gas thread of constant radius r_0 in a tube of radius R. The present analysis is therefore a special case of the more general stability analysis of core-annular flows,[14,15] where two fluids flow concentrically in a tube. Guillot *et al.*[16] have recently solved this problem neglecting convection. We adapt their results, neglecting gas viscosity η_g ($\eta_\mathrm{g}/\eta=0.017$ for nitrogen): for a perturbation of the gas thread of the form: $r(x,t)=r_0+\varepsilon\,\mathrm{Re}(e^{ikx+\sigma t})$,

[‡]We now show why we can discard the case of a complex k. From the form of the perturbation, the pressure can be written as: $p(x,y,t)=f(y)\mathrm{Re}(e^{ikx+\sigma t})$. As a consequence of Darcy law, $\Delta p=0$; writing $k=k_r+ik_i$ and $\sigma=\sigma_r+i\sigma_i$, one therefore gets: $0=\partial^2p/\partial x^2+\partial^2p/\partial y^2=[f''(y)+(k_i^2-k_r^2)f(y)]\cos(k_rx+\sigma_it)-2k_rk_i\sin(k_rx+\sigma_it)$. A necessary condition for this equality to hold is $k_ik_r=0$, hence k is real.

we obtain:

$$\sigma = \frac{\gamma}{16\eta R a^5}\left[-\frac{4i\nabla P_0 R^2}{\gamma}a^2(1-a^2)\tilde{k} + (1-4a^2+3a^4-4a^4\ln a)(\tilde{k}^2-\tilde{k}^4)\right], \quad (2.2)$$

with $a = r_0/R$, $\tilde{k} = kr_0$, and $\nabla P_0 = -\partial p/\partial x$ the pressure gradient in the unperturbed case. The growth rate $\mathrm{Re}(\sigma)$ is positive for $0 \leq \mathrm{Re}(\tilde{k}) \leq 1$ and $\mathrm{Im}(\tilde{k}) = 0$: contrary to the 2D case, the 3D collapse is therefore always unstable. The analysis suggests that the gas thread is destabilized as soon as it can be squeezed radially. This is supported by the fact that the transition between 2D and 3D collapses happens exactly for $w_\mathrm{m} = H$ (Fig. 2.3a,b).

We show now that the final breakup is not the result of the growth of a capillary instability. The physical mechanisms driving the 3D collapse can be inferred from the asymptotic behavior of w_m just before breakup.[17] To do so, we now keep only the data in the 3D collapse regime, and plot $\log w_\mathrm{m}$ *versus* $\log \tau$ in Fig. 2.4. All data collapse on power-law master curves, with exponents equal to 0.33±0.03, compatible with a power law of exponent 1/3. Such an exponent was reported for an asymmetric bubble pinch-off,[18,19] and related to a nonzero gas flow in the neck. Here, just as in[18,19], the gas flowing in the neck sucks the surrounding liquid, accelerating the pinch-off compared to the usual bubble pinch-off, where the balance between liquid inertia and surface tension would yield a 1/2 exponent.[20–22] Hence, although our 3D collapse may initiate from a capillary destabilization of the gas thread, it is eventually driven by gas and liquid inertia. Together with the results of Garstecki *et al.*,[7] who showed experimentally that the 2D collapse proceeds at a speed independent from the surface tension, this shows that the *entire* collapse does not depend on surface tension, but solely on the inertia of both liquid and gas.

Finally, we measured the polydispersity of the produced bubbles, by imaging them in the outlet channel at a wider field of view. We measured the area of approximately 100 bubbles, each bubble being measured on 50 images to improve the accuracy. We used as the polydispersity index (PDI) the ratio of the standard deviation to the average of the area. Our measured PDI are $0.1 \pm 0.1\%$ (case a), $0.3 \pm 0.1\%$ (case b) and $1.0 \pm 0.1\%$ (case c), confirming that flow-focusing is an efficient way to produce very monodisperse bubbles. Moreover, the PDI decreases with increasing aspect ratio of the channel cross-section, hence with increasing ratio between the

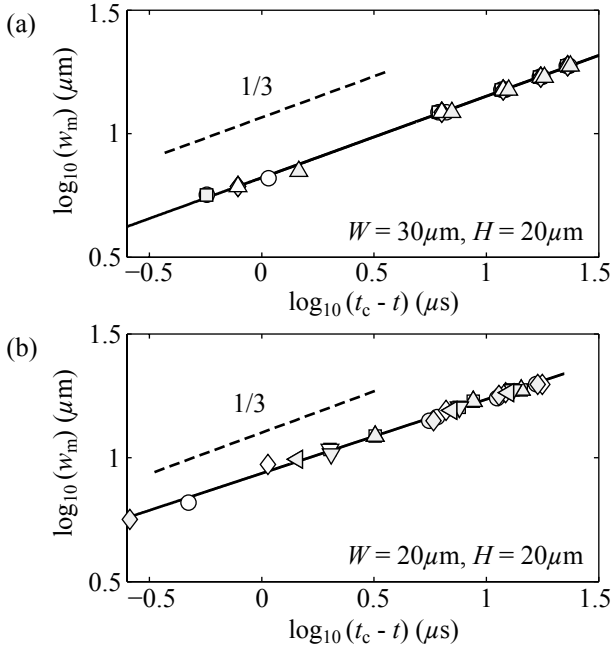

Figure 2.4: Logarithm of the minimum width of the gas thread w_m as a function of the logarithm of the time $t_c - t$ until final breakup. The line represents the best fit of the data: its slope is (a) 0.33 (cross-section $30 \times 20\,\mu m^2$) and (b) 0.30 (cross-section $20 \times 20\,\mu m^2$). Different symbols represent independent experiments. We do not present the results for the channel of cross-section $30 \times 6\,\mu m^2$, for which only three data points are in the 3D collapse regime: in that case, the slope is 0.35.

durations of the 2D and the 3D collapses. Indeed, since the 2D collapse proceeds quasistatically, its reproducibility is only limited by the experimental fluctuations of the gas and the liquid flow rates. On the other hand, the intrinsic unstable nature of the 3D collapse, hence its sensitivity to random fluctuations, limits its reproducibility. More precisely, comparing different pinch-off events in the square and the rectangular ($30 \times 20\,\mu m^2$) channels, we indeed saw a higher standard deviation in pinch-off time (2.8 *versus* 2.0 μs) and pinch-off location (1.5 *versus* 0.9 μm) in the square channel.

The values of PDI can be compared to the bubbling frequency. We measured values of 0.18 (case a), 6.9 (case b) and 10.7 kHz (case c). As expected, these frequencies are lower than the inverse time of the process studied in Fig. 2.3, because the gas tip retracts to the upstream direction after breakup (Fig. 2.1c), and the channel has to be refilled by the gas before the next collapse starts again.[8] This is the bubbling regime, in contrast to the jetting regime where the gas jet would not retract; such a regime has been predicted to happen only for liquid velocities higher than approximately $\gamma/\eta = 30$ m/s,[19,23] much higher than ours (3 m/s or lower). In the bubbling regime, the durations of the 2D and 3D collapses define the upper bound for the bubbling frequency, and at a given channel height, the stable 2D collapse is shortened and eventually suppressed when the aspect ratio W/H decreases to 1 (square channel).

2.3 Conclusion

In conclusion, the resolved study of the bubble detachment revealed that the ultimate stage of the pinch-off is only controlled by liquid and gas inertia, whose fluctuations cause the jitter in the 3D collapse time. On the other hand, in the 2D collapse, fluctuations are smoothened out by viscosity. Therefore the user has a choice between high monodispersity by using elongated rectangular channels, and high bubbling frequency by using square channels. This study therefore brings new insight in the design of microsystems dedicated to the production of microbubbles of very precise properties, including more complex channel geometries.[24,25]

References

[1] T. M. Squires and S. R. Quake, "Microfluidics: Fluid physics at the nanoliter scale," *Rev. Mod. Phys.* **77**, 977–1026 (2005).

[2] P. Tabeling, *Introduction to Microfluidics* (Oxford University Press, New York, 2006).

[3] J. R. Lindner, "Microbubbles in medical imaging: current applications and future directions," *Nat. Rev. Drug Discovery* **3**, 527–532 (2004).

[4] C. S. Smith, "On blowing bubbles for bragg's dynamic crystal model," *J. Appl. Phys.* **20**, 631 (1949).

[5] A. M. Gañán-Calvo and J. M. Gordillo, "Perfectly monodisperse microbubbling by capillary flow focusing," *Phys. Rev. Lett.* **87**, 274501 (2001).

[6] P. Garstecki, I. Gitlin, W. DiLuzio, G. M. Whitesides, E. Kumacheva, and H. A. Stone, "Formation of monodisperse bubbles in a microfluidic flow-focusing device," *Appl. Phys. Lett.* **85**, 2649–2651 (2004).

[7] P. Garstecki, H. A. Stone, and G. M. Whitesides, "Mechanism for flow-rate controlled breakup in confined geometries: A route to monodisperse emulsions," *Phys. Rev. Lett.* **94**, 164501 (2005).

[8] J.-P. Raven, P. Marmottant, and F. Graner, "Dry microfoams: formation and flow in a confined channel," *Eur. Phys. J. B* **51**, 137–143 (2006).

[9] E. Lorenceau, Y. Y. C. Sang, R. Höhler, and S. Cohen-Addad, "A high rate flow-focusing foam generator," *Phys. Fluids* **18**, 097103 (2006).

[10] Y. Xia and G. M. Whitesides, "Soft lithography," *Annu. Rev. Mat. Sci.* **28**, 153–184 (1998).

[11] D. C. Duffy, J. C. McDonald, O. J. A. Schueller, and G. M. Whitesides, "Rapid prototyping of microfluidic systems in poly(dimethylsiloxane)," *Anal. Chem.* **70**, 4974–4984 (1998).

[12] F. P. Bretherton, "The motion of long bubbles in tubes," *J. Fluid Mech.* **10**, 166–188 (1961).

[13] P. Gondret and M. Rabaud, "Shear instability of two-fluid parallel flow in a hele-shaw cell," *Phys. Fluids* **9**, 3267–3274 (1997).

[14] C. E. Hickox, "Instability due to viscosity and density stratification in axisymmetric pipe flow," *Phys. Fluids* **14**, 251–262 (1971).

[15] L. Preziosi, K. Chen, and D. D. Joseph, "Lubricated pipelining: stability of core-annular flow," *J. Fluid Mech.* **201**, 323–356 (1989).

[16] P. Guillot, A. Colin, A. S. Utada, and A. Ajdari, "Stability of a jet in confined pressure-driven biphasic flows at low reynolds numbers," *Phys. Rev. Lett.* **99**, 104502 (2007).

[17] J. Eggers, "Nonlinear dynamics and breakup of free-surface flows," *Rev. Mod. Phys.* **69**, 865–930 (1997).

[18] J. M. Gordillo, "Axisymmetric bubble pinch-off at high reynolds numbers," *Phys. Rev. Lett.* **95**, 194501 (2005).

[19] A. Sevilla, J. M. Gordillo, and C. Martínez-Bazán, "Transition from bubbling to jetting in a coaxial air-water jet," *Phys. Fluids* **17**, 018105 (2005).

[20] M. S. Longuet-Higgins, B. R. Kerman, and K. Lunde, "The release of air bubbles from an underwater nozzle," *J. Fluid Mech.* **230**, 365–390 (1991).

[21] H. N. Oğuz and A. Prosperetti, "Dynamics of bubble growth and detachment from a needle," *J. Fluid Mech.* **257**, 111–145 (1993).

[22] J. C. Burton, R. Waldrep, and P. Taborek, "Scaling and instabilities in bubble pinch-off," *Phys. Rev. Lett.* **94**, 184502 (2005).

[23] A. M. Gañán-Calvo, M. A. Herrada, and P. Garstecki, "Bubbling in unbounded coflowing liquids," *Phys. Rev. Lett.* **96**, 124504 (2006).

[24] K. Hettiarachchi, E. Talu, M. L. Longo, P. A. Dayton, and A. P. Lee, "On-chip generation of microbubbles as a practical technology for manufacturing contrast agents for ultrasonic imaging," *Lab Chip* **7**, 463–468 (2007).

[25] O. Amyot and F. Plouraboué, "Capillary pinching in a pinched microchannel," *Phys. Fluids* **19**, 033101 (2007).

Chapter 3 Microbubble formation and pinch-off scaling exponent in flow-focusing devices[§]

Abstract

We investigate the gas jet breakup and the resulting microbubble formation in a microfluidic flow-focusing device using ultra high-speed imaging at 1 million frames/s. In recent experiments [Dollet *et al.*, *Phys. Rev. Lett.* **100**, 034504 (2008)] it was found that in the final stage of the collapse the radius of the neck scales with time with a 1/3 power-law exponent, which suggested that gas inertia and the Bernoulli suction effect become important. Here, ultra high-speed imaging was used to capture the complete bubble contour and quantify the gas flow through the neck. It revealed that the resulting decrease in pressure, due to Bernoulli suction, is too low to account for an accelerated pinch-off. The high temporal resolution images enable us to approach the final moment of pinch-off to within 1 μs. We observe that the final moment of bubble pinch-off is characterized by a scaling exponent of 0.41 $\pm$ 0.01. This exponent is approximately 2/5, which can be derived, based on the observation that during the collapse the neck becomes *less slender*, due to the exclusive driving through liquid inertia.

3.1 Introduction

Liquid droplet pinch-off in ambient air or gas bubble pinch-off in ambient liquid can mathematically be seen as a singularity, both in space and time.[1,2] The process that leads to such a singularity has been widely studied in recent years[3–15] and is of major importance in an increasing number

[§]Submitted to *Physics of Fluids* as: W. van Hoeve, B. Dollet, M. Versluis, and D. Lohse, "Microbubble formation and pinch-off scaling exponent in flow-focusing devices."

of medical and industrial applications. Examples of this are the precise formation and deposition of droplets on a substrate using inkjet technology,[16] or for the production of medical microbubbles used in targeted drug delivery.[17,18]

For the pinch-off of liquid in gas, the dynamics close to pinch-off exhibit self-similar behavior, which implies that the local shape of the neck is not influenced by its initial conditions. The radius of the neck goes to zero following a universal scaling behavior with $r_0 \propto \tau^\alpha$, where τ represents the time remaining until pinch-off and α the power law scaling exponent.[1] The scaling exponent α is a signature of the physical mechanisms that drive the pinch-off. The formation and pinch-off of a low-viscosity liquid droplet in air is described by a balance between surface tension and inertia, resulting in a 2/3 scaling exponent.[2–4,6,19,20]

The inverted problem of the collapse of a gaseous thread in a liquid is, however, completely different. Initially, a simple power law was predicted based on a purely liquid inertia driven collapse giving rise to a 1/2 scaling exponent.[7,21,22] However, many groups report power law scaling exponents that are slightly larger than 1/2.[8,11–14,23,24] In recent work of Eggers *et al.*[25] and Gekle *et al.*[15] it was demonstrated that a coupling between the radial and axial length scale of the neck[10] can explain these small variations in the scaling exponent. Based on a slender-body calculation it is found that $\alpha(\tau) = 1/2 + (-16 \ln \tau)^{-1/2}$, where α slowly asymptotes to 1/2 when approaching pinch-off.

In the work of Gordillo *et al.*[8,14] it has been shown that gas inertia, *i.e.* Bernoulli suction, plays an important role in the bubble pinch-off. The increasing gas flow through the neck results in an accelerated collapse with $\alpha = 1/3$.[14,26] It should be noted that the smaller the scaling exponent α the more rapidly the radius of the neck diminishes at the instant of pinch-off, since the speed of collapse $\dot{r}_0 \propto \alpha\tau^{\alpha-1}$, where the overdot denotes the time derivative.

In the work of Dollet *et al.*[27] microbubble formation in a microfluidic flow-focusing device was investigated. A flow-focusing device comprises two co-flowing fluids, an inner gas and an outer liquid phase, that are focused into a narrow channel where bubble pinch-off occurs. It was found that bubble formation in a square cross-sectional channel ($W \times H = 20\,\mu\text{m} \times 20\,\mu\text{m}$) showed a similar collapse behavior giving a 1/3 scaling exponent. In that paper it was suggested that this exponent reflects the influence of gas inertia. However, this scaling exponent could not be conclusively ascribed

to Bernoulli suction, due to a lack of spatial and temporal resolution at the neck in the final stages of pinch-off.

In this work we study the bubble formation for extremely fast bubble pinch-off in a microfluidic flow-focusing channel of square cross-section, using ultra high-speed imaging at 1 Mfps. The complete spatial structure of the bubble, including its neck, was captured. This allowed us to not only investigate the effect of Bernoulli suction, but also the influence of the constituent radial and axial length scale length scales of the neck.

Here we find that the ultimate stage of microbubble pinch-off is purely *liquid* inertia driven. In our system, the neck becomes *less slender* when approaching the pinch-off, giving rise to an exponent $\alpha = 2/5$ over almost 2 decades, which is different as compared to the case of bubble pinch-off in the bulk as reported by Bergmann *et al.*,[11] Thoroddsen *et al.*,[13] and Gekle *et al.*,[26] among others.

3.2 Experimental setup

The experimental setup is shown in Fig. 3.1a. The flow-focusing device is fabricated with a square cross-section channel geometry, with channel width $W = 60\,\mu$m and height $H = 59\,\mu$m, as depicted schematically in Fig. 3.1, to ensure that the collapse occurs in the radial 3D collapse regime only.[27] The device was produced using rapid prototyping techniques.[28] A homogeneous layer of negative photoresist (SU-8) is spin-coated on a silicon wafer. The thickness of the layer defines the channel height. A chrome mask (MESA$^+$ Institute for Nanotechnology, University of Twente, The Netherlands) is used in contact photolithography to imprint features with sizes down to 2 μm. After ultraviolet exposure a cross-linking reaction starts which rigidifies the photoresist that is exposed to the light. The photoresist that is not exposed is removed during development with isopropanol. What is left is a positive relief structure which can be used as a mold to imprint micron-sized channels in polydimethylsiloxane (PDMS) (Sylgard 184, Dow Corning). PDMS is a transparent polymer which is obtained by mixing two components, base and curing agent, in a 10:1 ratio in weight. The mixture is poured on the mold and cured in a 65°C oven for 1 hour. The PDMS slab with imprinted microchannels is removed from the mold and then holes are punched in the PDMS. The PDMS slab is oxygen plasma-bonded (Harrick Plasma, Model PDC-002, Ithaca, NY, USA) to a glass cover plate of 1 mm thickness to close the channels. Plasma bonding creates

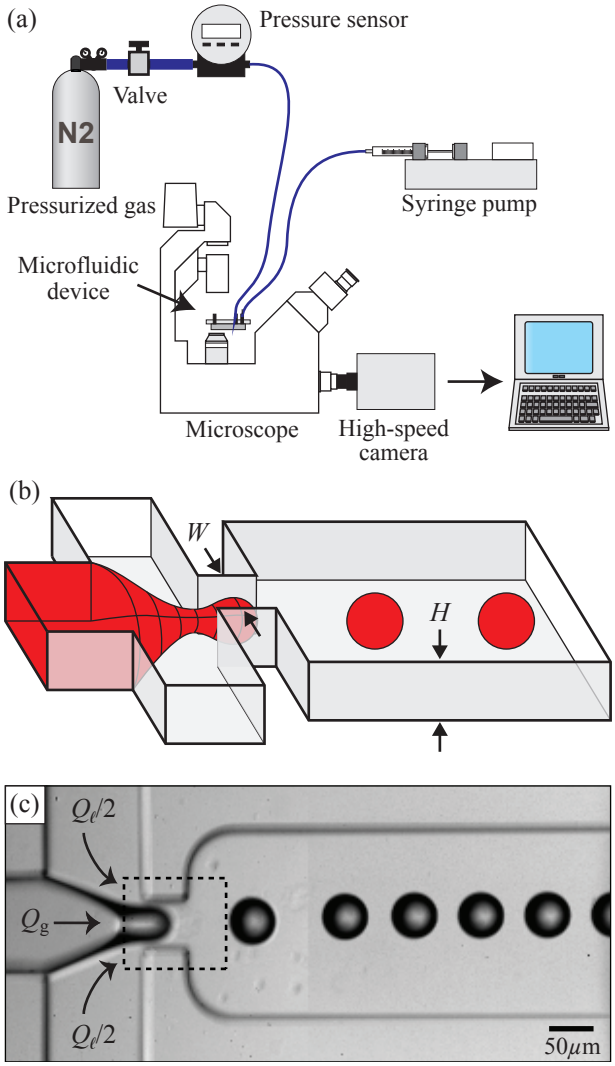

Figure 3.1: (a) Schematic overview of the setup for the study of microbubble formation in microfluidic flow-focusing devices. A high-speed camera mounted to an inverted microscope is used to capture the final moment of microbubble pinch-off. Gas pressure was controlled by a pressure regulator connected to a sensor. The liquid flow rate was controlled by a high-precision syringe pump. (b) Schematic representation of a planar flow-focusing device with uniform channel height $H = 59\,\mu$m and channel width $W = 60\,\mu$m. (c) Snapshot of a high-speed recording. The outer liquid flow Q_ℓ forces the inner gas flow Q_g to enter a narrow channel (encircled by the dashed line) in which a microbubble is formed.

a non-reversible bond which can withstand pressures up to a few bars.[29,30] The oxygen plasma turns the PDMS channel walls temporarily hydrophilic which enhances fluid flow and wetting of the channel walls. After closing the device, 1/16 inch outer diameter Telfon tubing is connected to the inlet channels, through which gas and liquid is supplied.

Nitrogen gas is controlled by a regulator (Omega, PRG101-25) connected to a pressure sensor (Omega, DPG1000B-30G). The gas supply pressure was 12 kPa. A 10% (w/w) solution of dishwashing liquid (Dreft, Procter & Gamble) in deionized water is flow-rate-controlled using a high precision syringe pump (Harvard Apparatus, PHD 2000, Holliston, MA, USA). The liquid, with density $\rho = 1000\,\mathrm{kg/m^3}$, surface tension $\gamma = 35\,\mathrm{mN/m}$, and viscosity $\eta = 1\,\mathrm{mPa{\cdot}s}$, wets the channel walls. The liquid surfactant solution was supplied at a flow rate $Q_\ell = 185\,\mu\mathrm{l/min}$. The Reynolds number $\mathrm{Re} = \rho Q_\ell R/\eta WH \approx 26$, with nozzle radius $R = WH/\left(W + H\right) \approx 30\,\mu\mathrm{m}$, is low enough to guarantee that the flow is laminar.

The bubble formation process is imaged using an inverted microscope (Nikon Instruments, Eclipse TE2000-U, Melville, NY, USA) equipped with an extra long working distance objective with a cover glass correction collar (Nikon Instruments, 60× Plan Fluor ELWD N.A. 0.70 W.D. 2.1–1.5 mm, Melville, NY, USA) and an additional 1.5× magnification lens. The system is operated in bright-field mode using high-intensity fiber illumination (Olympus, ILP-1, Zoeterwoude, The Netherlands).

To resolve the growth of the bubble and the extremely fast bubble pinch-off at the same time requires a high-speed camera that is capable of recording images at a high frame rate and at full resolution so that the field of view is sufficient to capture the entire bubble profile at sufficiently high spatial resolution. These two criteria, *i.e.* a short interframe time (of the order of $1\,\mu\mathrm{s}$) and a sufficiently large field of view means a specialized ultra high-speed camera is required for this task. Hence, we use the Shimadzu ultra high-speed camera (Shimadzu Corp., Hypervision HPV-1, Kyoto, Japan) to capture 100 consecutive images at a high temporal resolution of 1 Mfps (equivalent to an interframe time of $1\,\mu\mathrm{s}$), exposure time of $0.5\,\mu\mathrm{s}$, field of view of $200\,\mu\mathrm{m} \times 175\,\mu\mathrm{m}$, and with a spatial resolution of $0.68\,\mu\mathrm{m/pixel}$.

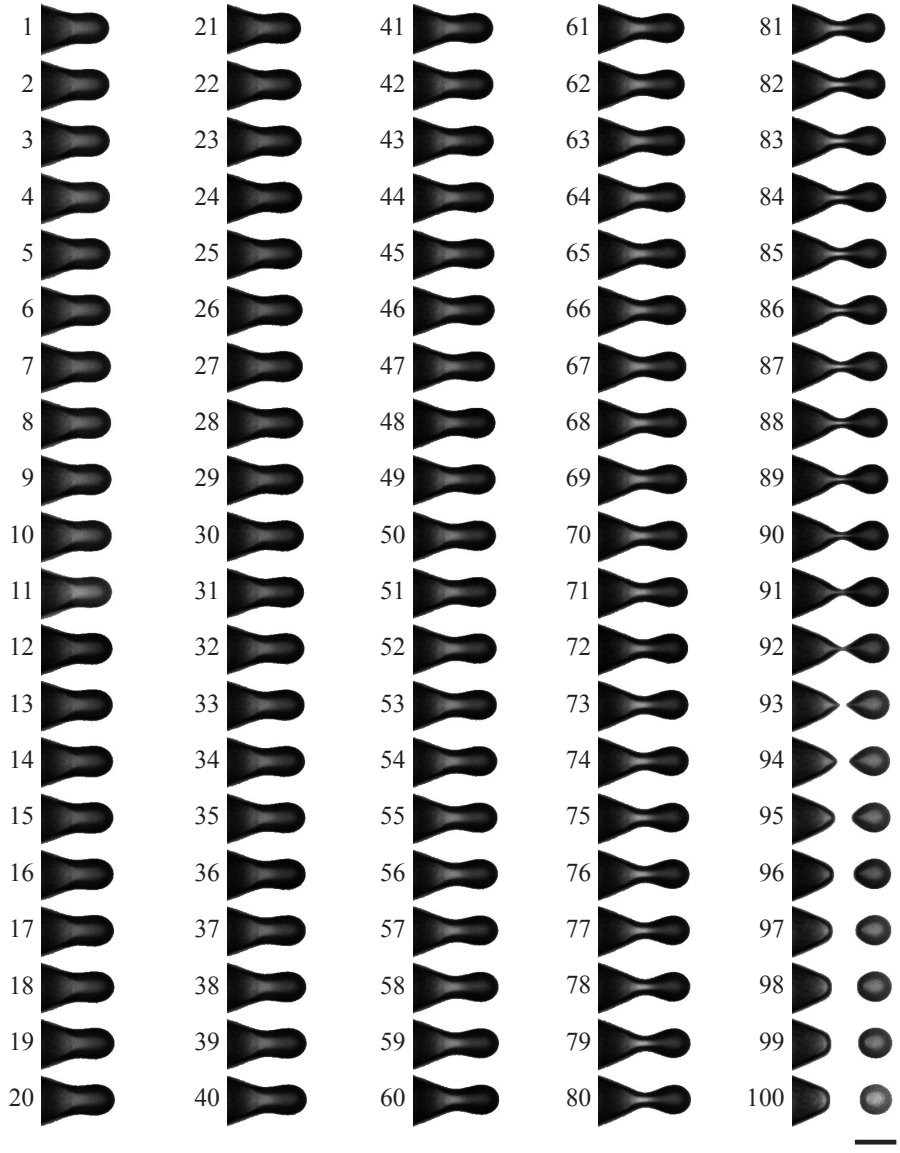

Figure 3.2: Time series showing the formation of a microbubble in a microfluidic flow-focusing device recorded at 1 Mfps. The frame number is indicated at the left of each frame. For reasons of clarity, the background, including the channel structure, is subtracted. A detailed image that corresponds to frame 86 is represented in Fig. 3.3a. The camera's field of view is indicated by the dashed line in Fig. 3.1c. The exposure time is 0.5 μs. The scale bar in the lower right corner denotes 50 μm.

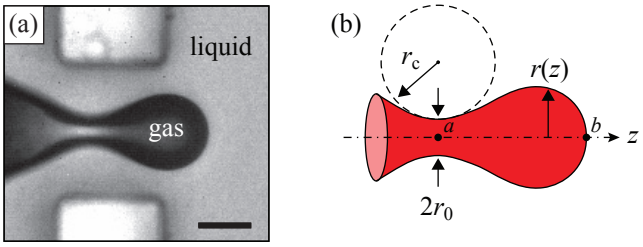

Figure 3.3: (a) Snapshot of the high-speed recording showing the formation of a microbubble corresponding to frame 86 in Fig. 3.2. The scale bar denotes 25 μm. (b) System of coordinates for an axisymmetric bubble. The shape of the gas-liquid interface $r(z)$ is described as a function of the axial-coordinate z. The bubble's volume is the volume enclosed between a and b indicated on the z-axis. The gaseous thread forms a neck that is concave in shape with r_0 and r_c the circumferential and axial radius of curvature respectively.

3.3 Results

3.3.1 Extracting the collapse curves

In Fig. 3.2 a time series of the formation of a microbubble is shown, where all images are background subtracted to improve the contrast. The first image (frame 1) shows the bubble almost completely blocking the narrow channel (*cf.* Fig. 3.1c). This restricts the outer liquid flow and the liquid starts to squeeze the gas in the radial direction forming a neck. The neck becomes smaller and smaller until final pinch-off, resulting in bubble detachment (frame 93). The complete contour of the bubble is extracted from the recordings using image analysis algorithms in MATLAB (Mathworks Inc., Natick, MA, USA). In order for precise detection of the contour the images were resampled and bandpass filtered in the Fourier domain to achieve sub-pixel accuracy. The schematic of the axisymmetric shape of the bubble with the axis of symmetry along the z-axis is given in Fig. 3.3.

In Fig. 3.4a a surface contour plot of the radius of the bubble r as a function of the axial coordinate z and the time remaining until pinch-off τ is shown. The minimum radius of the neck r_0 is indicated by the dashed line. In Fig. 3.4b we plot r_0 as a function of the time remaining until pinch-off $\tau = t_c - t$, with t the time and t_c the collapse time, on a linear scale, whereas the collapse curve is represented on a logarithmic scale in Fig. 3.4c. The collapse time is defined as the moment when the neck reaches its critical radius $r_0 = 0$ and breaks. From the ultra high-speed

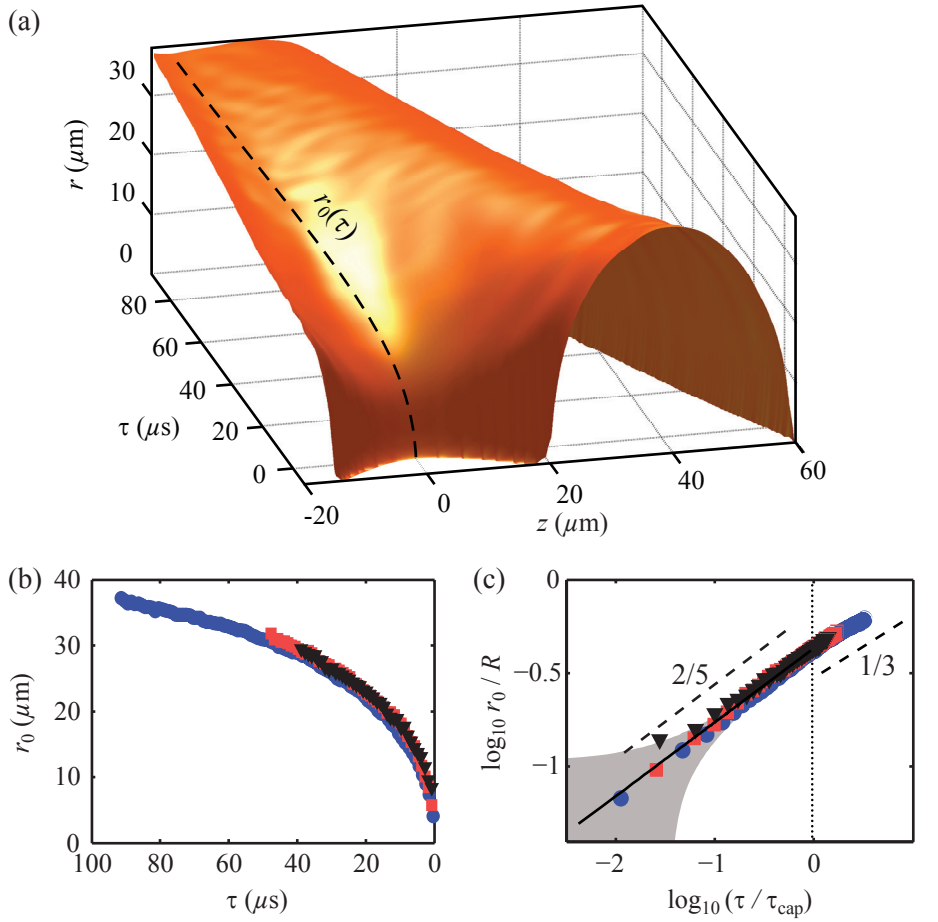

Figure 3.4: (a) Surface contour plot (false color) of the formation of a microbubble. The axisymmetric radius of the bubble is plotted as a function of the axial coordinate z and the time until pinch-off $\tau = t_c - t$. The dashed line indicates the minimum radius of the neck r_0 until final collapse and pinch-off at the origin. (b) The time evolution of the minimum radius of the neck for three different experiments under the same initial conditions. (c) The logarithm of the minimum radius of the neck r_0 normalized by the nozzle radius $R = 30\,\mu$m as a function of the logarithm of the time until final pinch-off τ, normalized by the capillary time $\tau_{cap} = 28\,\mu$s. The solid line represents the best fit to the data showing a 0.41 ± 0.01 slope. The dashed lines with slope 2/5 and slope 1/3 serve as a guide to the eye. The vertical dotted line marks the time closest to pinch-off measured in the work of Dollet *et al.*[27] The error in determining the collapse time t_c is visualized as the gray area.

imaging results it can be found that this moment occurs between the last frame before actual pinch-off (frame 93 in Fig. 3.2) and the first frame after pinch-off (frame 94). We estimate the time of collapse with sub-interframe time accuracy by assuming that the collapse exhibits a power law behavior with $r_0 \propto (t_c - t)^\alpha$, where the exponent α and the collapse time t_c are *a priori* unknown, similarly as was done in Bergmann *et al.*[31] From a best fit to the data we obtain $t_c = 93.3 \pm 1\,\mu$s, where the maximum systematic error is equal to the time between two frames. Note that the error in estimating t_c results in a deflection of the datapoints away from a straight line bounded between the curves $\log r_0(\tau \pm 1 \times 10^{-6}\,\mathrm{s})/R$ indicated by the gray area in Fig. 3.4c. This figure also suggests that two different stages during bubble formation exist: in the first stage of the collapse, all data was found to be well approximated by a power law $r_0/R \propto (\tau/\tau_{\mathrm{cap}})^\alpha$, with $\alpha = 0.29 \pm 0.02$. In the final stage, when $\tau \leq \tau_{\mathrm{cap}}$, a scaling with exponent $\alpha = 0.41 \pm 0.01$ is observed, spanning almost two decades.

3.3.2 Liquid inertia driven pinch-off

Approaching the singularity at pinch-off ($\tau \to 0$), the relative importance between viscous forces, surface tension forces, and inertial forces are given by the Reynolds number, Weber number, and the capillary number. The Reynolds number, as a measure of the ratio between inertial forces to viscous forces, is expressed as

$$\mathrm{Re} = \frac{\rho r_0 \dot{r}_0}{\eta}, \tag{3.1}$$

with characteristic length scale r_0, and characteristic velocity equivalent to the radial velocity of the interface $\dot{r}_0$. The relative importance of inertial forces with respect to surface tension forces is given by the Weber number

$$\mathrm{We} = \frac{\rho r_0 \dot{r}_0^2}{\gamma}. \tag{3.2}$$

The capillary number represents the relative importance of viscous forces to surface tension forces as

$$\mathrm{Ca} = \frac{\eta \dot{r}_0}{\gamma}. \tag{3.3}$$

If we now assume that $r_0 \propto \tau^\alpha$, where the experimentally determined scaling exponent is close to $\alpha = 2/5$, it follows that $\mathrm{Re} \propto \tau^{-1/5}$, $\mathrm{We} \propto$

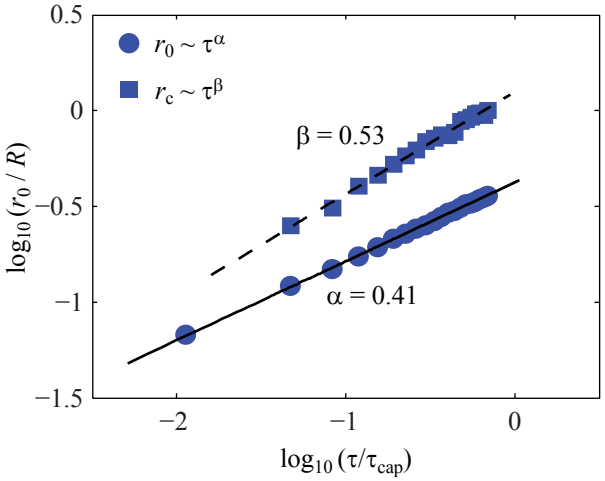

Figure 3.5: The axial radius of curvature r_c (squares) decreases faster compared to the circumferential radius of curvature r_0 (bullets). Hence the neck becomes less slender approaching pinch-off. Thus the slenderness ratio $\lambda = r_c/r_0$, becomes smaller when approaching the pinch-off. The radii of curvature are normalized by the nozzle radius $R = 30\,\mu$m. The time until pinch-off is normalized by the capillary time $\tau_{cap} \approx 28\,\mu$s.

$\tau^{-4/5}$, and Ca $\propto \tau^{-3/5}$. This implies that Re, We, and Ca all diverge approaching the singularity. Accordingly, inertial forces must dominate both surface tension and viscous forces, hence the final stage of the collapse is purely liquid inertia dominated.

In Eggers *et al.*[25] it was shown that for a liquid inertia driven collapse both the radial and axial length scale of the neck are important. Hence, the time evolution of the shape of the neck is investigated by measuring its slenderness. The slenderness ratio λ is defined as the ratio of the axial radius of curvature to the circumferential radius of curvature of the neck. The larger the slenderness ratio is, the more slender the neck is. The axial radius of curvature is measured by locally fitting a circle with radius r_c to the contour of the neck, whereas the circumferential radius of curvature r_0 is equivalent to the minimum radius of the neck, see Fig. 3.3. In Fig. 3.5 the time evolution of the principal radii of curvature are plotted on a logarithmic scale for the final stage of the collapse. It is found that the axial radius of curvature exhibits a power law behavior $r_c \propto \tau^{\beta}$, with $\beta = 0.53$. The circumferential radius of curvature scales as $r_0 \propto \tau^{\alpha}$, with $\alpha = 0.41$, as was shown before (*cf.* Fig. 3.4c).

The axial radius of curvature is found to have the more rapidly dimin-

ishing exponent ($\beta > \alpha$), which implies that the slenderness $\lambda = r_c/r_0 \propto \tau^\beta/\tau^\alpha \to 0$ for $\tau \to 0$. In other words, the neck profile becomes *less slender* approaching pinch-off, thus, both the radial and the axial length scales are still important. This 3D character implies that the liquid flows spherically inward towards the collapsing neck. Thus, it might be anticipated that, this 3D collapse can be approximately described using the Rayleigh-Plesset equation for spherical bubble collapse[22]

$$r_0\ddot{r}_0 + \frac{3}{2}\dot{r}_0^2 = \frac{1}{\rho}\left(p - \frac{2\gamma}{r_0}\right), \tag{3.4}$$

with capillary pressure p. It should be noted that a necessary condition for this is that the neck should be much smaller than the channel dimensions ($r_0 \ll W$, H). By substituting $r_0 \propto \tau^\alpha$ in above equation and keeping the right-hand side constant, which assumes an inertia-dominated flow, it is found that it is necessary that $\alpha = 2/5$, which agrees surprisingly well with our experimental findings of 0.41 ± 0.01.

3.3.3 "Filling effect"

How to account for the scaling $r_0 \propto \tau^{0.29\pm0.02}$ for $\tau > \tau_{cap}$, *i.e.* at early times? At this initial stage of the collapse a thin layer of liquid with a thickness of several micrometers separates the bubble from the hydrophilic channel wall.[32] The liquid flow in such a confined channel can be described using Darcy's law for pressure driven flow through porous media. The volumetric flow rate of liquid that permeates into the neck region is

$$Q_{in} = -\frac{kA}{\eta}\frac{\partial p}{\partial z}, \tag{3.5}$$

with k the permeability, $A = WH - \pi r_0^2$ the cross-sectional area of the thin liquid layer surrounding the bubble, and $\partial p/\partial z$ the pressure gradient.

The pressure distribution in the liquid is inhomogeneous, thus the bubble's surface does not have a constant curvature even though the gas pressure is practically uniform. The pressure gradient that drives the liquid flow can be derived from the capillary pressure

$$p = \gamma\left(\frac{1}{r_0} - \frac{1}{r_c}\right). \tag{3.6}$$

In the initial stage of the collapse, *i.e.* at the onset of neck formation, $r_c > r_0$. As a gross simplification, we approximate the neck as a radi-

ally collapsing cylinder, of length r_c much larger than its radius r_0. The capillary pressure is then $p \approx \gamma/r_0$, therefore $\partial p/\partial z \approx -r_0^{-2}\partial r_0/\partial z$.

The volumetric gas flow rate that is pushed out of the neck region is

$$Q_{out} = \dot{V}_g \approx r_0 r_c \dot{r}_0, \tag{3.7}$$

with $V_g \approx r_c r_0^2$ the volume occupied by the gas.

The gas in the neck is replaced by the liquid. This is referred to as the "filling effect", thus, from a balance between Eq. (3.5) and Eq. (3.7), we now get

$$r_0 r_c \dot{r}_0 \approx \frac{1}{r_0^2}\frac{\partial r_0}{\partial z} \approx \frac{1}{r_0 r_c}, \tag{3.8}$$

hence, assuming that r_c varies little in this initial stage of the collapse, $r_0^2\dot{r}_0$ is roughly constant. It follows that the radius of the neck must scale as $r_0 \propto \tau^\alpha$, with $\alpha = 1/3$. This is in good agreement with the experimentally measured scaling exponent $\alpha \approx 0.29 \pm 0.02$ for $\tau > \tau_{cap}$.

3.4 Discussion

In Gekle *et al.*[26] a supersonic air flow through the neck is visualized using smoke particles and it is reported that Bernoulli suction accelerates the collapse. An accelerated collapse due to Bernoulli suction is also reported by Gordillo *et al.*,[8] giving rise to a 1/3 scaling exponent. It is extremely difficult to measure the gas velocity in a microfluidic flow-focusing device in a direct way. However, the camera's wide field of view ($200\,\mu m \times 175\,\mu m$) enabled us to capture the contour of the expanding bubble in great detail and allows for an estimate of the gas velocity.

The volume of the bubble V_b, as the gas volume downstream of the neck that is enclosed by the bubble contours, is calculated as follows:

$$V_b = \int_a^b \mathrm{d}z \pi r^2(z), \tag{3.9}$$

with the profile of the bubble $r(z)$, with a the axial coordinate of the location of the neck and b the tip of the bubble (*cf.* Fig. 3.3). We plot the bubble volume V_b as a function of time until pinch-off in Fig. 3.6. The bubble's contour is indicated for four characteristic moments during the bubble formation process in the panels (i–iv) of Fig. 3.6. In the initial stage the gaseous thread in front of the flow-focusing channel is forced to

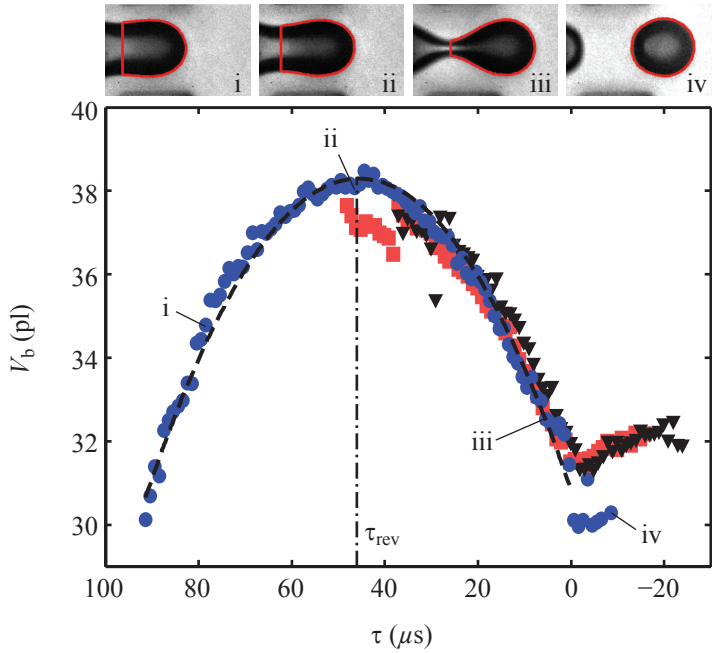

Figure 3.6: Volume of the bubble V_b as a function of the time until pinch-off τ. The volume of the bubble was calculated by integration over its contour along the z-axis between the neck and the tip of the bubble (indicated a and b in Fig. 3.3). The insets (i–iv) depict the contours that enclose the bubble's volume corresponding to the marked data points in the graph. A second order polynomial fit is used to calculate $\partial V_b/\partial\tau$ (dashed line). The bubble reaches its maximum volume at τ_{rev} (dashed-dotted line) and the gas flow direction reverses, consequently, the bubble shrinks during the final moments before pinch-off. Different symbols represent different experiments, giving an indication of the reproducibility.

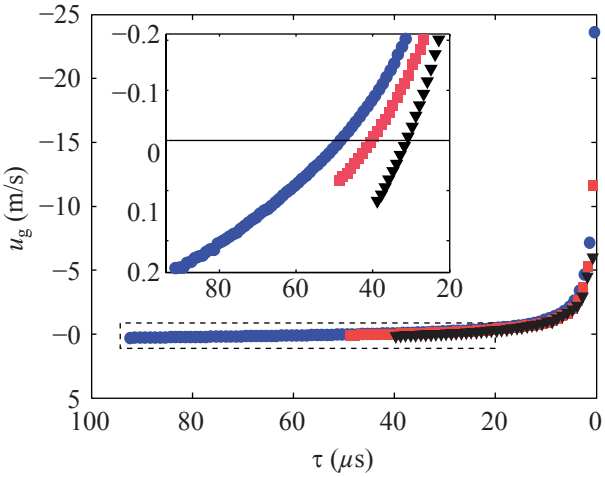

Figure 3.7: Gas velocity u_g in the neck as a function of the time until collapse τ. The initial positive gas velocity reverses its flow direction and accelerates when approaching the pinch-off. At the moment of pinch-off maximum velocity of -23 m/s is reached. In the inset an enlarged section of the graph for the data points encircled by the dashed line is represented demonstrating the gas flow reversal. Again, different symbols/colors represent different individual experiments.

enter the channel and completely fills it (i–ii). The volume of the bubble increases until it reaches a maximum volume of 38 pl at $\tau = 46\,\mu$s (ii). The restricted liquid flow starts to "squeeze" the gaseous thread and a clearly visible neck begins to develop. Then a remarkable event takes place—the gas flow reverses and the neck starts to collapse (ii-iii) until bubble pinch-off occurs. The volume of the bubble beyond pinch-off ($\tau < 0$) is 31 pl, which is equivalent to a bubble radius of 19 μm.

We estimate the volumetric gas flow rate Q_g through the neck as the time derivative of the volume of the bubble, $Q_g = \dot{V}_b$, where it is assumed that no gas diffusion into the surrounding liquid take place. The bubble volume is approximated by a second order polynomial function, as indicated by the dashed line in Fig. 3.6, which is used to obtain the time derivative of the volume.

The gas velocity through the neck u_g is calculated as the volume flow rate Q_g divided by the cross-sectional area of the neck (πr_0^2). In Fig. 3.7 we plot the gas velocity as a function of the time until pinch-off. Note that the gas velocity is low during almost the entire collapse process, *i.e.* $|u_g| < 0.5$ m/s (see the inset in Fig. 3.7), however, in the final stage of the collapse,

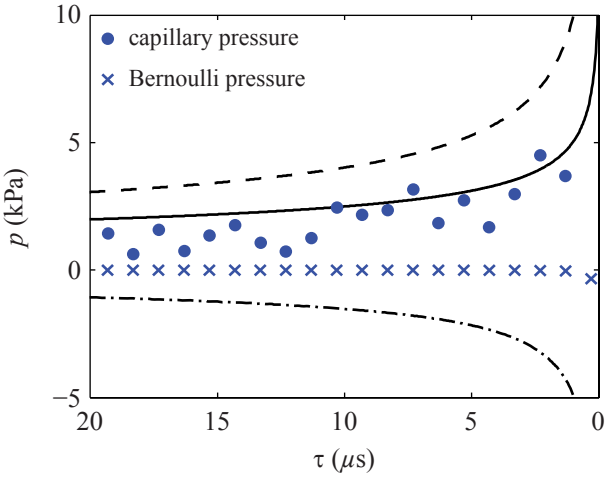

Figure 3.8: Evolution of the capillary pressure and the Bernoulli pressure drop during the final moments of bubble pinch-off. The dashed line indicates the capillary pressure contribution due to the circumferential curvature ($p = \gamma/r_0$, with $r_0 \propto \tau^{0.41}$); the dashed-dotted line shows the pressure contribution from the axial curvature ($p = -\gamma/r_c$, with $r_c \propto \tau^{0.53}$); the solid line represents the sum of both contributions. The bullets represents the capillary pressure obtained from the local shape of the neck ($r(z)$) extracted from the wide-field-of-view images and using Eq. (3.10). The increasing gas velocity through the neck causes a local pressure reduction in the neck, referred to as Bernoulli suction ($p = -\rho u_g^2/2$), as indicated by the crosses. It can be seen that the capillary pressure clearly dominates during the entire bubble formation process.

a strong acceleration of the gas flow is observed, reaching a velocity up to $u_{max} = -23\,\mathrm{m/s}$. The pressure drop due to the fast gas flow through the neck is given by Bernoulli's equation as $\Delta p = -\rho_g \left(u_{rev}^2 - u_{max}^2\right)/2 \approx 0.3\,\mathrm{kPa}$, with $u_{rev} = 0\,\mathrm{m/s}$ the gas velocity at the moment of flow reversal and $\rho_g = 1.2\,\mathrm{kg/m^3}$ the gas density.

We now compare this pressure drop with the capillary pressure in the neck. Just before pinch-off, the capillary pressure, as a consequence of surface tension forces acting on the curved interface, should be at a much higher pressure than the surrounding liquid. For an axisymmetric surface profile, with $r = r(z)$, the capillary pressure, as a function of the axial coordinate z, is given by the Laplace equation

$$p(z) = \gamma \left[\frac{1}{r\sqrt{1+r'^2}} - \frac{r''}{\left(1+r'^2\right)^{3/2}} \right], \tag{3.10}$$

where prime denotes the derivative with respect to z.[33] Note that, at the

location where the neck is thinnest, the first term equals the circumferential curvature (r_0^{-1}), whereas the second term represents the axial curvature (r_c^{-1}). In Fig. 3.8, both the Bernoulli pressure drop and the capillary pressure in the neck are plotted as a function of the time remaining until pinch-off. The capillary pressure (represented by the bullets) is obtained by inserting the complex shape of the neck into Eq. (3.10). The dashed line and the dashed-dotted line indicate the pressure contribution from the circumferential curvature ($p \propto \gamma\tau^{-\alpha}$) and the axial curvature ($p \propto -\gamma\tau^{-\beta}$) respectively, while the solid line represents the sum of both contributions of the capillary pressure. In the figure it is demonstrated that the pressure drop due to Bernoulli suction is marginal in comparison to the increasing capillary pressure approaching pinch-off. Hence, it can be concluded that Bernoulli suction, *i.e.* gas inertia, is irrelevant during the entire bubble formation process. It is also shown that the concave axial curvature counteracts the circumferential curvature leading to a significant decrease in capillary pressure. This confirms that the axial length scale of the neck is important and gives the collapse a three-dimensional character.

3.5 Conclusion

In conclusion, we visualized the complete microbubble formation and extremely fast bubble pinch-off in a microscopically narrow flow-focusing channel of square cross-section ($W \times H = 60\,\mu\text{m} \times 59\,\mu\text{m}$), using ultra high-speed imaging. The camera's wide field of view enabled visualization of all the features of bubble formation, including the two principal radii of curvature of the bubble's neck. Recording was performed at 1 Mfps, thereby, approaching the moment of pinch-off to within $1\,\mu$s. It was found that the neck's axial length scale decreases faster than the radial one, ensuring that the neck becomes less and less slender, collapsing spherically towards a point sink. We describe this collapse using the Rayleigh-Plesset equation for spherical bubble collapse,[22] and recover a 2/5 power law exponent which is consistent with our experimental findings. The gas velocity through the neck is calculated from the growth-rate of the bubble. Just before pinch-off the gas velocity accelerates up to -23 m/s reducing the bubble's volume, however this velocity is too low for Bernoulli suction to be the dominant effect. Thus, the final moment of microbubble pinch-off in a flow-focusing system is purely liquid inertia driven.

References

[1] J. Eggers, "Nonlinear dynamics and breakup of free-surface flows," *Rev. Mod. Phys.* **69**, 865–930 (1997).

[2] J. Eggers and E. Villermaux, "Physics of liquid jets," *Rep. Prog. Phys.* **71**, 036601 (2008).

[3] Y.-J. Chen and P. H. Steen, "Dynamics of inviscid capillary breakup: collapse and pinchoff of a film bridge," *J. Fluid Mech.* **341**, 245–267 (1997).

[4] R. F. Day, E. J. Hinch, and J. R. Lister, "Self-similar capillary pinchoff of an inviscid fluid," *Phys. Rev. Lett.* **80**, 704–707 (1998).

[5] A. M. Gañán-Calvo and J. M. Gordillo, "Perfectly monodisperse microbubbling by capillary flow focusing," *Phys. Rev. Lett.* **87**, 274501 (2001).

[6] D. Leppinen and J. R. Lister, "Capillary pinch-off in inviscid fluids," *Phys. Fluids* **15**, 568–578 (2003).

[7] J. C. Burton, R. Waldrep, and P. Taborek, "Scaling and instabilities in bubble pinch-off," *Phys. Rev. Lett.* **94**, 184502 (2005).

[8] J. M. Gordillo, A. Sevilla, J. Rodríguez-Rodríguez, and C. Martínez-Bazán, "Axisymmetric bubble pinch-off at high reynolds numbers," *Phys. Rev. Lett.* **95**, 194501 (2005).

[9] A. M. Gañán-Calvo, M. A. Herrada, and P. Garstecki, "Bubbling in unbounded coflowing liquids," *Phys. Rev. Lett.* **96**, 124504 (2006).

[10] J. M. Gordillo and M. Pérez-Saborid, "Axisymmetric breakup of bubbles at high Reynolds numbers," *J. Fluid Mech.* **562**, 303–312 (2006).

[11] R. P. H. M. Bergmann, D. van der Meer, M. Stijnman, M. Sandtke, A. Prosperetti, and D. Lohse, "Giant bubble pinch-off," *Phys. Rev. Lett.* **96**, 154505 (2006).

[12] N. C. Keim, P. Møller, W. W. Zhang, and S. R. Nagel, "Breakup of air bubbles in water: Memory and breakdown of cylindrical symmetry," *Phys. Rev. Lett.* **97**, 144503 (2006).

[13] S. T. Thoroddsen, T. G. Etoh, and K. Takehara, "Experiments on bubble pinch-off," *Phys. Fluids* **19**, 042101 (2007).

[14] J. M. Gordillo, "Axisymmetric bubble collapse in a quiescent liquid pool. I. Theory and numerical simulations," *Phys. Fluids* **20**, 112103 (2008).

[15] S. Gekle, J. H. Snoeijer, D. Lohse, and D. van der Meer, "Approach to universality in axisymmetric bubble pinch-off," *Phys. Rev. E* **80**, 036305 (2009).

[16] H. Wijshoff, "The dynamics of the piezo inkjet printhead operation," *Phys. Rep.* **491**, 77–177 (2010).

[17] K. W. Ferrara, R. Pollard, and M. A. Borden, "Ultrasound microbubble contrast agents: Fundamentals and application to gene and drug delivery," *Ann. Rev. Biomed. Eng.* **9**, 415–447 (2007).

[18] K. W. Ferrara, M. A. Borden, and H. Zhang, "Lipid-shelled vehicles: Engineering for ultrasound molecular imaging and drug delivery," *Acc. Chem. Res.* **42**, 881–892 (2009).

[19] J. C. Burton, J. E. Rutledge, and P. Taborek, "Fluid pinch-off dynamics at nanometer length scales," *Phys. Rev. Lett.* **92**, 244505 (2004).

[20] H. González and F. J. García, "The measurement of growth rates in capillary jets," *J. Fluid Mech.* **619**, 179–212 (2009).

[21] M. S. Longuet-Higgins, B. R. Kerman, and K. Lunde, "The release of air bubbles from an underwater nozzle," *J. Fluid Mech.* **230**, 365–390 (1991).

[22] H. N. Oğuz and A. Prosperetti, "Dynamics of bubble-growth and detachment from a needle," *J. Fluid Mech.* **257**, 111–145 (1993).

[23] R. Bolaños-Jiménez, A. Sevilla, C. Martínez-Bazán, and J. M. Gordillo, "Axisymmetric bubble collapse in a quiescent liquid pool. II. Experimental study," *Phys. Fluids* **20**, 112104 (2008).

[24] R. Bolaños-Jiménez, A. Sevilla, C. Martínez-Bazán, D. van der Meer, and J. M. Gordillo, "The effect of liquid viscosity on bubble pinch-off," *Phys. Fluids* **21**, 072103 (2009).

[25] J. Eggers, M. A. Fontelos, D. Leppinen, and J. H. Snoeijer, "Theory of the collapsing axisymmetric cavity," *Phys. Rev. Lett.* **98**, 094502 (2007).

[26] S. Gekle, I. Peters, J. M. Gordillo, D. van der Meer, and D. Lohse, "Supersonic air flow due to solid-liquid impact," *Phys. Rev. Lett.* **104**, 024501 (2010).

[27] B. Dollet, W. van Hoeve, J.-P. Raven, P. Marmottant, and M. Versluis, "Role of the channel geometry on the bubble pinch-off in flow-focusing devices," *Phys. Rev. Lett.* **100**, 034504 (2008).

[28] D. C. Duffy, J. C. McDonald, O. J. A. Schueller, and G. M. Whitesides, "Rapid prototyping of microfluidic systems in Poly(dimethylsiloxane)," *Anal. Chem.* **70**, 4974–4984 (1998).

[29] S. Bhattacharya, A. Datta, J. M. Berg, and S. Gangopadhyay, "Studies on surface wettability of poly(dimethyl) siloxane (PDMS) and glass under oxygen-plasma treatment and correlation with bond strength," *J. Microelectromech. S.* **14**, 590–597 (2005).

[30] M. A. Eddings, M. A. Johnson, and B. K. Gale, "Determining the optimal PDMS-PDMS bonding technique for microfluidic devices," *J. Micromech. Microeng.* **18**, 067001 (2008).

[31] R. P. H. M. Bergmann, D. van der Meer, S. Gekle, J. A. van der Bos, and D. Lohse, "Controlled impact of a disk on a water surface: cavity dynamics," *J. Fluid Mech.* **633**, 381–409 (2009).

[32] P. Garstecki, I. Gitlin, W. DiLuzio, G. M. Whitesides, E. Kumacheva, and H. A. Stone, "Formation of monodisperse bubbles in a microfluidic flow-focusing device," *Appl. Phys. Lett.* **85**, 2649–2651 (2004).

[33] P.-G. de Gennes, F. Brochard-Wyart, and D. Quéré, *Capillarity and Wetting Phenomena: Drops, Bubbles, Pearls, Waves* (Springer, New York, US, 2004).

Chapter 4 Microbubble generation in a co-flow device operated in a new regime[§]

Abstract

A new regime of operation of PDMS-based flow-focusing microfluidic devices is presented. We show that monodisperse microbubbles with diameters below one-tenth of the channel width (here $W = 50\,\mu$m) can be produced in low viscosity liquids thanks to a strong pressure gradient in the entrance region of the channel. In this new regime bubbles are generated at the tip of a long and stable gas ligament whose diameter, which can be varied by tuning appropriately the gas and liquid flow rates, is substantially smaller than the channel width. Through this procedure the volume of the bubbles formed at the tip of the gas ligament can be varied by more than two orders of magnitude. The experimental results for the bubble diameter d_b as function of the control parameters are accounted for by a scaling theory, which predicts $d_\mathrm{b}/W \propto (\mu_\mathrm{g}/\mu_\ell)^{1/12}\,(Q_\mathrm{g}/Q_\ell)^{5/12}$, where μ_g and μ_ℓ indicate, respectively, the gas and liquid viscosities and Q_g and Q_ℓ are the gas and liquid flow rates. As a particularly important application of our results we produce monodisperse bubbles with the appropriate diameter for therapeutical applications ($d_\mathrm{b} \simeq 5\,\mu$m) and a production rate exceeding 10^5 Hz.

4.1 Introduction

Microbubble formation is an area of growing interest due to its countless applications in food processing,[1] material science,[2] pharmacy and medicine.[3] In the last few decades, microbubbles have become the most effective type of contrast agent available for medical ultrasound imaging[4–6] or as carri-

[§]Accepted for publication in *Lab on a Chip* as: E. Castro-Hernández, W. van Hoeve, D. Lohse, and J. M. Gordillo, "Microbubble generation in a co-flow device operated in a new regime."

ers for targeted drug delivery.[7,8] In order to ensure that microbubbles can safely flow through the smallest capillaries, the diameter of the microbubbles injected into the patient's blood stream needs to be between 1 and 10 μm; the preferred diameter is between 2 μm and 5 μm. Larger bubbles may provoke edema and smaller ones possess a poor reflectivity.

Microbubbles with sizes in the correct range for therapeutical purposes can be easily produced by either sonication or by mechanical agitation.[9–12] The generation of bubbles with a size below 1 μm can be achieved through the injection of a gas using porous membranes, which requires an extremely high working pressure typically of the order of 10 MPa.[13] However, all these procedures generate a polydisperse emulsion of bubbles in the liquid, limiting the potential use of microbubbles in medicine. Indeed, it is of current interest for therapeutical applications to design a simple procedure for the mass production of microbubbles with controllable diameters ranging from 2 to 5 μm and *with a low polydispersity index,* typically PDI $= s/r_{\mathrm{b}} < 5 \times 10^{-2}$, with r_{b} the averaged bubble radius and s the standard deviation.[3] When the values of the PDI are sufficiently low (say, below 5%), the bubbles are considered as monodisperse. Perfect monodispersity PDI $= 0$ can obviously never be achieved. Note that the monodispersity is essential when microbubbles are used as ultrasound contrast agents to improve the quality of an echographical image. In the case that microbubbles are used as drug carriers, very low values of the PDI index are also demanded in order to precisely control the amount of the drug delivered into the patient.

In this chapter we will describe and characterize in detail a novel process for the production of the type of microbubbles needed for therapeutical applications. More specifically, we propose a novel method for the production of $\simeq 5\,\mu$m bubbles with a PDI of 5% or better and at a production rate that exceeds 10^5 Hz.

Probably, the simplest way of producing monodisperse bubbles is to inject a small gas flow through an underwater nozzle.[14,15] Unfortunately, the bubbles released from a needle with a diameter of 5 μm into a stagnant reservoir of water is $\sim 50\,\mu$m, *much larger* than the injection needle diameter. Clearly, this method is not feasible for the production of monodisperse bubbles with potential therapeutical applications. However, it is known from the early works of Bragg and Nie[16] – who modeled the dynamic structure of crystals through a wet foam composed of monodisperse bubbles[17] – that bubbles with sizes comparable to the needle diameter can be

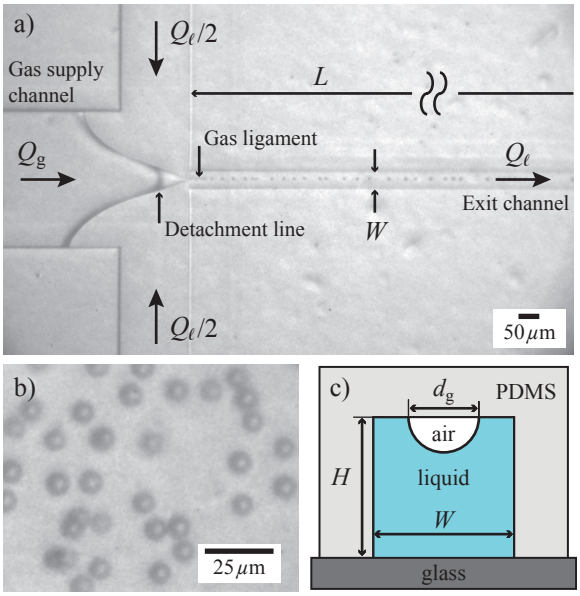

Figure 4.1: (a) High speed photograph showing the formation of microbubbles using our microfluidic flow-focusing geometry, $W = 50\,\mu$m, $L/W = 30$. The outer liquid flow forces the inner gas flow to form a tiny gas ligament that detaches from the channel wall and breaks up into microbubbles. The size of the microbubbles $d_b = 7.2\,\mu$m is much smaller than the channel width. The gas and liquid pressures are $p_g = 1555\,$mbar and $p_\ell = 1597\,$mbar, respectively, and the liquid flow rate is $U_\ell = 7.67\,\mathrm{m\,s^{-1}}$. (b) Microbubbles immediately after exiting the channel. (c) Schematic representation of a cross-section of the microfluidic channel downstream of the detachment line. The gaseous ligament dewets the PDMS channel wall.

generated when a small amount of gas is injected within a liquid crossflow[16] or a liquid co-flow.[18] Since then, it has been shown that micron-sized bubbles can be produced if a sufficiently small tube or channel through which a gas is injected, is placed in a strong liquid co-flow[14,19–25] or cross-flow.[26–33] Usually, the liquid is forced to flow thanks to an imposed pressure gradient. Farook *et al.* and Pancholi *et al.*[34–36] implemented the coaxial electrospray configuration described by Loscertales *et al.*[37] to generate 5 μm bubbles. In this particular case, the liquid co-flow is induced by the electrical tangential stresses. However, this production technique does not result in the formation of microbubbles with a sufficiently narrow size distribution.

An alternative way for the production of virtually monodisperse microbubbles at high and controlled production rates is to use a procedure called flow-focusing.[38–41] Here, a strong co-flow of liquid is created when

both the liquid and gas streams are forced to flow through a small constriction. Placing a cylindrical gas injection tube in front of an orifice of smaller diameter, Gañán-Calvo and Gordillo[42] produced bubbles with $d_b \sim O(10)\,\mu$m, which are typically *smaller* than the orifice diameter, by simply controlling the flow rate ratio. Indeed, the diameter d_b of the bubbles obtained in this way is given, approximately, by $d_b \propto (Q_g/Q_\ell)^\beta$, with $\beta \simeq 0.38 \simeq 2/5$, $Q_g/Q_\ell < 1$ and with Q_g and Q_ℓ indicating the gas and liquid flow rates, respectively.[42,43]

However, due to the fact that the alignment of the injection tube with the exit orifice is not an easy task, the parallelization of this type of axisymmetric devices for the mass production of microbubbles is not straightforward. Later on, Anna *et al.*,[44] Gordillo *et al.*[45] and Garstecki *et al.*[46] circumvented this limitation of axisymmetric flow focusing bubble makers by implementing the same geometry in planar devices. Planar microfluidic devices built using soft lithography techniques and incorporating the flow focusing geometry, are nowadays used by many research groups to produce monodisperse bubbles with therapeutical purposes.[47–50]

We stress that, though the flow focusing geometry in the planar version[46] is very similar to the axisymmetric one,[42] the physical mechanism leading to bubble formation is substantially different in both types of devices. For the axisymmetric case,[42] liquid velocities are such that the dimensionless groups We and Re satisfy $\mathrm{We} \gg 1$ and $\mathrm{Re} \gg 1$. Note that the Weber number, We, quantifies the relative importance of surface tension stresses with respect to liquid inertia and is defined as $\mathrm{We} = \rho U^2 W/\sigma$, with ρ, U and σ indicating the liquid density, the liquid mean velocity and surface tension coefficient respectively and W the transversal dimension of the exit channel. On the other hand, the dimensionless group that compares viscous stresses with respect to liquid inertia is the Reynolds number, defined as $\mathrm{Re} = \rho U W/\mu_\ell$, with μ_ℓ the liquid viscosity. Due to the fact that $\mathrm{We} \gg 1$ and $\mathrm{Re} \gg 1$, bubble formation in the experiments reported by Gañán-Calvo and Gordillo[42] is controlled by liquid inertia. However, the typical liquid flow rates injected in the planar version of flow focusing are so small (10^{-2} to $1\,\mu\mathrm{l}\,s^{-1}$), that $\mathrm{We} \ll 1$ and $\mathrm{Re} \lesssim 1$ and, in addition, the capillary numbers ($\mathrm{Ca} = \mu_\ell U/\sigma$) are typically such that $\mathrm{Ca} < 10^{-2}$.[46,51,52] Therefore, liquid inertia is negligible when compared to viscous shear stresses and viscous shear is not strong enough to overcome capillary pressure.[31] Under these conditions, bubbles block almost the whole cross section of the exit channel, forcing the carrier fluid to flow through thin wetting films strad-

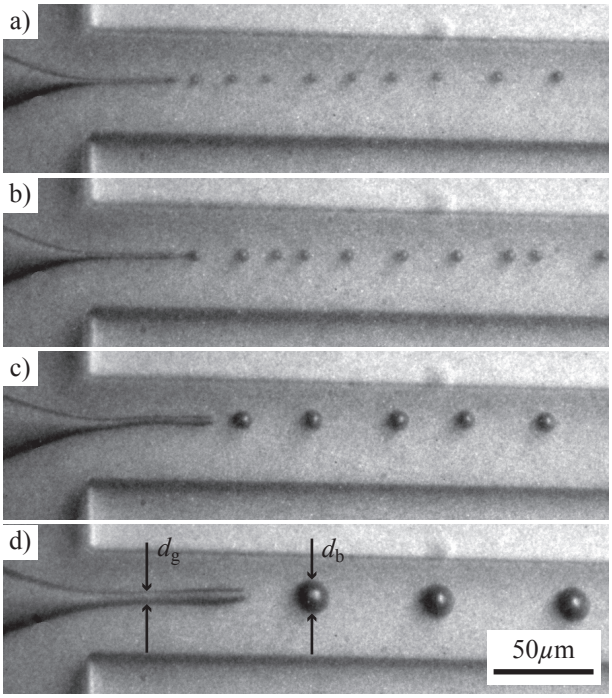

Figure 4.2: The size of the microbubbles produced can be accurately varied by adapting the gas and liquid flow rates by controlling their driving pressures. In order for $Q_g/Q_\ell \ll 1$, the gas pressure in the supplying vessel, p_g, is chosen to be very similar to that of the liquid, p_l. The operating conditions corresponding to each of the four images are: a) $p_\ell = 1800\,\text{mbar}$, $p_g = 1757\,\text{mbar}$, $U = 8.67\,\text{m}\,\text{s}^{-1}$, $d_b = 4.33\,\mu\text{m}$, $d_g = 2.60\,\mu\text{m}$; b) $p_\ell = 1800\,\text{mbar}$, $p_g = 1763\,\text{mbar}$, $U = 8.67\,\text{m}\,\text{s}^{-1}$, $d_b = 5.73\,\mu\text{m}$, $d_g = 2.92\,\mu\text{m}$; c) $p_\ell = 1410\,\text{mbar}$, $p_g = 1383\,\text{mbar}$, $U = 6.83\,\text{m}\,\text{s}^{-1}$, $Q_g = 0.0044\,\text{ml}\,\text{min}^{-1}$, $d_b = 10.05\,\mu\text{m}$, $d_g = 3.90\,\mu\text{m}$; d) $p_\ell = 1410\,\text{mbar}$, $p_g = 1463\,\text{mbar}$, $U = 6.83\,\text{m}\,\text{s}^{-1}$, $Q_g = 0.0134\,\text{ml}\,\text{min}^{-1}$, $d_b = 15.58\,\mu\text{m}$, $d_g = 5.84\,\mu\text{m}$. From this figure note that, as expected, for a fixed value of Q_ℓ (or p_ℓ), d_b increases as p_g increases.

dling at the walls of the device. This fact results in a significant increase of the liquid pressure upstream of the emerging bubble, leading to the 'squeezing' of the gas thread.[31] Except in the final stage of the collapse, in which gas inertia accelerates the bubble pinch-off process,[53,54] the mechanism of bubble formation is mainly controlled by the gas and liquid flow rates and by the device geometry.

A direct consequence of the geometrically controlled mechanism of bubble formation is that the polydispersity index of the bubbles generated through the 'squeezing' mechanism is below 5%; moreover, Garstecki *et al.* found that the bubble size can be expressed as a function of the ratio of gas and liquid flow rates as $d_b \propto (Q_g/Q_\ell)^{1/3}$. Note that the exponent 1/3, which differs from the exponent $\simeq 2/5$ that characterize bubble size in the axisymmetric flow focusing devices, already reflects the differences in the way bubbles are formed in both types of geometries. But there is an even more important difference between the two types of implementations: since bubbles block the exit channel in the planar version of flow focusing, the diameters of the bubbles formed in this way are necessarily larger than the width of the exit channel. Conversely, in the axisymmetric version of flow focusing devices, d_b is smaller than the exit orifice diameter as pointed out above.

This fact has an important consequence when bubbles are produced using the planar flow focusing geometry, namely, bubbles with sizes of the order of 5 μm obviously require the use of tiny microchannels of widths $W \approx 5\,\mu$m (see *e.g.* Hettiarachchi *et al.*[47]). We implemented the ing geometry incorporating exit channels of widths of 5 μm and experienced that these tiny channels tended to clog very easily due to the accumulation of impurities. Thus, we decided to find a different way for the production of 5 μm-bubbles that differed from the methods already existing in the literature.[46–51,53]

Here we describe a new method for the controlled production of $\sim$ 5 μm-bubbles with a polydispersity index below 5% at high production rates ($> 10^5$ bubbles/s) by means of a planar flow focusing device. The essential geometrical difference of our device with respect to *all* previous implementations is that the length of the exit channel L is much larger than its width, namely, $L/W \gg 1$, as depicted in Fig. 4.1. This, together with the fact that the imposed liquid and gas flow rates are such that $\mathrm{Re} \gtrsim 10^2$, $\mathrm{We} \gg 1$ and $Q_g/Q_\ell \ll 1$, enabling the production of bubbles in water with sizes one order of magnitude smaller than the channel width. In this

way, we are able to produce, in a single step, bubbles with sizes within the range needed for therapeutical applications whilst avoiding clogging problems. The final result, which we present in detail in the 'Results' section and derive in the 'Discussion' section, is that bubble size can be predicted based on the gas to liquid flow rate ratio and the fluid properties as

$$d_{\mathrm{b}}/W \simeq 2.75(\mu_{\mathrm{g}}/\mu_{\ell})^{1/12}(Q_{\mathrm{g}}/Q_{\ell})^{5/12}\,. \tag{4.1}$$

Eq. (4.1) is applicable *if* the gas and liquid flow rates satisfy the conditions $Q_{\mathrm{g}}/Q_{\ell} \ll 1$ and

$$\frac{Q_{\ell}}{Q_0} > 3\left(\frac{Q_{\mathrm{g}}}{Q_0}\right)^{-1/7}\,, \tag{4.2}$$

where the reference flow rate Q_0 is given by

$$Q_0 = \left(\frac{\sigma W^3}{\rho}\right)^{1/2}\,. \tag{4.3}$$

Note that the exponent 5/12 in Eq. (4.1), which differs from the exponents 1/3 and 2/5 to calculate bubble diameter as a function of the ratio Q_{g}/Q_{ℓ} reported in previous publications,[42,46] reveals that our method is different from those already published. The differences can be visually appreciated in Fig. 4.2: in our device, bubbles are formed after the formation of a long gas jet, whose diameter is much smaller than the channel width, and bubbles breakup up from its tip. The gas jet, which has a diameter of only a few microns, is formed at the entrance of the exit channel, where the liquid pressure gradient reaches its maximum value. To our knowledge, this is the first time that the existence of such tiny and stable gas jets within a microchannel is reported. Moreover, this is the first time that bubbles with a size of one-tenth the channel width are produced in a low viscosity liquid such as water. Since a long gas jet is created before bubbles are emitted from its tip, bubbles are not formed in the way described in Gañán-Calvo and Gordillo.[42] Clearly, since bubbles do not block the exit channel, they are not produced in the 'squeezing' regime described by Garstecki *et al.*[31,46,51] either. Let us point out that the advantage of microbubble formation in the way presented in this chapter as compared to the *squeezing* regime is that bubbles with sizes in the range of interest for medical applications ($d_{\mathrm{b}} \lesssim 5\,\mu$m) at frequencies that exceed 10^5 Hz are formed from a square microchannel of $50 \times 50\,\mu\mathrm{m}^2$ cross sectional area. This one order of magnitude reduction in bubble size with respect to channel width, avoids

the clogging of the exit channel and enormously decreases the pressures at which both the gas and the liquid need to be injected into the microfluidic device. Our procedure also allows us to easily vary the bubble volume over more than two orders of magnitude by simply varying the gas and liquid flow rates.

This chapter is organized as follows: in Sec. 4.2, we describe in detail the experimental procedure followed to generate micron-sized bubbles. In Sec. 4.3 we report the bubble formation frequencies as well as their associated PDI as a function of bubble diameter. In addition, we indicate the ranges of both the gas and liquid flow rates needed to create bubbles of less than $10\,\mu$m. For those readers interested in technical details, Eq. (4.1) and conditions (4.2)–(4.3) are deduced in Sec. 4.4. The final section is dedicated to presenting the conclusions of our study.

4.2 Materials and methods

The bubble generators were produced by soft lithography techniques. A mold was created from a negative photosensitive material (SU-8 GM 1060, Gersteltec SARL) and spin-coated on a silicon oxide substrate, to imprint a reticulable polymer PDMS (Poly(dimethylsiloxane), Sylgard 184, Dow Corning) which was irreversibly bounded to a glass cover plate in a plasma cleaner. We placed the microbubble-generating devices in an oven at 65° for one hour and they were used only after 24 hours to ensure the hydrophobicity of the PDMS. Note that, contrary to most microfluidic applications, we impose the hydrophobicity of the PDMS[52] since, in our case, the gas ligament should remain attached to the PDMS surface for stability purposes. The height of the microbubble maker is uniform and equal to $H = 50\,\mu$m and the width and length of the exit channel are, respectively, $W = 50\,\mu$m and $L = 1500\,\mu$m (see Fig. 4.1). Note that the main geometrical difference between our bubble generator and those used in previous studies[46,47,51,53] is that, in order for bubbles to be formed at the entrance region of the exit channel, our devices satisfy the condition $L/W \gg 1$. To avoid fluctuations in the gas flow rate, air was injected through a tube with 0.5 m in length and $50\,\mu$m of inner diameter. The air pressure, p_g, was controlled through a pressure regulator (Bosch Rexroth) and was measured using a digital manometer (Digitron 2000P). The continuous phase was distilled water with a 2% (w/v) of Tween 80 (Sigma Aldrich) added. The addition of the surfactant lowered the water-air interfacial tension coefficient to

$\sigma \simeq 40\,\mathrm{mN/m}$ and the contact angles with the PDMS and glass substrates were, respectively, $\theta_{\mathrm{PDMS}} = 89^\circ$ and $\theta_{\mathrm{glass}} = 39.5^\circ$. Since the liquid was supplied from a pressurized vessel instead of from a syringe pump, the liquid injection pressure, p_ℓ, was controlled and measured in the same way as the gas. The liquid flow rate Q_ℓ was determined by measuring the volume of liquid collected at the exit of the device during several minutes. The setup was placed under an inverted microscope (3000B Leica) which was connected to either a high-speed camera (Phantom V 7.3, with a resolution of 80×16 pixels and a field of view of $163 \times 33\,\mu\mathrm{m}^2$ when operated at an acquisition rate of 2×10^5 fps) or to an Intensified Retiga Fast camera (resolution of 1280×800 pixels, with a field of view of $415 \times 260\,\mu\mathrm{m}^2$). We checked the accuracy of reproducibility of the experiments. To take data, experiments were repeated twice for each couple of values p_ℓ, p_g: First, the bubbling frequency ω was determined using the high-speed camera. Second, in an independent experiment for the same parameters the bubble diameter d_b was measured from the high-resolution images taken with the intensified camera. Knowing ω and d_b, the volumetric gas flow rate was determined as $Q_\mathrm{g} = \pi d_\mathrm{b}^3 \omega/6$. We checked that the values of Q_g calculated in this way were practically identical – albeit more accurate – to those obtained assuming Poiseuille flow along the gas injection pipe.

4.3 Results

Fig. 4.1 shows a global view of the microchannel entrance region, which is where the microbubbles are formed. The figure reveals that – thanks to our choice $Q_\mathrm{g}/Q_\ell < 0.03$ – the gas filament contracts from the width of the gas supply channel ($400\,\mu\mathrm{m}$) to a steady ligament whose diameter is substantially smaller than W. Due to the fact that the height (H) of the device is equal to the width of the exit channel ($H = W \gg d_\mathrm{b}$), the gas thread separates from the lower glass surface at the region indicated as *detachment line* in Fig. 4.1. Indeed, since the PDMS substrate is less hydrophilic than the glass one ($\theta_{\mathrm{PDMS}} \simeq 90^\circ$ and $\theta_{\mathrm{glass}} = 39.5^\circ$), the narrow gas ligament, of diameter $d_\mathrm{g} \ll W$, is attached to the upper PDMS surface, as sketched in Fig. 4.1c. Once the steady gas ligament is formed, it breaks into uniformly sized bubbles with diameters $d_\mathrm{b} \sim d_\mathrm{g}$, as depicted in Fig. 4.2. In Fig. 4.3 we plot, as a function of d_b, the bubbling frequencies extracted from the analysis of the high speed videos and their corresponding values of the PDI calculated from the image analysis of the high resolution pictures.

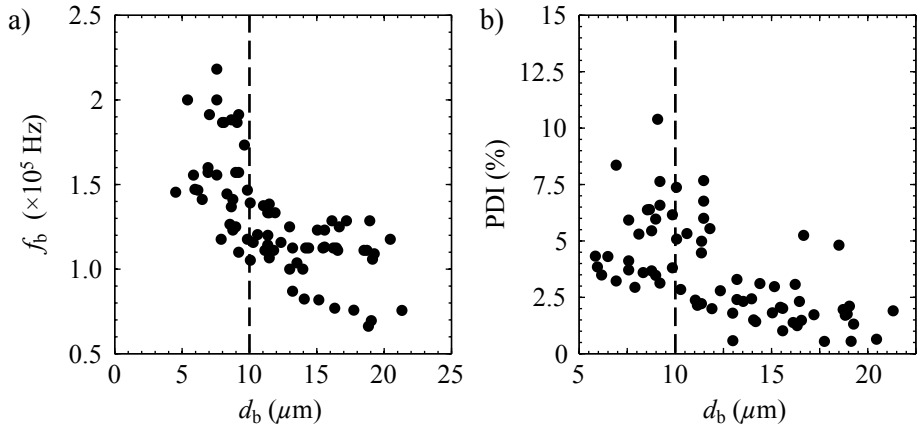

Figure 4.3: (a) Bubble formation frequencies as a function of bubble diameter. Note that all bubbles with diameters below $10\,\mu$m are produced at frequencies that exceed 10^5 Hz. (b) PDI index, in %, as a function of bubble diameter. Note that for many experimental conditions bubbles with diameters $d_b \simeq 5\,\mu$m can be produced with values of the PDI index below 5%. The reason for which the (apparent) PDI index is larger for some experiments is attributable to the fact that some images are out of the focus plane and are a bit blurred.

Clearly, Fig. 4.3 reveal that our procedure enables the production of bubbles with diameters $\simeq 5\,\mu$m and very low polydispersity index at frequencies that exceed 10^5 Hz.

We will now indicate the range of values of Q_ℓ and Q_g for which bubbles with sizes substantially smaller than the channel width, are produced. Note first that the mean liquid velocity along the exit channel, $U = Q_\ell/(W^2)$, needs to be above a certain threshold. Indeed, the liquid pressure decreases by an amount of $\Delta p_\ell \simeq \rho U^2$ from the detachment line to the inlet of the exit channel. Since the liquid pressure drop is much larger than the gas pressure variation in the same region, namely, $\Delta p_g \sim \mu_g Q_g/W^3$, the normal stress condition at the gas-liquid interface, when evaluated at the channel inlet can be expressed as $\rho U^2 \simeq 2\sigma/d_g$, implying $\mathrm{We_j} = \rho U^2\, d_g/\sigma > \mathrm{We_{min}} \simeq 2.5$. If d_g is expressed as a function of the ratio Q_g/Q_ℓ by means of Eq. (4.5) – deduced in the beginning of the next section – it is straightforward to show that the condition $\mathrm{We_j} > 2.5$ is equivalent to the one given by Eq. (4.2), which expresses that the liquid flow rate has to be above a certain threshold that depends on the gas flow rate. Moreover, in order to generate bubbles with sizes substantially smaller than the channel width, we also choose to impose the condition $Q_g/Q_\ell \leq 0.03$ *i.e.*, the liquid flow rate has

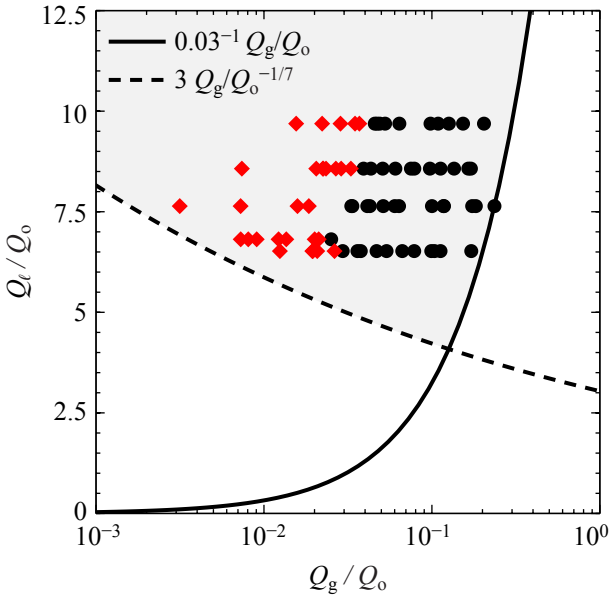

Figure 4.4: Values of the liquid and gas flow rates considered in this study. Liquid velocities were varied between $6\,\mathrm{m\,s^{-1}}$ and $8.5\,\mathrm{m\,s^{-1}}$, whereas the gas flow rate varied between $4 \times 10^{-4}\,\mathrm{ml\,min^{-1}}$ and $4 \times 10^{-2}\,\mathrm{ml\,min^{-1}}$. Diamonds indicate the operating conditions for which $d_\mathrm{b} < 10\,\mu\mathrm{m}$ whereas dots indicate $d_\mathrm{b} > 10\,\mu\mathrm{m}$. Note that the liquid and gas flow rates considered here satisfy the condition $Q_\mathrm{g}/Q_\ell \ll 1$ as well as the condition $Q_\ell/Q_0 > 3(Q_\mathrm{g}/Q_\ell)^{-1/7}$ given in Eq. (4.2). This latter condition is deduced from the fact that, in order for the gas ligament to be formed, the Weber number based on the gas ligament diameter namely, $\mathrm{We_j} = \rho U^2 d_\mathrm{g}/\sigma$ (see Fig. 4.2 for a definition of d_g), needs to be above a certain constant or order unity.

to be substantially larger than the gas one. Clearly, as depicted in Fig. 4.4, the different experiments considered in this study satisfy the conditions $Q_\mathrm{g}/Q_\ell \ll 1$ and that given in Eq. (4.2). The diamonds indicate the experimental data points for which bubbles with diameters below $10\,\mu\mathrm{m}$ are produced, these are of particular interest for the use as ultrasound contrast agents.

4.4 Discussion of the results

4.4.1 Scaling of the gas ligament diameter

Note first that, for the range of liquid velocities investigated here, $\mathrm{Re} = U d_\mathrm{b}/\nu_\ell \sim \mathcal{O}(10^2)$ with $\nu_\ell \simeq 10^{-6}\,\mathrm{m^2\,s^{-1}}$ the kinematic viscosity of water. This estimate indicates that the flow in the exit channel is laminar. Moreover, for the range of Reynolds numbers considered here, the entrance length is such that $L_\mathrm{e} \simeq 0.1 Q_\ell/\nu_\ell \simeq 1.5L$. Therefore, since the gas ligament breaks at a distance of $\sim H \ll L_\mathrm{e}$ from the duct inlet (see Fig. 4.2), bubbles are produced within the entrance region of the microchannel. In this entrance region, the liquid velocity profile is approximately uniform except at the thin boundary layers of typical width $\delta \ll W$ near the walls.[55]

Moreover, since the gas Reynolds number is such that $\mathrm{Re_g} = Q_\mathrm{g}/(\nu_\mathrm{g}\, d_\mathrm{b}) \sim \mathcal{O}(1)$, being ν_g the kinematic viscosity of air, the flow rate along the gas ligament can be calculated as

$$Q_\mathrm{g} = -K \frac{d_\mathrm{g}^4}{\mu_\mathrm{g}} \frac{\mathrm{d}p_\mathrm{g}}{\mathrm{d}x}\,, \tag{4.4}$$

where μ_g is the gas viscosity, K is a constant and $\mathrm{d}p_\mathrm{g}/\mathrm{d}x$ indicates the pressure gradient along the gas jet. Due to the fact that the cross-section of the ligament hardly varies downstream (*cf.* Fig. 4.2), $-\mathrm{d}p_\mathrm{g}/\mathrm{d}x$ approximately coincides with the liquid pressure gradient evaluated at the channel inlet, $-\mathrm{d}p_\ell/\mathrm{d}x = C\mu_\ell U/W^2$, with μ_ℓ the liquid viscosity and C is a constant that depends on the geometry of the channel and on the width δ of the liquid boundary layers at the channel walls. Note that the smaller δ, the larger C and therefore the liquid pressure gradient is maximal at the duct entrance.[55] For instance, in the particular case of a circular channel with a fully developed Poiseuille flow, for which $\delta \simeq W$, the pressure gradient is given by $-\mathrm{d}p_\mathrm{g}/\mathrm{d}x = 32\,\mu_\ell U/W^2$. Consequently, since $\delta \ll W$, the constant C satisfies $C \gg 32$.[55] Now, as expressed by Eq. (4.4), d_g decreases for a fixed value of Q_g when $-\mathrm{d}p_\mathrm{g}/\mathrm{d}x = -\mathrm{d}p_\ell/\mathrm{d}x = C\mu_\ell U/W^2$ increases. We conclude that, thanks to the large values of C – *i.e.*, thanks to the fact that bubbles are produced at the duct entrance – d_g can be reduced down to only a few microns, as depicted in Fig. 4.2. With $-\mathrm{d}p_\mathrm{g}/\mathrm{d}x = C\mu_\ell U/W^2$ Eq. (4.4) yields the following expression for d_g:

$$\frac{d_\mathrm{g}}{W} \propto \left(\frac{\mu_\mathrm{g}}{\mu_\ell}\right)^{1/4} \lambda^{1/4}\,, \tag{4.5}$$

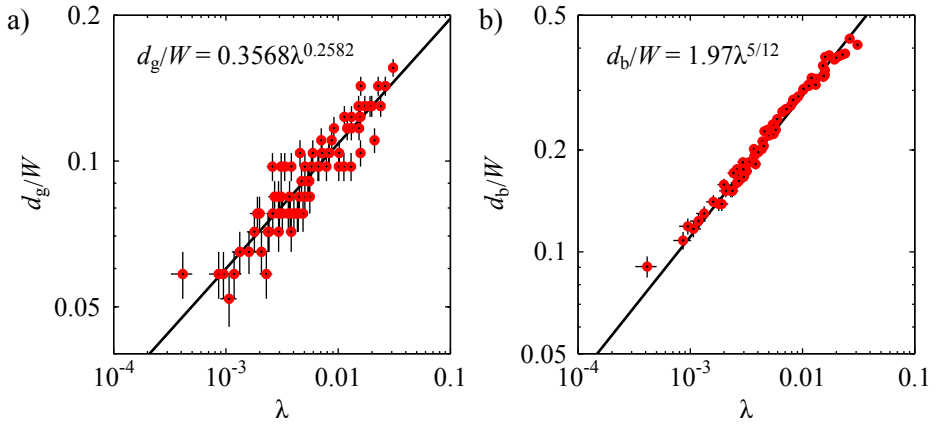

Figure 4.5: (a) Optically measured (minimal) width d_g of the gas ligament as function of the gas flow ratio λ. In spite of the large error bars associated to the fact that d_g is of the order of only a few microns, the best fit to the experimental data (straight line) closely follows the prediction $\propto \lambda^{1/4}$ given by equation (4.4). (b) Optically measured microbubble diameter d_b as function of the gas flow ratio, together with the scaling law $d_b/W \propto \lambda^{5/12}$ following from the presented scaling theory. Here the error bars are smaller as the bubbles are spherical and larger than the minimal width of the gas ligament.

where $\lambda = Q_g/Q_\ell$. Fig. 4.5 shows that the best fit to the experimental data follows very closely the prediction $d_g \propto \lambda^{1/4}$ of equation (4.5), validating our physical reasoning.

4.4.2 Bubble size

We now must only find the size of the bubbles as a function of d_g, U, and Q_g. First, note from Fig. 4.2 that the gas ligament breaks only slightly downstream of the channel inlet. At this location, the liquid pressure gradient is smaller than $C\mu_\ell U/W^2$ and thus, according to Eq. (4.4), d_g must increase in order to keep Q_g constant. Indeed, this is seen in Fig. 4.2. The increase in the jet diameter triggers the bubble formation process and also induces variations in the gas pressure gradient of the order of $\Delta(\mathrm{d}p_g/\mathrm{d}x) \sim \sigma/(d_g W)$.* Thus, since $C \gg 32$,[55] the relative variation of the gas flow rate is given by

$$\frac{\Delta Q_g}{Q_g} = \frac{\Delta(\mathrm{d}p_g/\mathrm{d}x)}{\mathrm{d}p_g/\mathrm{d}x} \sim \frac{1}{C}\frac{\sigma}{\mu_\ell U}\frac{W}{d_g} \ll 1\,. \tag{4.6}$$

*In this estimate it has been taken into account that the length of the gas ligament is $\simeq W$ (*cf.* Fig. 4.2)

The condition expressed by Eq. (4.6) means that bubbles are formed under constant flow rate conditions[21] and, consequently, the bubbling frequency is given by $\omega \propto U/d_g$.[14,21,42] Therefore, the bubble diameter can be easily calculated from the mass balance as

$$\frac{\pi\, d_b^3}{6} \propto Q_g \frac{d_g}{U} \rightarrow \frac{d_b}{W} \propto \left(\frac{\mu_g}{\mu_\ell}\right)^{1/12} \lambda^{5/12}. \tag{4.7}$$

Fig. 4.5b shows that once the proportionality constant is fixed to 2.75, Eq. (4.7) predicts the size of the bubbles formed with a maximum relative error of $\pm 10\%$. This maximum relative error corresponds to the minimum value of λ. We attribute this small discrepancy between experiments and theory to the fact that, for the smallest values of d_g, the gas ligament is embedded within the liquid boundary layer, resulting in a smaller local liquid velocity and thus an underestimation of λ.

4.5 Conclusions and Outlook

To conclude, we succeeded in producing monodisperse microbubbles in a controllable and reproducible way for microchannels with dimensions of tens of microns, avoiding clogging problems, and easily being able to adjust the microbubble size by varying the liquid and gas flow rates. We have provided the operating conditions in terms of the gas and liquid flow rates for which microbubbles with $d_b < 10\,\mu$m, thus in the size range required for medical applications, can be produced with very low values of the PDI index at frequencies that exceed 10^5 Hz. From the point of view of applications, our method is able to produce $\sim 10^{10}$ virtually monodisperse microbubbles with $d_b \simeq 5\,\mu$m with a total energy consumption of only ~ 200 J.

Moreover, we could theoretically account for this new regime of operation of the co-flow device: The central issues are an extremely low gas flow rate (as compared to the liquid flow rate) and a strong pressure gradient in the entrance region of the channel where the microbubbles form. The theory allows to derive the correct scaling laws for the microbubble size as function of the control parameters.

The next step will be to stabilize the formed bubbles by phospholipids or surfactants to prevent the bubbles dissolving or coalescing in the pool where they are trapped. If one succeeds, the new device allows for an alternative way to produce ultrasound contrast agents, with presumably a much narrower distribution of bubble sizes, *i.e.*, monodisperse bubbles.

For commercial applications one obviously has to go beyond PDMS devices (*e.g.*, silicon), to guarantee stable long time behavior. Another issue is the mass production for real applications, but the fact that our devices incorporate the flow focusing region in a planar geometry, facilitates the multiplexation of these types of devices.[56] Anyway, typically, the number of bubbles injected into a patient's blood stream is $\sim 10^{10}$ bubbles. Since this is the amount of bubbles generated by just one device during one day, one hundred of these devices working in parallel would create 100 doses a day with a power consumption of only $\sim 1\,\mathrm{W}$.

References

[1] R.N. Zúñiga and J.M. Aguilera, "Aerated food gels: fabrication and potential applications," *Trends Food Sci. Tech.* **19**, 176–187 (2008).

[2] K. S. Suslick and G. J. Price, "Applications of ultrasound to material chemestry," *Ann. Rev. Mat. Sci.* **29**, 295–326 (1999).

[3] E. Stride and M. Edirisinghe, "Novel microbubble preparation technologies," *Soft Matter* **4**, 2350–2359 (2008).

[4] E. Stride and R.J. Tang, M-X. Eckersley, "Physical phenomena affecting quantitative imaging of ultrasound contrast agents," *Appl. Acoust.* **70**, 1352–1362 (2009).

[5] S. M. van der Meer, B. Dollet, M. M. Voormolen, C. T. Chin, A. Bouakaz, N. de Jong, M. Versluis, and D. Lohse, "Microbubble spectroscopy of ultrasound contrast agents," *J. Acoust. Soc. Am.* **121**, 648–656 (2007).

[6] J. R. Lindner, J. Song, F. Xu, A. L. Klibanov, K. Singbartl, K. Ley, and S. Kaul, "Noninvasive ultrasound imaging of inflammation using microbubbles targeted to activated leukocytes," *Circulation* **102**, 2745–2750 (2000).

[7] K.W. Ferrara, M.A. Borden, and H. Zhang, "Lipid-shelled vehicles: Engineering for ultrasound molecular imaging and drug delivery," *Acc. Chem. Res.* **42**, 881–892 (2009).

[8] K. Ferrara, R. Pollard, and M. Borden, "Ultrasound microbubble contrast agents: Fundamentals and application to gene and drug delivery," *Ann. Rev. Biomed. Eng.* **9**, 415–447 (2007).

[9] Y.-Z. Zhao, H.-D. Liang, X.-G. Mei, and M. Halliwell, "Preparation, characterization and in vivo observation of phospholipid-based gas-filled microbubbles containing hirudin.." *Ultrasound Med. Biol.* **31**, 1237–1243 (2005).

[10] W. L. Nyborg, "Biological effects of ultrasound: Development of safety guidelines. Part II: General review," *Ultrasound Med. Biol.* **27**, 301–333 (2001).

[11] B. B. Jiang, C. Y. Gao, and J. C. Shen, "Polylactide hollow spheres fabricated by interfacial polymerization in an oil-in-water emulsion system," *Colloid Polym. Sci.* **284**, 513–519 (2006).

[12] C. Christiansen, H. Kryvi, P. Sontum, and T. Skotland, "Physical and biochemical characterization of Albumex^{TM}: A new ultrasound contrast agent consisting of air filled albumin microspheres suspended in a solution of human albumin," *Biotechnol. Appl. Biochem.* **19**, 307–320 (1994).

[13] M. Kukizaki and M. Goto, "Size control of nanobubbles generated from shirasu-porous-glass (spg) membranes," *J. Membr. Sci* **281**, 386–396 (2006).

[14] H. N. Oğuz and A. Prosperetti, "Dynamics of bubble growth and detachment from a needle," *J. Fluid Mech.* **257**, 111–145 (1993).

[15] R. Bolaños-Jiménez, A. Sevilla, C. Martínez-Bazán, and J. M. Gordillo, "Axisymmetric bubble collapse in a quiescent liquid pool. II. Experimental study," *Phys. Fluids* **20**, 112104 (2008).

[16] W. L. Bragg and J. F. Nie, "A dynamical model of a crystal structure," *Proc. Roy. Soc. Lond. A* **190**, 474–481 (1947).

[17] A. van der Net, W. Drenckhan, D. Weaire, and S. Hutzler, "The crystal structure of bubbles in the wet foam limit," *Soft Matter* **2**, 129–134 (2006).

[18] C. S. Smith, "On blowing bubbles for bragg's dynamic crystal model," *J. Appl. Phys.* **20**, 631 (1949).

[19] S. C. Chuang and V. W. Goldschmidt, "Bubble formation due to a submerged capillary tube in quiescent and coflowing streams," *ASME J. Basic Eng.* **92**, 705–711 (1970).

[20] A. Sevilla, J M Gordillo, and C. Martínez-Bazán, "Bubble formation in a coflowing airwater stream," *J. Fluid Mech.* **530**, 181–195 (2005).

[21] J. M. Gordillo, A. Sevilla, and C. Martínez-Bazán, "Bubbling in a co-flow at high Reynolds numbers," *Phys. Fluids* **19**, 077102 (2007).

[22] R. Suryo and O. A. Basaran, "Tip streaming from a liquid drop forming from a tube in a co-flowing outer fluid," *Phys. Fluids* **18**, 082102 (2006).

[23] A. S. Utada, A. Fernandez-Nieves, H. A. Stone, and D. A. Weitz, "Dripping to jetting transitions in coflowing liquid streams," *Phys. Rev. Lett.* **99**, 094502 (2007).

[24] P. Guillot, A. Colin, A. S. Utada, and A. Ajdari, "Stability of a jet in confined pressure-driven biphasic flows at low Reynolds numbers," *Phys. Rev. Lett.* **99**, 104502 (2007).

[25] A. G. Marín, F. Campo-Cortés, and J. M. Gordillo, "Generation of micron-sized drops and bubbles through viscous coflows," *Colloids Surf. A: Physicochem. Eng. Aspects* **344**, 2–7 (2009).

[26] S. E. Forrester and C. D. Rielly, "Bubble formation from cylindrical, flat and concave sections exposed to a strong liquid cross-flow," *Chem. Eng. Sci.* **53**, 1517–1527 (1998).

[27] T. Thorsen, R. W. Roberts, F. H. Arnold, and S. R. Quake, "Dynamic pattern formation in a vesicle-generating microfluidic device," *Phys. Rev. Lett.* **86**, 4163–4166 (2001).

[28] J. H. Xu, S. W. Li, Y. J. Wang, and G. S. Luo, "Controllable gas-liquid phase flow patterns and monodisperse microbubbles in a microfluidic T-junction device," *Appl. Phys. Lett.* **88**, 133506 (2006).

[29] K. Pancholi, E. Stride, and M. Edirisinghe, "Dynamics of bubble formation in highly viscous liquids," *Langmuir* **24**, 4388–4393 (2008).

[30] P. Guillot and A. Colin, "Stability of parallel flows in a microchannel after a T junction," *Phys. Rev. E* **72**, 066301 (2005).

[31] P. Garstecki, M. J. Fuerstman, H. A. Stone, and G. M. Whitesides, "Formation of droplets and bubbles in a microfluidic T-junction—scaling and mechanism of break-up," *Lab Chip* **6**, 437–446 (2006).

[32] V. van Steijn, C. R. Kleijn, and M. T. Kreutzer, "Flows around confined bubbles and their importance in triggering pinch-off," *Phys. Rev. Lett.* **103**, 214501 (2009).

[33] V. van Steijn, C. R. Kleijn, and M. T. Kreutzer, "Predictive model for the size of bubbles and droplets created in microfluidic T-junctions," *Lab Chip* **10**, 2513–2518 (2010).

[34] U. Farook, E. Stride, and M. Edirisinghe, "Preparation of suspensions of phospholipid-coated microbubbles by coaxial electrohydrodynamic atomization," *J. R. Soc. Interface* **6**, 271–277 (2009).

[35] K. P. Pancholi, U. Farook, E. Stride, and M. J. Edirisinghe, "Novel methods for preparing phospholipid coated microbubbles," *Eur. Biophys. J.* **37**, 515–520 (2008).

[36] U. Farook, E. Stride, and M. J. Edirisinghe, "Stability of microbubbles prepared by co-axial electrohydrodynamic atomisation," *Eur. Biophys. J.* **38**, 713–718 (2009).

[37] I. G. Loscertales, A. Barrero, I. Guerrero, R. Cortijo, M. Marquez, and A. M. Gañán-Calvo, "Micro/nano encapsulation via electrified coaxial liquid jets," *Science* **295**, 1695–1698 (2002).

[38] O. A. Basaran, "Small-scale free surface flows with breakup: drop formation and emerging applications," *AIChE J.* **48**, 1842–1848 (2002).

[39] A. Gunther and K.F. Jensen, "Multiphase microfluidics: from flow characteristics to chemical and materials synthesis," *Lab Chip* **6**, 1487–1503 (2006).

[40] A. Barrero and I. G. Loscertales, "Micro- and nanoparticles via capillary flows," *Annu. Rev. Fluid Mech.* **39**, 89–106 (2007).

[41] C. J. Martinez, "Bubble generation in microfluidic devices," *Bubble Science, Engineering & Technology* **1**, 40–52 (2009).

[42] A. M. Gañán-Calvo and J. M. Gordillo, "Perfectly monodisperse microbubbling by capillary flow focusing," *Phys. Rev. Lett.* **87**, 274501 (2001).

[43] A. M. Gañán-Calvo, "Perfectly monodisperse microbubbling by capillary flow focusing: An alternate physical description and universal scaling," *Phys. Rev. E* **69**, 027301 (2004).

[44] S. L. Anna, N. Bontoux, and H. A. Stone, "Formation of dispersions using "flow focusing" in microchannels," *Appl. Phys. Lett.* **82**, 364–366 (2003).

[45] J. M. Gordillo, Z. Cheng, M. Márquez, A.M. Gañán-Calvo, and D.A. Weitz, "A new device for the generation of microbubbles," *Phys. Fluids* **16**, 2828–2834 (2004).

[46] P. Garstecki, I. Gitlin, W. DiLuzio, G. M. Whitesides, E. Kumacheva, and H. A. Stone, "Formation of monodisperse bubbles in a microfluidic flow-focusing device," *Appl. Phys. Lett.* **85**, 1487–1503 (2004).

[47] K. Hettiarachchi, E. Talu, M.L. Longo, P.A Dayton, and A.P. Lee, "On-chip generation of microbubbles as a practical technology for manufacturing contrast agents for ultrasonic imaging," *Lab Chip* **7**, 463–468 (2007).

[48] E. Talu, K. Hettiarachchi, R.L. Powell, A.P. Lee, P.A. Dayton, and M.L. Longo, "Maintaining monodispersity in a microbubble population formed by flow-focusing," *Langmuir* **24**, 1745–1749 (2008).

[49] J.I. Park, Z. Nie, A. Kumachev, and E. Kumacheva, "A microfluidic route to small CO_2 microbubbles with narrow size distribution," *Soft Matter* **6**, 630–634 (2010).

[50] J. I. Park, E. Tumarkin, and E. Kumacheva, "Small, stable and monodisperse bubbles encapsulated with biopolymers," *Macromol. Rapid Commun.* **31**, 222–227 (2010).

[51] P. Garstecki, H. A. Stone, and G. M. Whitesides, "Mechanism for flow-rate controlled breakup in confined geometries: A route to monodisperse emulsions," *Phys. Rev. Lett.* **94**, 164501 (2005).

[52] P. Tabeling, "A brief introduction to slippage, droplets and mixing in microfluidic systems," *Lab Chip* **9**, 2428–2436 (2009).

[53] B. Dollet, W. van Hoeve, J.-P. Raven, P. Marmottant, and M. Versluis, "Role of the channel geometry on the bubble pinch-off in flow-focusing devices," *Phys. Rev. Lett.* **100**, 034504 (2008).

[54] J. M. Gordillo, A. Sevilla, J. Rodríguez-Rodríguez, and C. Martínez-Bazán, "Axisymmetric bubble pinch-off at high Reynolds numbers," *Phys. Rev. Lett.* **95**, 194501 (2005).

[55] L. Rosenhead, *Laminar boundary layers* (Dover Publications, New York, US, 1988).

[56] I. Kobayashi, T. Takano, R. Maeda, Y. Wada, K. Uemura, and M. Nakajima, "Straight-through microchannel devices for generating monodisperse emulsion droplets several microns in size," *Microfluid. Nanofluid.* **4**, 167–177 (2008).

Chapter 5 Bubble size prediction in co-flowing streams[§]

Abstract

In this chapter, the size of bubbles formed through the breakup of a gaseous jet in a co-axial microfluidic device is derived. The gaseous jet surrounded by a co-flowing liquid stream breaks up into monodisperse microbubbles and the size of the bubbles is determined by the radius of the inner gas jet and the bubble formation frequency. We obtain the radius of the gas jet by solving the Navier-Stokes equations for low Reynolds number flows and by minimization of the dissipation energy. The prediction of the bubble size is based on the system's control parameters only, *i.e.* the inner gas flow rate Q_i, the outer liquid flow rate Q_o, and the tube radius R. For a very low gas-to-liquid flow rate ratio ($Q_\mathrm{i}/Q_\mathrm{o} \to 0$) the bubble radius scales as $r_\mathrm{b}/R \propto \sqrt{Q_\mathrm{i}/Q_\mathrm{o}}$, independent of the inner-to-outer viscosity ratio $\eta_\mathrm{i}/\eta_\mathrm{o}$ and of the type of the velocity profile in the gas, which can be either flat or parabolic, depending on whether high-molecular-weight surfactants cover the gas-liquid interface or not. However, in the case in which the gas velocity profiles are parabolic and the viscosity ratio is sufficiently low, *i.e.* $\eta_\mathrm{i}/\eta_\mathrm{o} \ll 1$, the bubble radius scales as $r_\mathrm{b}/R \propto (Q_\mathrm{i}/Q_\mathrm{o})^\beta$, with β smaller than 1/2.

5.1 Introduction

The controlled formation of monodisperse microbubbles and microdroplets at high production rates is important in many industrial and medical applications. For example, the food industry seeks new methods to generate *en masse* monodisperse droplets and bubbles to accurately control the density and structure of a wide variety of materials.[1,2] In medical ultrasound

[§]Submitted to *Europhysics Letters* as: W. van Hoeve, B. Dollet, J. M. Gordillo, M. Versluis, and D. Lohse, "Bubble size prediction in co-flowing streams."

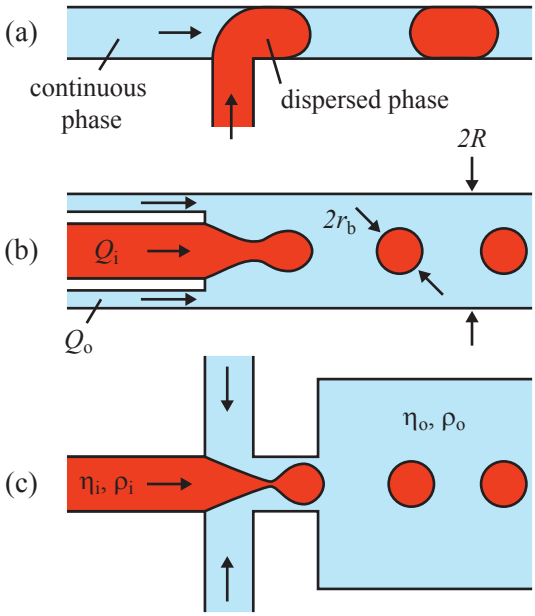

Figure 5.1: Schematic representation of the three main microfluidic geometries used for the formation of droplet and bubbles. The dispersed phase is injected (a) in a cross-flowing stream through a T-shaped junction, (b) in a co-flowing stream, and (c) in a focused stream imposed by the continuous phase.

imaging, microbubbles can be used as ultrasound contrast agents (UCA), where the resonance size of the bubble determines its acoustic response.[3,4] Commercially available UCA are produced using ultrasound-induced bubble formation methods, which results in a wide size distribution, *i.e.* UCA have a mean of 2 μm bubbles, but bubbles with a size between 1 μm and 20 μm exist in the population. Consequently, resonance occurs only for a small selection of bubbles. Improving the sensitivity in diagnostic imaging can thus be achieved by narrowing the size distribution so that more bubbles are at resonance size.

The use of microfluidic technology for the generation of these accurately produced droplets and bubbles has received considerable attention recently.[5–8] Various microfluidic geometries are used, for example, T-shaped devices,[9,10] co-flow, and flow-focusing geometries,[11–13] as is shown schematically in Fig. 5.1. In the latter, the dispersed phase is focused by the outer continuous phase to enter a narrow channel (see Fig. 5.1c). Droplets (or

bubbles) are formed in the 'dripping' mode or 'jetting' mode depending on the system's parameters. These include the inner and outer volumetric flow rates, Q_i and Q_o, the channel dimensions, and the fluid parameters (viscosity and surface tension). When the outer continuous flow rate Q_o is low, the droplets are generated in the dripping regime. In this regime, the dispersed phase enters the narrow channel and almost completely blocks the continuous phase. This leads to the formation of a neck, connecting the droplet to the inner feeding channel, that is gradually squeezed by the outer fluid until it breaks and a droplet is released.[14] In Raven *et al.*[15] this mode of operation was used to generate a wide variety of foams. For increasing gas fraction ($Q_\mathrm{i}/Q_\mathrm{o}$) foams are produced that consist of separated bubbles, to bubbly flow, to dry bamboo foam. Droplet formation in the dripping regime is characterized by droplets with a size comparable to the size of the channel and its droplet production rate is typically low.

When the outer liquid velocity is sufficiently high, such that the capillary number of the outer fluid $\mathrm{Ca}_\mathrm{o} = \eta_\mathrm{o}\tilde{u}/\gamma \geq 1$, with outer liquid viscosity η_o, velocity at the interface $\tilde{u}$, and surface tension γ, viscosity overcomes surface tension forces and an elongated jet is formed.[16–19] This regime is referred to as the jetting regime. The cylindrical jet breaks up in equally-sized fragments driven by the classical mechanism of droplet formation through a Rayleigh-Plateau instability driven by surface tension forces.[20] High-throughput monodisperse droplet formation in the jetting mode is of great value for industrial applications where a high-production rate is essential.

Utada *et al.*[21] and Utada *et al.*[16] presented a simple description of the droplet size in a liquid-liquid co-flowing microfluidic system with a geometry similar to that considered here. In their work, the inner liquid viscosity η_i is lower than the outer liquid viscosity η_o ($\eta_\mathrm{i}/\eta_\mathrm{o} \simeq 0.1$) and both the inner and outer flows are pressure driven; consequently, they exhibit Poiseuille-like velocity profiles (see Fig. 5.2a).

In this work we study microbubble formation through the breakup of a cylindrical jet in an axisymmetric gas-liquid co-flowing device formed by two coaxial tubes of circular section. Differently to the cases considered by Utada et al.,[16,21] we assume here an inner gas flow with negligible viscosity ($\eta_\mathrm{i} \ll \eta_\mathrm{o}$). Two different situations are considered depending upon whether the gas-liquid interface is free or rigidified by high-molecular-weight surfactants such as phospholipids, amphiphilic polymers, *etc.* These complex molecules are highly relevant in UCA microbubble formation[2] to avoid gas

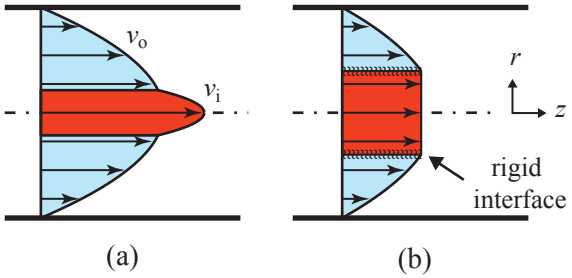

Figure 5.2: Velocity profiles for the inner and outer flow in a co-flowing stream. (a) Poiseuille velocity profile for both inner and outer flow for two co-flowing liquids, with $\eta_i < \eta_o$. (b) The inner gas flow shows a flat velocity profile, whereas the outer flow shows a Poiseuille profile. The rigid interface allows for a discontinuity of shear stress at the gas-liquid surface. The red core represents the inner phase.

dissolution into the carrier liquid. Notice that the main difference between the two situations studied here is that high-molecular-weight surfactants naturally populate the gas-liquid interface and form a rigid interface that greatly affect the inner flow boundary conditions (see Fig. 5.2b).

In this chapter we obtain a complete description of the radius of the inner gaseous jet and bubble size solely based on: the gas and liquid flow rates, the size of the channel, and the liquid properties. We first describe droplet and bubble formation in the absence of high-molecular-weight surfactants, following the calculation already presented in Utada *et al.*[21] We do so in preparation for the key new finding of this work in which bubble formation with high-molecular-weight surfactants at the interface is described. We use minimization of energy dissipation to close the system of equations describing these specific conditions.[22]

5.2 Droplet and bubble formation from a liquid or gas jet

In order to be able to highlight the analogies and differences between gas-liquid and liquid-liquid systems, we first repeat and elucidate the essence of the droplet-size calculation of Utada *et al.*[21] and then we extend this result to the case of bubbles. Let us consider the flow of two immiscible fluids without surfactants in an axisymmetric co-flow device, as depicted in Fig. 5.1b. These type of devices are typically fabricated by careful align-

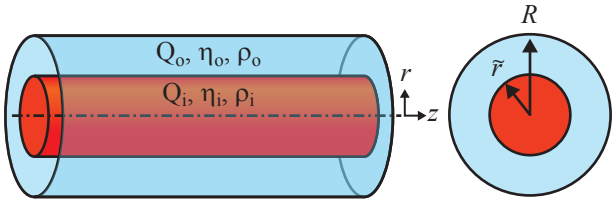

Figure 5.3: Coordinate system for an axisymmetric unperturbed inner jet with radius $\tilde{r}$ surrounded by a co-flowing liquid in a tube of radius R. Subscripts i and o refer to the inner and outer phase respectively.

ment of two coaxial capillaries: a tapered inner capillary for the supply of the dispersed phase and an outer capillary with radius R that delivers the continuous phase. When the outer liquid velocity is sufficiently high, such that viscous forces overcome surface tension forces ($\mathrm{Ca_o} \geq 1$), an elongated liquid jet is formed. In the case of the dispersed phase is a liquid, the cylindrical jet ultimately develops undulations driven by surface tension that lead to the jet disruption into droplets with sizes comparable to the jet diameter. This breakup mechanism is known as Rayleigh breakup[23]. The size of the droplets is $V = \lambda^\star \pi \tilde{r}^2$, where $\lambda^\star$ is the wavelength of the fastest growing disturbance and $\tilde{r}$ the unperturbed jet radius.

In this section we give an expression for the radius of the jet $\tilde{r}$ as a function of the inner and outer flow rates, Q_i and Q_o respectively, the properties of the two fluids, and the outer capillary tube radius R. The coordinate system that represents the initial state of the jet is shown in Fig. 5.3.

The Reynolds number, as a measure of the relative importance of inertial forces to viscous forces, is typically low in microfluidics, hence the fluid flow can be described using the steady-state Stokes equations for low Reynolds number flows,

$$0 = -\nabla p + \eta \nabla^2 u, \tag{5.1}$$

with pressure gradient ∇p, viscosity η, and the velocity u. Note also that, with independence of the value of the Reynolds number, Eq. (5.1) is still valid to describe strictly parallel streams, which is the case under consideration here. The velocity fields are obtained under the assumption of a no-slip boundary condition at the outer tube wall

$$u_\mathrm{o}(R) = 0, \tag{5.2}$$

continuity of velocity at the liquid-liquid interface

$$u_{\mathrm{o}}(\tilde{r}) = u_{\mathrm{i}}(\tilde{r}), \tag{5.3}$$

and continuity of shear stress

$$\eta_{\mathrm{o}} \left.\frac{\mathrm{d}u_{\mathrm{o}}}{\mathrm{d}r}\right|_{r=\tilde{r}} = \eta_{\mathrm{i}} \left.\frac{\mathrm{d}u_{\mathrm{i}}}{\mathrm{d}r}\right|_{r=\tilde{r}}. \tag{5.4}$$

The unperturbed flow of the inner jet resembles a perfect cylinder with constant radius $r = \tilde{r}$. The capillary pressure, *i.e.* the pressure difference across the interface, is given by the Young-Laplace equation

$$p_{\mathrm{i}} - p_{\mathrm{o}} = \frac{\gamma}{\tilde{r}}, \tag{5.5}$$

with γ the interfacial tension. Note that, since the radius of the cylinder is constant, the pressure gradient in both the inner and outer fluid are the same, and equal to ∇p.

Inserting the boundary conditions of Eq. (5.2), Eq. (5.3), and Eq. (5.4) into Eq. (5.1) and integrating gives an expression for the inner and outer liquid velocity profile

$$u_{\mathrm{i}}(r) = \frac{\nabla p}{4\eta_{\mathrm{i}}} \left\{ r^2 - \frac{\eta_{\mathrm{i}}}{\eta_{\mathrm{o}}} \left[1 + \left(\frac{\eta_{\mathrm{o}}}{\eta_{\mathrm{i}}} - 1 \right) \frac{\tilde{r}^2}{R^2} \right] R^2 \right\}, \tag{5.6}$$

$$u_{\mathrm{o}}(r) = -\frac{\nabla p}{4\eta_{\mathrm{o}}} \left(R^2 - r^2 \right). \tag{5.7}$$

The velocity for the inner disperse phase and the outer continuous phase as a function of the radial coordinate are schematically shown in Fig. 5.2a.

The volumetric flow rate is found from the integration of the flux over the cross-sectional area of the jet as $Q = 2\pi \int r u(r) \mathrm{d}r$ and, consequently, the flow rate ratio becomes[21]

$$\frac{Q_{\mathrm{i}}}{Q_{\mathrm{o}}} = \frac{\eta_{\mathrm{o}}}{\eta_{\mathrm{i}}} \frac{x^4}{\left(1 - x^2\right)^2} + \frac{2x^2}{1 - x^2}, \tag{5.8}$$

with $x = \tilde{r}/R$ the dimensionless jet radius. This equation can of course be inverted, leading to

$$x = \sqrt{\frac{X}{X+1}}, \text{ where } X = \frac{\eta_{\mathrm{i}}}{\eta_{\mathrm{o}}} \left(-1 + \sqrt{1 + \frac{\eta_{\mathrm{o}}}{\eta_{\mathrm{i}}} \frac{Q_{\mathrm{i}}}{Q_{\mathrm{o}}}} \right). \tag{5.9}$$

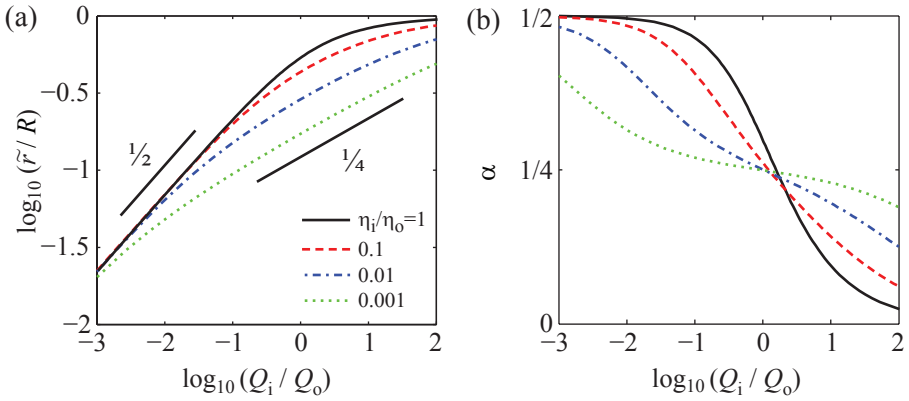

Figure 5.4: (a) Normalized radius of the inner jet as a function of the inner and outer volumetric flow rates for various viscosity ratios. The jet's radius decreases, while the maximum inner velocity increases, for decreasing inner-to-outer viscosity ratio. The radius of the jet scales as $\tilde{r} \propto (Q_\mathrm{i}/Q_\mathrm{o})^{\alpha}$. (b) Local slope $\alpha = \mathrm{d}\log(\tilde{r}/R)/\mathrm{d}\log(Q_\mathrm{i}/Q_\mathrm{o})$. In the limit of $Q_\mathrm{i}/Q_\mathrm{o} \to 0$ the size of the jet scales as $\tilde{r}/R = 2^{-1/2}\,(Q_\mathrm{i}/Q_\mathrm{o})^{1/2}$ independent of the viscosity ratio. For decreasing viscosity ratio $(\eta_\mathrm{i}/\eta_\mathrm{o})$ a scaling $\alpha = 1/4$ becomes pronounced.

The dimensionless jet radius x as a function of the flow rate ratio $(Q_\mathrm{i}/Q_\mathrm{o})$ for various inner-to-outer viscosity ratios is depicted in Fig. 5.4. It is shown here that, for $Q_\mathrm{i}/Q_\mathrm{o} \to 0$, the size of the jet $\tilde{r}/R = 2^{-1/2}\,(Q_\mathrm{i}/Q_\mathrm{o})^{1/2}$, independently of the viscosity ratio. The size of the jet is thus proportional to the square root of the flow rate ratio, a fact that was reported previously by various groups.[16–19] Note, however, that for the relevant case of bubble formation, *i.e.* $\eta_\mathrm{i} \ll \eta_\mathrm{o}$, the jet dimensionless radius is given by $\tilde{r}/R \propto (Q_\mathrm{i}/Q_\mathrm{o})^{\alpha}$ with $Q_\mathrm{i}/Q_\mathrm{o} < 1$ and $1/4 \leqslant \alpha \leqslant 1/2$ for a large range of values of the flow rate ratio. Indeed, in Fig. 5.4b the crossover of the local slope $\alpha = \mathrm{d}\log(\tilde{r}/R)/\mathrm{d}\log(Q_\mathrm{i}/Q_\mathrm{o})$ from the 1/2-scaling to the 1/4-scaling is shown for various viscosity ratios. Only for the limiting case of an inviscid gas, say $\eta_\mathrm{i}/\eta_\mathrm{o} \lesssim 0.001$, does the 1/4 scaling becomes pronounced. Note that a 1/4 scaling exponent is also observed in the co-flow device by Castro-Hernández *et al.*,[24] but under the different conditions of a strongly pressure gradient in the entrance region of the outer capillary.

For the case of drop formation, the cylindrical liquid jet is unstable against surface perturbations with a wavelength that exceeds the circumference of the jet $(\lambda > 2\pi\tilde{r})$.[25] The fastest growing disturbance $\lambda^\star$ that

leads to droplet pinch-off determines the droplet's volume $V = \pi\tilde{r}^2\lambda^\star$, with $\lambda^\star \approx 11.2\tilde{r}$ (for $\eta_\mathrm{i} = \eta_\mathrm{o}$),[26] hence the size of the droplets $r_\mathrm{d} \approx 2.03\tilde{r} \approx 1.44R\,(Q_\mathrm{i}/Q_\mathrm{o})^{1/2}$. However, for the case of gas jets ($\eta_\mathrm{i}/\eta_\mathrm{o} \ll 1$), since the period of bubble formation is proportional to $\pi R^2\tilde{r}(Q_\mathrm{i}/Q_\mathrm{o})$, bubble volume is calculated through the mass balance $4/3\pi r_\mathrm{b}^3/6 \propto \pi R^2 Q_\mathrm{i} \times \tilde{r}/Q_\mathrm{o}$.[24,27,28] This gives $r_\mathrm{b} \propto (Q_\mathrm{i}/Q_\mathrm{o})^\beta$, with the exponent β varying from the two limiting values $\beta = 0.5$ for $Q_\mathrm{i}/Q_\mathrm{o} \to 0$ ($\alpha = 0.5$) and $\beta = 5/12$ for $\eta_\mathrm{i}/\eta_\mathrm{o} \to 0$ ($\alpha = 1/4$), being these latter exponents firstly reported by Castro-Hernández *et al.*[24]

5.3 Bubble formation from a 'hollow jet'

We now come to the specific case of UCA microbubble formation through the breakup of a 'hollow jet'. The co-flowing outer liquid contains high-molecular-weight molecules like surfactants, proteins, and amphiphilic polymers that self-organize at the gas-liquid interface to form a coating around the bubble. This coating, or shell, ensures a much longer bubble lifetime in contrast to uncoated bubbles, therefore improving their stability, an essential condition for medical imaging.

In this section we give an expression for the size of the jet based on the inner gas and the outer liquid flow rates and under the assumption that the interface is rigidified by the surfactant solution.[29]

We solve the velocity fields in the Stokes equations (5.1) for an outer liquid flow rate with no-slip condition at the outer tube wall. We assume that the viscous stress imposed by the liquid is entirely balanced by the interface, hence that no stress is transmitted to the gas. This implies a homogeneous pressure distribution inside the jet, hence a flat velocity profile (see Fig. 5.2b).

The inner and outer velocity fields respectively read

$$u_\mathrm{i}(r) = \tilde{u} = \text{constant}, \tag{5.10}$$

with $\tilde{u}$ the velocity at the interface, and

$$u_\mathrm{o}(r) = -\frac{\nabla p}{4\eta_\mathrm{o}}\left(R^2 - r^2\right) + \frac{\log r/R}{\log \tilde{r}/R}\left(\tilde{u} + \frac{R^2 - \tilde{r}^2}{4\eta_\mathrm{o}}\nabla p\right). \tag{5.11}$$

Thus, the corresponding volumetric flow rates are given by

$$Q_\mathrm{i} = \pi\tilde{r}^2\tilde{u} \quad \text{and} \tag{5.12}$$

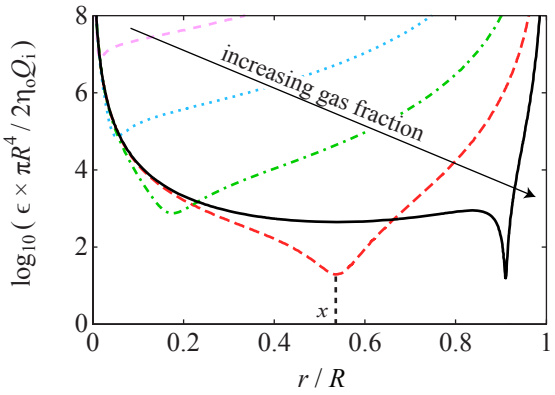

Figure 5.5: Energy dissipation ϵ as a function of the radius of the inner gas jet r_i, for gas-to-liquid flow rate ratios Q_i/Q_o equal to 0.001, 0.01, 0.1, 1, and 10 (arrow indicating increasing gas fraction). For each given Q_i and Q_o there exists a minimum energy dissipation in the system, which defines the optimum radius of the inner jet $x = \tilde{r}/R$.

$$\frac{Q_o}{2\pi} = \frac{R^4\left(1-x^2\right)}{16\eta_o}\nabla p\left(x^2-1+\frac{x^2-1-2x^2\log x}{\log x}\right) + \frac{Q_i}{\pi x^2}\frac{x^2-1-2x^2\log x}{4\log x}, \tag{5.13}$$

with $x = \tilde{r}/R$. In this expression the pressure gradient (∇p) and the radius of the jet ($x = \tilde{r}/R$) are unknown. Experimentally, both are selected by the system once the gas and liquid flow rates are imposed. Here, it is possible to close the problem by minimizing the viscous energy dissipation ϵ,[22]

$$\frac{\epsilon}{2\pi} = \eta_o \int_{\tilde{r}}^{R} r\left(\frac{\partial u_o}{\partial r}\right)^2 \mathrm{d}r\,. \tag{5.14}$$

Inserting Eq. (5.11) and Eq. (5.13) into Eq. (5.14) and simplifying gives

$$\frac{\epsilon}{2\pi\eta_o} = \frac{Q_i^2}{\pi^2 R^4}\left\{\frac{8\left(Q_o/Q_i - K(x)/2x^2\right)^2}{\left(1-x^2\right)\left(x^2-1+K(x)\right)^2} - \frac{1}{x^4\log x}\right\}, \tag{5.15}$$

with $K(x) = \left(x^2-1-2x^2\log x\right)/\log x$. Thus, the amount of energy that is dissipated into the system depends on both the inner and outer flow rate

and the radius of the jet, as is demonstrated in Fig. 5.5. The curves indicate the dissipation energy for fixed inner and outer volumetric flow rates and its minimum value marks the optimum radius x. The optimum radius as a function of the flow rates is found numerically by minimizing the energy dissipation function and is plotted in Fig. 5.6 (solid line).

The gaseous jet is inherently unstable[30] and will break up in bubbles by means of either a capillary instability or as a consequence of a pressure drop in the gas. In the case of bubbles are formed as a consequence of a capillary instability, the breakup of the gas jet is driven by the fastest growing disturbance. A linear stability analysis predicts that the optimum wavelength for the breakup of a gaseous jet surrounded by a liquid is slightly larger when compared to its inverted system—a liquid jet in air. The stability of a unconfined 'hollow jet' in ambient liquid was accomplished by Chandrasekhar,[25] who obtained that the size of the bubbles $r_\mathrm{b} \approx 2.15\tilde{r} \propto (Q_\mathrm{i}/Q_\mathrm{o})^{1/2}$. In confined geometries as the ones considered here, the prefactor of this relation will be somewhat different.[26,30] In this case the jet breaks as a consequence of a pressure drop in the gas stream and the bubble formation frequency is proportional to $R^2\tilde{r}/Q_\mathrm{o}$.[27,28] The bubble size can then be calculated from the mass balance $r_\mathrm{b}^3 \propto R^2\tilde{r}Q_\mathrm{i}/Q_\mathrm{o} \propto R^3(Q_\mathrm{i}/Q_\mathrm{o})^{3/2}$ and, thus, in this case, $r_\mathrm{b}/R \propto (Q_\mathrm{i}/Q_\mathrm{o})^{1/2}$. Therefore, independent of the source of the instability, the bubble size is proportional to the square root of the flow rate ratio.

5.4 Discussion and conclusion

In conclusion, we have expressed the radius of gas jets formed in axisymmetric co-flowing streams as a function the control parameters, *i.e.* the flow rates of both the continuous and the dispersed flows and the outer tube radius. The study has been divided in two parts, depending upon whether the gas-liquid interface contains high-molecular-weight surfactants to avoid the rapid dissolution of the gas into the carrier liquid. In the case where these complex molecules are not present it is found that, if the flow rate ratio is $Q_\mathrm{i}/Q_\mathrm{o} \to 0$, the diameter of the bubbles is proportional to the square root of the flow rate ratio, independent of the viscosity ratio. However, for finite values of the flow rate ratio $Q_\mathrm{i}/Q_\mathrm{o} < 1$ and very low values of the viscosity ratio, *i.e.* $\eta_\mathrm{i}/\eta_\mathrm{o} \ll 1$, the bubble radius scales as $r_\mathrm{b} \propto (Q_\mathrm{i}/Q_\mathrm{o})^\beta$, with β varying from the two limiting values (see Fig. 5.4) $\beta = 0.5$ for $Q_\mathrm{i}/Q_\mathrm{o} \to 0$ and $\beta = 5/12$ for $\eta_\mathrm{i}/\eta_\mathrm{o} \to 0$. This latter exponent

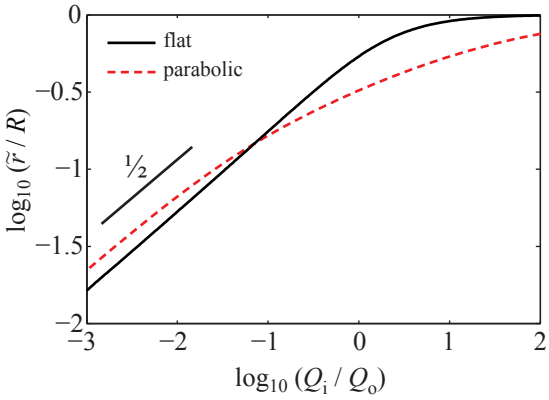

Figure 5.6: Optimum radius of the inner gas jet $\tilde{r}$ as a function of the gas-to-liquid flow rate ratio Q_i/Q_o. The solid line represents the optimum radius that is found from minimization of energy dissipation and under the assumption of a flat velocity profile. Alternatively, the system is described by two pressure driven co-flowing fluids (η_i, η_o), with parabolic velocity profiles for both the inner and outer phase for an air-water system ($\eta_o = 10^{-3}$ Pa·s, $\eta_i = 1.8 \times 10^{-5}$ Pa·s) (dashed line). For $Q_i/Q_o \to 0$, the slope is 1/2, indicating that the optimum radius scales with the square root of the flow rate ratio ($\tilde{r} \propto R\,(Q_i/Q_o)^{1/2}$).

was reported by Castro-Hernández *et al.*[24]

In the case that high-molecular-weight surfactants are added, we have found that the bubble radius is proportional to the square root of the flow rate ratio. Moreover, in Fig. 5.6 a comparison is made between the gas jet radius predicted based on an inner parabolic velocity profile (dashed line) and a flat velocity profile (solid line) for an air-water system (with viscosity of air $\eta_i = 1.8 \times 10^{-5}$ Pa·s and water $\eta_o = 10^{-3}$ Pa·s). It is demonstrated that for small gas fractions $Q_i \ll Q_o$ the influence of the inner flow conditions on the jet radius is marginal.

References

[1] S. van der Graaf, C. G. P. H. Schroën, and R. M. Boom, "Preparation of double emulsions by membrane emulsification—a review," *J. Membr. Sci.* **251**, 7–15 (2005).

[2] K. Hettiarachchi and A. P. Lee, "Polymer-lipid microbubbles for biosensing and the formation of porous structures," *J. Colloid Interface Sci.* **344**, 521–527 (2010).

[3] A. L. Klibanov, "Ultrasound contrast agents: Development of the field and current status," *Top. Curr. Chem.* **222**, 73–106 (2002).

[4] K. Hettiarachchi, E. Talu, M. L. Longo, P. A. Dayton, and A. P. Lee, "On-chip generation of microbubbles as a practical technology for manufacturing contrast agents for ultrasonic imaging," *Lab Chip* **7**, 463–468 (2007).

[5] A. Günther and K. F. Jensen, "Multiphase microfluidics: from flow characteristics to chemical and materials synthesis," *Lab Chip* **6**, 1487–1503 (2006).

[6] G. F. Christopher and S. L. Anna, "Microfluidic methods for generating continuous droplet streams," *J. Phys. D: Appl. Phys.* **40**, R319–R336 (2007).

[7] C. N. Baroud, F. Gallaire, and R. Dangla, "Dynamics of microfluidic droplets," *Lab Chip* **10**, 2032–2045 (2010).

[8] A. Nazir, C. G. P. H. Schroën, and R. M. Boom, "Premix emulsification: A review," *J. Membr. Sci.* **362**, 1–11 (2010).

[9] T. Thorsen, R. W. Roberts, F. H. Arnold, and S. R. Quake, "Dynamic pattern formation in a vesicle-generating microfluidic device," *Phys. Rev. Lett.* **86**, 4163–4166 (2001).

[10] C. Chen, Y. Zhu, P. W. Leech, and R. Manasseh, "Production of monodispersed micron-sized bubbles at high rates in a microfluidic device," *Appl. Phys. Lett.* **95**, 144101 (2009).

[11] A. M. Gañán-Calvo, "Generation of steady liquid microthreads and micron-sized monodisperse sprays in gas streams," *Phys. Rev. Lett.* **80**, 285–288 (1998).

[12] A. M. Gañán-Calvo and J. M. Gordillo, "Perfectly monodisperse microbubbling by capillary flow focusing," *Phys. Rev. Lett.* **87**, 274501 (2001).

[13] S. L. Anna, N. Bontoux, and H. A. Stone, "Formation of dispersions using "flow focusing" in microchannels," *Appl. Phys. Lett.* **82**, 364–366 (2003).

[14] P. Garstecki, H. A. Stone, and G. M. Whitesides, "Mechanism for flow-rate controlled breakup in confined geometries: A route to monodisperse emulsions," *Phys. Rev. Lett.* **94**, 164501 (2005).

[15] J.-P. Raven, P. Marmottant, and F. Graner, "Dry microfoams: formation and flow in a confined channel," *Eur. Phys. J. B* **51**, 137–143 (2006).

[16] A. S. Utada, A. Fernandez-Nieves, H. A. Stone, and D. A. Weitz, "Dripping to jetting transitions in coflowing liquid streams," *Phys. Rev. Lett.* **99**, 094502 (2007).

[17] A. M. Gañán-Calvo, R. González-Prieto, P. Riesco-Chueca, M. A. Herrada, and M. Flores-Mosquera, "Nature physics," *Nature Phys.* **3**, 737–742 (2007).

[18] A. G. Marín, F. Campo-Cortés, and J. M. Gordillo, "Generation of micron-sized drops and bubbles through viscous coflows," *Colloids and Surfaces A: Physicoch. Eng. Aspects* **344**, 2–7 (2009).

[19] E. Castro-Hernández, V. Gundabala, A. Fernández-Nieves, and J. M. Gordillo, "Scaling the drop size in coflow experiments," *New Journal of Physics* **11**, 075021 (2009).

[20] P. Guillot, A. Colin, A. S. Utada, and A. Ajdari, "Stability of a jet in confined pressure-driven biphasic flows at low Reynolds numbers," *Phys. Rev. Lett.* **99**, 104502 (2007).

[21] A. S. Utada, E. Lorenceau, D. R. Link, P. D. Kaplan, H. A. Stone, and D. A. Weitz, "Monodisperse double emulsions generated from a microcapillary device," *Science* **308**, 537–541 (2005).

[22] D. Stauffer, "Teaching Reiser's extremal principle for hydrodynamics," *Am. J. Phys.* **73**, 282–283 (2005).

[23] Lord Rayleigh, "On the capillary phenomena of jets," *Proc. R. Soc. London* **29**, 71–97 (1879).

[24] E. Castro-Hernández, W. van Hoeve, D. Lohse, and J. M. Gordillo, "Microbubble generation in a co-flow device operated in a new regime," (under review).

[25] S. Chandrasekhar, *Hydrodynamic and hydromagnetic stability* (Oxford Press, 1961).

[26] S. Tomotika, "On the instability of a cylindrical thread of a viscous liquid surrounded by another viscous fluid," *Proc. Roy. Soc. London* **150**, 322–337 (1935).

[27] H. N. Oğuz and A. Prosperetti, "Dynamics of bubble growth and detachment from a needle," *J. Fluid Mech.* **257**, 111–145 (1993).

[28] J. M. Gordillo, A. Sevilla, and C. Martínez-Bazán, "Bubbling in a co-flow at high reynolds numbers," *Phys. Fluids* **19**, 077102 (2007).

[29] N. D. Denkov, S. Tcholakova, K. Golemanov, K. P. Ananthpadmanabhan, and A. Lips, "The role of surfactant type and bubble surface mobility in foam rheology," *Soft Matter* **5**, 3389–3408 (2009).

[30] P. Guillot, A. Colin, and A. Ajdari, "Stability of a jet in confined pressure-driven biphasic flows at low Reynolds number in various geometries," *Phys. Rev. E* **78**, 016307 (2008).

Chapter 6 Breakup of diminutive Rayleigh jets[§]

Abstract

Discharging a liquid from a nozzle at sufficient large velocity leads to a continuous jet that due to capillary forces breaks up into droplets. Here we investigate the formation of microdroplets from the breakup of micron-sized jets with ultra high-speed imaging. The diminutive size of the jet implies a fast breakup time scale $\tau_c = \sqrt{\rho r^3/\gamma}$ of the order of 100 ns, and requires imaging at 24 million frames/s. We directly compare these experiments with a numerical lubrication approximation model that incorporates inertia, surface tension, and viscosity [Eggers and Dupont, *J. Fluid Mech.* **262**, 205 (1994); Shi, Brenner, and Nagel, *Science* **265**, 219 (1994)]. The lubrication model allows to efficiently explore the parameter space to investigate the effect of jet velocity and liquid viscosity on the formation of satellite droplets. In the phase diagram we identify regions where the formation of satellite droplets is suppressed. We compare the shape of the droplet at pinch-off between the lubrication approximation model and a boundary integral calculation, showing deviations at the final moment of the pinch-off. Inspite of this discrepancy, the results on pinch-off times and droplet and satellite droplet velocity obtained from the lubrication approximation agree with the high-speed imaging results.

6.1 Introduction

A narrow size distribution in droplet formation is important in many industrial and medical applications. For example, the controlled formation of (double)emulsions from microfluidic devices in T-shaped,[1,2] co-flow,[3] or flow-focusing geometries[4–6] is needed in many personal care products,

[§]Published as: W. van Hoeve, S. Gekle, J. H. Snoeijer, M. Versluis, M. P. Brenner, and D. Lohse, "Breakup of diminutive Rayleigh jets," *Physics of Fluids* **22**, 122003 (2010).

foods, and cosmetics. In food industry, the production of powders with a monodisperse particle size distribution through spray-drying results in a reduction of transportation and energy costs. In inkjet printing, monodisperse microdroplets are required to accurately control droplet deposition.[7] In drug inhalation technology, monodisperse droplets lead to an improved lung targeting.[8,9]

Highly monodisperse micrometer-sized droplet production is achieved in various droplet generators.[10–12] In continuous jet technology the breakup of a liquid jet emanating from a nozzle is stimulated by an acoustic wave, resulting in a continuous stream of droplets.[13] Piezoelectric drop-on-demand systems generate a well-defined piezo-driven pressure pulse into the (ink)-reservoir which forces a precisely controlled amount of liquid to detach from the nozzle.[14,15] In electrospray atomization a high voltage is applied to generate (sub)micron-sized droplets of conducting liquids.[16,17] However, for drug inhalation technology ideally one would need a low-cost droplet generator that is simple, light, and disposable. The typical size of nebulizer droplets is 2.5 μm in radius. Droplets that are too large do not penetrate into the deeper regions of the lungs, whereas droplets that are too small evaporate or are exhaled.[8,9] Inhaler sprays therefore need a well-controlled and narrow size distribution. The more sophisticated droplet generators involve the use of dedicated equipment and hence do not meet the criteria for this specific application.

The formation of droplets by the slow emission of a liquid from a nozzle (*e.g.* a leaking faucet) forms a pendant droplet that grows slowly, characterized by a quasi-static balance between inertial and surface tension forces.[18–21] The droplet formation mechanism in this regime is associated as 'dripping'. It is known that the shape of the nozzle opening can dramatically influence the size of the droplets.[22] Droplet formation in the dripping regime typically produces large droplets at low production rates.

When the liquid flow rate is progressively increased such that the liquid velocity v is sufficiently large such that the kinetic energy overcomes the surface energy a continuous liquid jet is formed. The lower critical velocity for jet formation can be expressed in terms of the Weber number

$$\mathrm{We} = \frac{\rho_\ell r v^2}{\gamma} > 4, \tag{6.1}$$

with radius of the jet r, liquid density ρ_ℓ, and surface tension γ.[23] The formation of a jet, that is inherently unstable, gives rise to the next droplet formation regime, where droplets are generated by the spontaneous breakup

of the jet to minimize its surface energy. Droplet formation by 'jetting' a liquid is referred to as 'Rayleigh breakup' as described by Plateau[24] and Lord Rayleigh[25] more than a century ago. A small disturbance introduced by mechanical vibrations or by thermal fluctuations will grow when its wavelength exceeds the circumference of the jet. The optimum wavelength for an inviscid liquid jet is expressed as $\lambda_{\text{opt}} = 2\sqrt{2}\pi r$ and is determined by the jet radius only.[25] The system automatically selects this optimum wavelength and breaks up in fixed fragments of volume $\lambda_{\text{opt}}\pi r^2$, which then determines the droplet size. The size of the droplets is thus governed by the geometry of the system and it is independent on the jetting velocity.

When the liquid velocity is further increased the relative velocity between the jet and the ambient air can no longer be neglected. Aerodynamic effects accelerate the breakup process and a shortening of the length from the nozzle exit to the location of droplet pinch-off is observed. A transition from the 'Rayleigh breakup' regime to the first wind-induced breakup regime occurs when the inertia force of the surrounding air reaches a significant fraction of the surface tension force, such that the Weber number in gas is

$$\text{We}_{\text{g}} = \frac{\rho_g}{\rho_\ell}\text{We} > 0.2, \tag{6.2}$$

with ρ_{g} the density of the gas.[23,26]

Figure 6.1 shows a classification of droplet formation regimes based on the radius of the jet r and the liquid velocity v. All the lines in the figure are indicated for pure water. Droplet formation through the breakup of a continuous liquid jet in the Rayleigh breakup regime ('jetting') is bounded by a lower and upper critical velocity of 5 m/s and 35 m/s respectively for a 10 μm radius jet, and 17 m/s and 110 m/s for a 1 μm jet. From a practical prospective, the velocity operating range for Rayleigh breakup becomes wider for decreasing jet size. The size of the droplets is governed by the jet radius and is independent of the jetting velocity. This makes it the favorable regime for high-throughput monodisperse microdroplet formation. A complete overview on liquid jet breakup has recently been given by Eggers and Villermaux.[30]

Droplet formation by dripping from the tip of a nozzle or through the breakup of a continuous liquid jet has been extensively studied both experimentally and numerically. In the work of Wilkes *et al.*[31] a two-dimensional finite element method (FEM) is used to study the formation of droplets and a comparison is made to high-speed imaging results recorded at 12,000 frames per second (fps). Hilbing *et al.*[32] used a non-linear boundary ele-

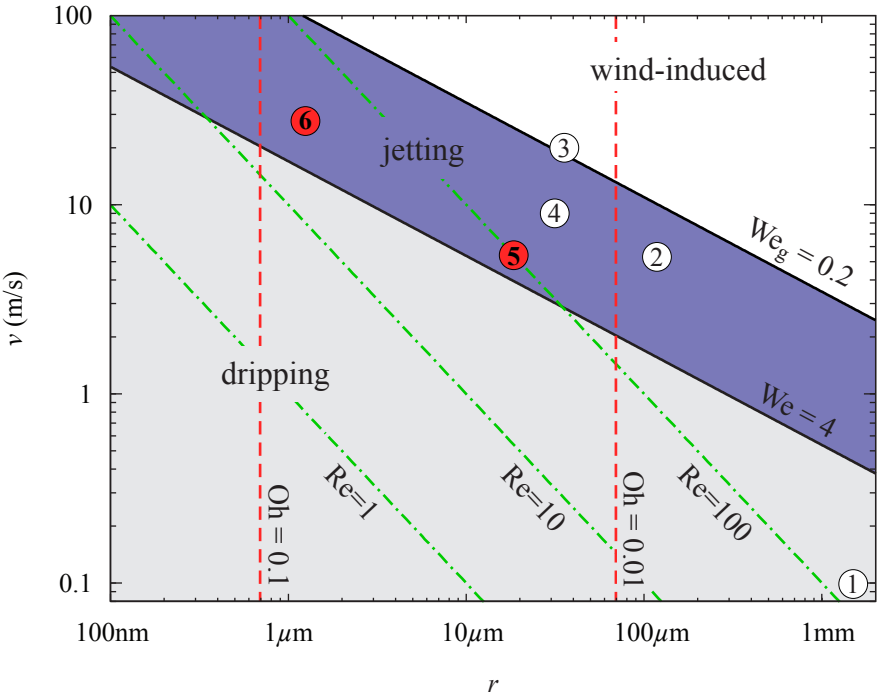

Figure 6.1: Classification of droplet formation regimes for a liquid discharging from an orifice of radius r with liquid velocity v. Droplet formation through the Rayleigh breakup mechanism in jetting is bounded by a lower and upper critical jet velocity (*c.f.* the area labeled "jetting"), expressed in terms of the Weber number $\mathrm{We} = \rho_\ell v^2 r/\gamma > 4$ and $\mathrm{We_g} = (\rho_\mathrm{g}/\rho_\ell)\mathrm{We} < 0.2$ respectively. The lines shown correspond to the Weber number, Reynolds number ($\mathrm{Re} = \rho_\ell v r/\eta$), and Ohnesorge number ($\mathrm{Oh} = \eta/\sqrt{\rho_\ell r \gamma}$) for pure water (with density $\rho_\ell = 1000\,\mathrm{kg/m^3}$, surface tension $\gamma = 72\,\mathrm{mN/m}$, and viscosity $\eta = 1\,\mathrm{mPa{\cdot}s}$). The encircled numbers (1–4) refer to droplet formation studies performed by Ambravaneswaran *et al.*,[19] Kalaaji *et al.*,[27] González & García,[28] and Pimbley & Lee[29] respectively; in this work we study diminutive Rayleigh jets using ultra high-speed imaging at 500 kfps (5) and 14 Mfps (6).

ment method (BEM) to study the effect of large amplitude periodic disturbances on the breakup of a liquid jet into droplets. In the work of Moseler and Landman a molecular dynamics (MD) simulations for nanometer-sized jets was presented.[33]

Fully three-dimensional or axisymmteric analysis of free-surface flows in droplet formation represents a complicated and computationally intensive task. The use of one-dimensional (1D) simplified models based on the lubrication approximation became standard since the work of Eggers and Dupont,[34] Shi, Brenner and Nagel,[35] and Brenner *et al.*[18] Application of the lubrication approximation offers a fast computational algorithm for describing free-surface flows, while incorporating the effect of inertia, surface tension, and viscosity. Many groups have successfully implemented the lubrication approximation to study the dynamics of droplet formation (in both 'dripping' and 'jetting') and the predictions are remarkable accurate in comparison to results obtained experimentally or by more complex numerical simulations. In Ambravaneswaran *et al.*[36] the performance of a one-dimensional model based on the lubrication approximation is evaluated by comparing it with the predictions obtained from a two-dimensional FEM calculations. Ambravaneswaran *et al.*[19] studied the formation of a sequence of hundreds of droplets by dripping from a nozzle using a one-dimensional model based on the lubrication approximation and compared the rich nonlinear dynamics with experimental results. In Yildirim *et al.*[37] it is stated that results obtained from a one-dimensional model can be used to improve the accuracy of the *drop weight method* to accurately measure the surface tension of a liquid. In Furlani *et al.*[38] a one-dimensional analysis of microjet breakup is studied within the lubrication approximation and validated using volume of fluid simulations.

Relatively little attention has been given to the experimental validation of such models in predicting the formation of microdroplets from the breakup of microjets. A study on the dynamics of these microscopically thin jets is experimentally extremely difficult due to the small length and time scales involved.[11] The local thinning of the liquid microjet followed by the droplet pinch-off is an extremely fast process. If the liquid viscosity can be safely neglected—*i.e.*, when the Ohnesorge number

$$\mathrm{Oh} = \frac{\eta}{\sqrt{\gamma \rho_\ell r}} \ll 1, \tag{6.3}$$

with liquid viscosity η—the collapse is driven by a balance between inertial and surface tension forces. The relevant time scale is then given by the

capillary time

$$\tau_c = \sqrt{\frac{\rho_\ell r^3}{\gamma}}. \tag{6.4}$$

In the specific case for the breakup of a 1 μm liquid jet, the capillary time is of the order of 100 nanoseconds.

In this chapter we study microdroplet formation from the breakup of a continuous liquid microjet experimentally using ultra high-speed imaging and within a 1D lubrication approximation model. We focus on two distinct cases for different jet sizes. In this study the Bond number $\mathrm{Bo} = g\rho r^2/\gamma$ for both cases is small, $\mathrm{Bo} \sim O(10^{-6})$, and hence gravity does not play a role. First, we resolve the breakup of a 18.5 μm jet (*cf.* number 5 in Fig. 6.1) at a high spatial and temporal resolution, such that the smallest structures (*i.e.* satellite droplets) can be studied in great detail. We make a direct comparison between the high-speed imaging results captured at 500 kfps and those obtained from the 1D model calculation for this specific case. One of the key contributions of this work is to demonstrate the good agreement between the experimental and lubrication approximation results, which to date have never been established before on such a small time and length scale (*cf.* the encircled numbers 1–4 indicating existing studies presented in literature in Fig. 6.1). For the second case we push towards the experimental limit (number 6 in the same figure) and provide ultra high-speed imaging results recorded at 14 Mfps (corresponding to 73 ns interframe time) of microdroplet formation from the breakup of a 1 μm diminutive jet. On this scale van der Waals forces and thermal fluctuations could become important, but here we show that the contribution of these forces is negligible and that the 'standard' dimensionless analysis indeed carries on down to the microscale.

The chapter is organized as follows. In Sec. 6.2 we briefly describe the one-dimensional model based on the lubrication approximation. The experimental setup to resolve the extremely fast droplet formation process is described in Sec. 6.3, while the results are presented in Sec. 6.4. Sec. 6.3 and 6.4 are divided into two sub-sections for both cases of jet breakup: for a microjet (A) and for a diminutive jet of 1 μm in size (B). In Sec. 6.5 a comparison is made between the 1D model and a boundary integral calculation. A discussion and concluding remarks are given in Sec. 6.6.

6.2 Lubrication approximation

Numerical simulations of jet breakup are carried out by solving the Navier-Stokes equations within the lubrication approximation as described in detail in the work by Eggers and Dupont[34] and Shi, Brenner and Nagel.[35] It was shown that droplet formation—*e.g.*, from a dripping faucet—can be predicted within great accuracy by solving the Navier-Stokes equations in a one-dimensional approximation obtained from a long-wavelength expansion. We apply the very same technique to model microdroplet formation from the breakup of an axisymmetric liquid microjet emanating from a circular orifice. The geometry of the system is schematically shown in Fig. 6.2(c). For small perturbations of the jet, the radial length scale is very much smaller than the longitudinal length scale and it is therefore appropriate to apply the lubrication approximation. We note, however, that close to break-up this approximation is no longer justified. One of the key questions is to investigate whether this influences the prediction of the breakup phenomenon.

Here we briefly review the main steps leading to the lubrication equations. The state of the system is described by the pressure field p and the velocity field v. A Taylor series expansion around $r = 0$ is obtained for both the velocity component in the z-direction v_z and the pressure field p. The velocity component in the z-direction is represented by a uniform base flow v_0 with a second-order correction term. The velocity in the radial direction v_r follows from continuity. The linearized equations are inserted in the full Navier-Stokes equations in cylindrical form and keeping only the lowest order in r.

The system is closed by applying the boundary conditions for the normal and tangential force on the jet surface. The normal force is balanced by the Laplace pressure, which gives the pressure jump across the interface. For the thin jet of our experiment at moderate jetting velocity, the breakup is not influenced by the surrounding air and the tangential force is set to zero. Applying these boundary conditions gives the reduced form of the Navier-Stokes equations

$$\frac{\partial v}{\partial t} + vv' = -\frac{\gamma}{\rho_\ell} C' + \frac{3\eta}{\rho_\ell} \frac{\left(h^2 v'\right)'}{h^2}, \tag{6.5}$$

where h is the radius of the jet, v is the liquid velocity, and prime denotes the derivative with respect to the axial-coordinate z. The curvature of the

interface C is given by

$$C = \frac{1}{R_1} + \frac{1}{R_2} = \frac{1}{h\sqrt{1+h'^2}} - \frac{h''}{\left(1+h'^2\right)^{3/2}}. \tag{6.6}$$

The interface moves with the velocity field as

$$\frac{\partial h^2}{\partial t} + \left(vh^2\right)' = 0. \tag{6.7}$$

The set of linear equations, *i.e.* Eq. (6.5), (6.6), and (6.7), is solved using an explicit scheme ODE solver in MATLAB (The Mathworks Inc., Natick, MA, USA).† A fixed number of grid points are homogeneously distributed from the nozzle exit to the tip of the jet.

As the initial condition for the shape of the jet, we used a hemispherical droplet described by $h = \sqrt{h_0^2 - z^2}$ (see Fig. 6.2(c)), with h_0 the initial radius of the jet at the nozzle exit, and axial coordinate z containing 1000 grid points, homogeneously distributed between the nozzle exit (at $z = 0$) and the tip of the jet at $z = h_0$. The initial jetting velocity v_{jet} was constant along the z-axis. A modulation of the nozzle radius is applied in the numerical simulations to initiate jet breakup, mimicking thermal fluctuations. The amplitude of variation of the jet radius at the nozzle exit is small, $\delta/h_0 \approx 0.005$.

$$h_{\text{nozzle}} = h_0 + \delta \sin 2\pi f t \tag{6.8}$$

with f the driving frequency. To assure a constant flow rate Q through the nozzle, the velocity was modulated correspondingly,

$$v_{\text{nozzle}}(t) = \frac{h_0^2 v_{\text{jet}}(t)}{h_{\text{nozzle}}^2}. \tag{6.9}$$

The driving frequency of the modulation is chosen such that it matches the optimum wavelength for jet breakup ($f = v_{\text{jet}}/\lambda_{\text{opt}}$). The amplitude of the wave grows until it equals the radius of the jet and a droplet pinch-off occurs. The moment of droplet pinch-off is defined as the moment where the minimum width of the jet is below a threshold value, which in our

† When scaling all lengths with the jet radius r and time with capillary time τ_c, these equations indeed only contain two dimensionless parameters: the Ohnesorge number Oh, expressing the importance of the viscous term, and the Weber number We, expressing the jet velocity.

simulations we set to $0.001h_0$. After pinch-off all grid points between the nozzle exit and the pinch-off location were redistributed and the calculations continued until another droplet was formed. After droplet pinch-off, the continuous jet and the detached droplet where calculated individually. When a droplet meets another droplet (or jet) the two objects where combined to simulate droplet coalescence. Droplet coalescence is defined when two objects overlap with a critical distance $0.005h_0$.

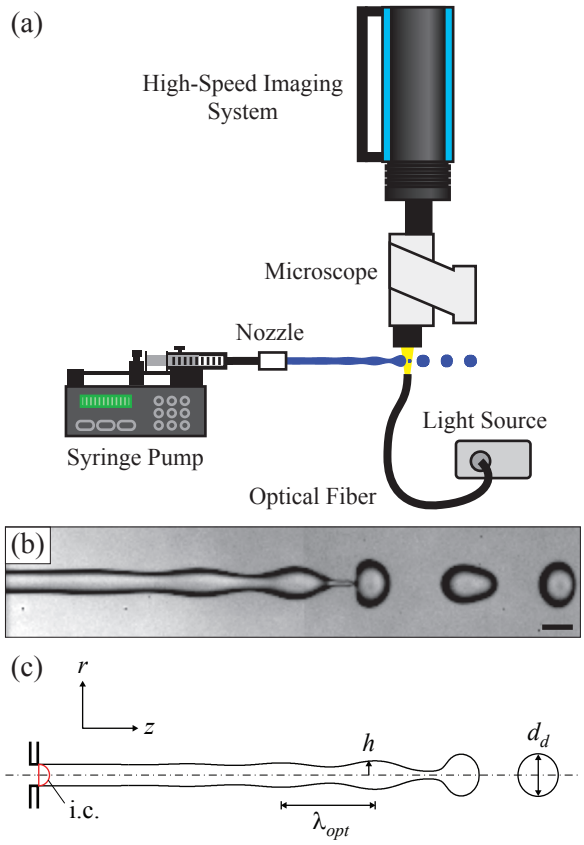

Figure 6.2: (a) Schematic overview of the experimental setup to visualize the extremely fast breakup of a liquid microjet into droplets. (b) Snapshot of a high-speed imaging recording of the breakup of a 18.5 μm radius jet. The scale bar denotes 50 μm. (c) Coordinate system. The initial condition (i.c.) of the system is indicated by the solid red line.

6.3 Experimental setup

The experimental study of microjet breakup is extremely challenging due to the small length and time scales involved. This section describes the experimental setup that is used to visualize the breakup of liquid microjets. We consider two different systems—first for the breakup of a 18.5 μm liquid microjet, and second, for a diminutive jet under the extreme condition for resolving its breakup using visible light microscopy.

6.3.1 Microjets (18.5 μm)

Fig. 6.2(a) shows the experimental setup to visualize the formation of microdroplets from the breakup of a continuous liquid microjet. An aqueous solution of 40% w/w glycerol, dissolved in a 0.9% w/w saline solution (with $\rho_\ell = 1098\,\mathrm{kg/m^3}$, $\eta = 3.65\,\mathrm{mPa{\cdot}s}$, and $\gamma = 67.9\,\mathrm{mN/m}$), was supplied at a constant flow rate Q of 0.35 ml/min through a high-precision syringe pump (accuracy 0.35%) (PHD 22/2000, Harvard Apparatus, Holliston, MA). The addition of sodium chloride prevents the droplets from charging and avoids deflection of the jet when it exits the nozzle. The liquid is forced to flow through a silicon micro machined nozzle chip (Medspray XMEMS bv, The Netherlands). The nozzle chip consist of a rectangular opening of aspect ratio 8:1 ($W \times H = 89\,\mu\mathrm{m} \times 11\,\mu\mathrm{m}$). This leads to a jet of non-circular cross-section, with the major/minor axis switching along the jet.[25,39] The oscillation is damped out by viscosity and once the jet gets back to a cylindrical shape its radius is measured to be $r = 18.5\,\mu$m. The jet velocity v_{jet} is calculated from the imposed liquid flow rate and the cross-sectional area of the jet A as $v_{\mathrm{jet}} = Q/A = 5.4\,\mathrm{m/s}$, with $A = \pi r^2$. The experimental conditions are expressed by the dimensionless Reynolds number (Re), Weber number for the liquid (We), Weber number for the ambient gas ($\mathrm{We_g}$), and the Ohnesorge number (Oh). The Reynolds number $\mathrm{Re} = \sqrt{\mathrm{We}}/\mathrm{Oh} \approx 30$, assuring that the flow remains laminar. The Weber number for the liquid and the gas, defined in Eq. (6.1) and Eq. (6.2), are respectively $\mathrm{We} \approx 8.7$ and $\mathrm{We_g} \approx 0.01$, confirming that the breakup of the liquid jet is purely driven by the Rayleigh breakup mechanism, since the criteria $\mathrm{We} > 4$ and $\mathrm{We_g} < 0.2$ holds.[23] The Ohnesorge number, defined in Eq. (6.3), $\mathrm{Oh} \approx 0.10$ is small, but finite, which implies that the viscosity of the liquid influences the motion of the fluid. The relevant time scale for the motion of the liquid is given by the capillary time $\tau_{\mathrm{c}} = \sqrt{\rho_\ell r^3/\gamma} \approx 10\,\mu$s. To resolve the droplet formation and the extremely fast pinch-off, a high-speed camera (Hyper-

vision HPV-1, Shimadzu Corp., Kyoto, Japan) was used which captures 102 consecutive images at a frame rate of 500,000 frames per second (fps) and 312 × 260 pixel spatial resolution, *cf.* Fig. 6.2(b). To minimize motion blur the exposure time of the camera was set to 1 μs. The camera was mounted to a microscope (BX-FM, Olympus Nederland bv, Zoeterwoude, The Netherlands) with a 50× objective lens (SLMPlan N 50×/0.35, Olympus). The system was operated in bright-field mode using a high-intensity continuous light source (LS-M352A, Sumita Optical Glass Europe GmbH, Germany) and fiber illumination.

6.3.2 Diminutive microjets (1 μm)

Diminutive liquid microjets were studied by mounting a nozzle chip that consisted of a row of 49 identical orifices of a radius of $r = 1.25\,\mu$m separated from each other by 25 μm. The nozzle chip was fed from a single liquid supply. The overall length of the jets showed no significant variation in the breakup length (< 5%). A 0.9% saline solution (with $\rho_\ell = 1003\,\mathrm{kg/m^3}$, $\eta = 1\,\mathrm{mPa{\cdot}s}$, and $\gamma = 72\,\mathrm{mN/m}$) was discharged at a constant liquid flow rate of 0.50 ml/min from the nozzle chip resulting in the formation of 49 parallel microjets of approximately 1.25 μm in radius (neglecting the *vena contracta* effect). The jet velocity is estimated by $v_{\mathrm{jet}} = Q/(nA) = 35\,\mathrm{m/s}$, with $n = 49$ the number of jets, and $A = \pi r^2$ the cross-sectional area of a single orifice. The Reynolds number Re = 44; the Weber number for the liquid We = 21, and for the gas $\mathrm{We_g} = 0.03$; the Ohnesorge number Oh = 0.10. The capillary time is $\tau_\mathrm{c} = 165\,\mathrm{ns}$. The extremely fast dynamics involved in the breakup of these diminutive jets were captured with the ultra high-speed Brandaris 128 camera[40] at a framerate of 13.76 Mfps, corresponding to a temporal resolution of 73 ns. The microscopic system used was the same as described above. A high-intensity flash lamp coupled into a liquid lightguide was used that produces a single flash with a pulse duration sufficiently long to expose all 128 image frames of the high-speed recording (≈ 10 μs).

6.4 Results

6.4.1 Results for microjets

In Fig. 6.3 we show a time series of the formation of a droplet captured using ultra high-speed imaging at 500 kfps (a) and we show the accompa-

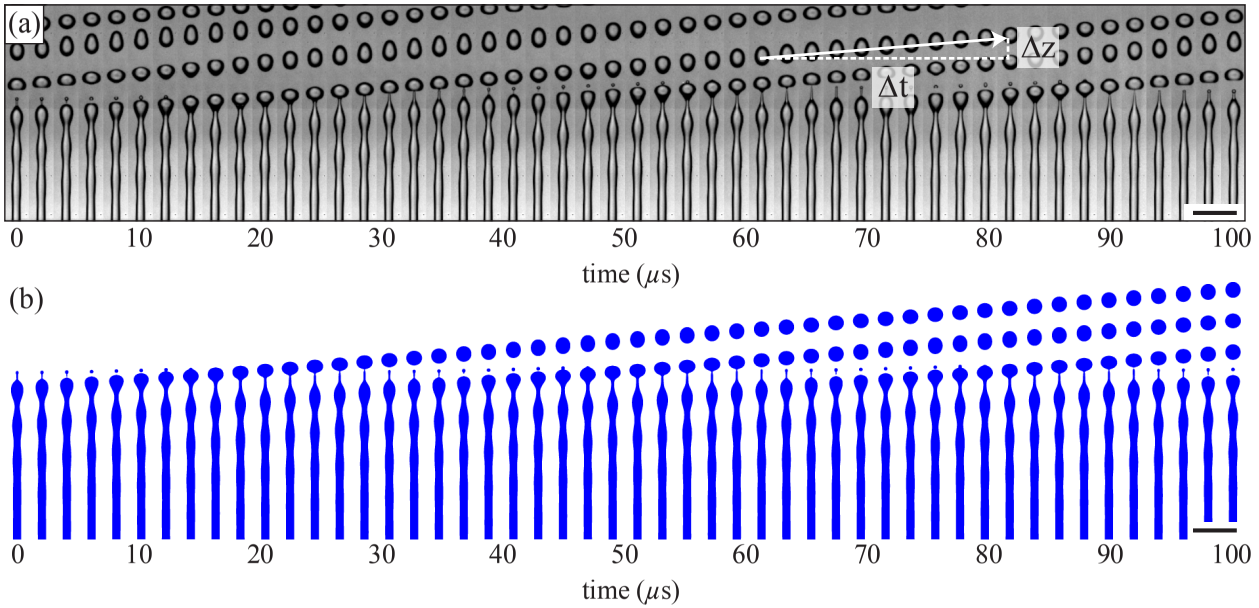

Figure 6.3: Comparison between the time series of the high-speed imaging results (a) and those obtained from the lubrication approximation calculation (b), indicating that droplet formation is predicted in good agreement with the experimental results. The droplet velocity is calculated from the displacement of the droplet's center of mass between two consecutive images. The scale bar in both panels correspond to 200 μm.

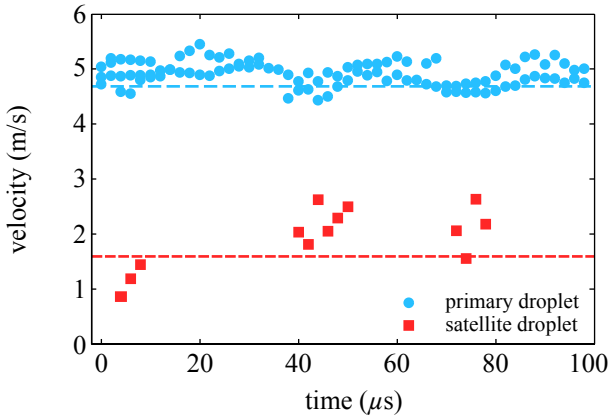

Figure 6.4: Experimental droplet velocity of the primary droplet (blue online) and the satellite droplet (red online) as a function of the time. The dashed line is the velocity predicted by the lubrication approximation model.

nying prediction based on the lubrication approximation model (b). The lubrication approximation model calculation is based on the experimental values for the radius of the jet $r = 18.5\,\mu$m, the jet velocity $v_{\text{jet}} = 5.4\,$m/s, and the liquid properties only. We observe two different types of droplets—the primary droplet, with a size almost twice the diameter of the jet, and a small satellite droplet. The satellite droplet is formed from the breakup of the thin thread between the jet and the primary droplet. In Fig. 6.3 it is demonstrated that the lubrication model accurately predicts both the formation of the primary droplet and its satellite droplet.

We obtain the velocity of the droplets from the displacement of the droplet's center of mass between two frames. Eight droplets are traced throughout the recording, resulting in a total of 116 velocity measurements, which are shown in Fig. 6.4. The predicted velocities for the primary droplet and the satellite droplets of respectively $4.68 \pm 0.01\,$m/s and $1.6 \pm 0.3\,$m/s, nicely agree with the experimental findings of $4.9 \pm 0.2\,$m/s and $1.9 \pm 0.6\,$m/s. In Fig. 6.4 it is also displayed that the velocity of the primary droplet shows a minimum (at time $6\,\mu$s, $40\,\mu$s, and $70\,\mu$s) that is correlated with the existence of the satellite droplet. This periodicity in the primary droplet velocity is due to an inertia effect as a consequence of the pinch-off.

The primary droplet travels at a speed that is smaller than the imposed liquid velocity $v_{\text{d}} < v_{\text{jet}}$, which is caused by the loss of kinetic energy due to surface oscillations after droplet pinch-off. The reason for the deceleration

Figure 6.5: Direct comparison between experimental results and the lubrication approximation model in both space and time. High-speed imaging at 500,000 fps shows the breakup of a 18.5 μm radius jet into a primary droplet and a small satellite droplet. A 40% glycerol-saline solution is supplied at 0.35 ml/min, equivalent to a jetting velocity of 5.4 m/s. The lubrication calculation (blue online) is synchronized to the location of droplet pinch-off in the experiment at $t = 0\,\mu$s. No fitting parameters were used. Satellite droplet merging with the primary droplet was not included in the model. The scale bar in the lower right corner denotes 100 μm.

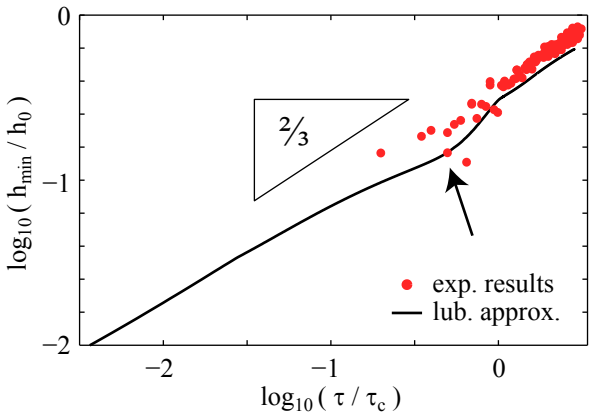

Figure 6.6: The logarithm of the normalized minimum radius of the neck $h_{\min}/h_0$ as a function of the logarithm of the time remaining until droplet pinch-off $\tau = t_c - t$, normalized by the capillary time τ_c, scales with a characteristic 2/3 scaling exponent.

of the satellite droplet with respect to the mean jet velocity can be understood from Fig. 6.5. In this figure we make a detailed comparison between the experimentally measured shape of the jet and the prediction obtained from the lubrication approximation model. The moment of primary droplet pinch-off defines time $t = 0\,\mu$s in the top-left panel. The axial-coordinate of the pinch-off location in the high-speed imaging recording is aligned with the one in the model calculation (in the first frame only). The satellite droplet pinches off from the primary droplet (at $t \approx 0\,\mu$s) before it pinches off from the jet (at $t \approx 4\,\mu$s), resulting in a deceleration of the satellite droplet.[29]

In Fig. 6.6 we plot the evolution of the minimum radius of the neck $h_{\min}$ during collapse, until breakup. When the viscosity of the liquid is neglected, the collapse of the 'neck' can be described by a radially collapsing cylinder. From a balance between inertia and surface tension forces it follows that the minimum radius of the neck $h_{\min} \propto (\tau/\tau_c)^{2/3}$, with a characteristic 2/3 exponent.[41] The experimental data fall on a single power-law curve with an exponent equal to 2/3. The evolution of the minimum radius of the neck during pinch-off predicted by the lubrication approximation shows a deviation from the 2/3 slope line (indicated by the arrow in Fig. 6.6), which can be attributed to the formation of the satellite droplet, as described in the work by Brenner *et al.*[18] and Notz *et al.*[42] This is illustrated in Fig. 6.7 where three moments during droplet pinch-off are shown. In (i)

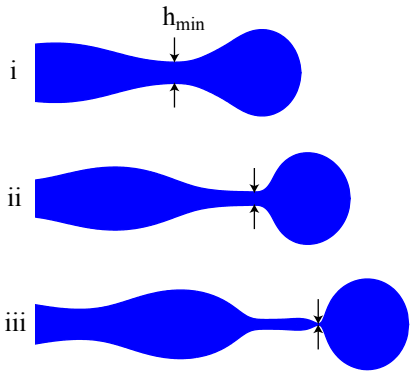

Figure 6.7: The shape of the neck for three successive moments approaching droplet pinch-off.

and (ii) the thin liquid thread shows an elongation, which is followed up by a thickening (iii) and the formation of a satellite droplet. This affects the breakup dynamics and causes a (transient) deviation from the asymptotic 2/3 behavior.

6.4.2 Results for diminutive microjets

We now consider the results obtained from the ultra high-speed imaging recordings for the breakup of diminutive jets of 1 μm in radius. Fig. 6.8 shows a time series obtained from the 128 image frames captured with the Brandaris 128 camera[40] (a) and the accompanying lubrication approximation calculation (b). The experimental results show the formation of microdroplets at a temporal resolution of 73 ns and a spatial resolution of 0.22 μm/pixel. Note that the total time displayed is less than 10 μs—within this time 30 droplets and 30 satellite droplets are formed. The ultra high-speed time series shows the formation of the primary droplets and even of the existence of satellite droplets. The primary droplet size is determined by measuring the cross-sectional area of the droplet using digital image analysis—its equivalent radius is 2.5 $\pm$ 0.2 μm, which nicely agrees with the predicted droplet size by the lubrication model of 2.4 μm. The area of the satellite droplet is too small to measure it accurately. From the lubrication approximation calculation we can learn that the size of the satellite droplet is 0.6 μm (equivalent to a droplet volume of 1 fl).

The same set of image frames is shown in greater detail in Fig. 6.9. It is observed that droplet formation from the breakup of a 1 μm liquid

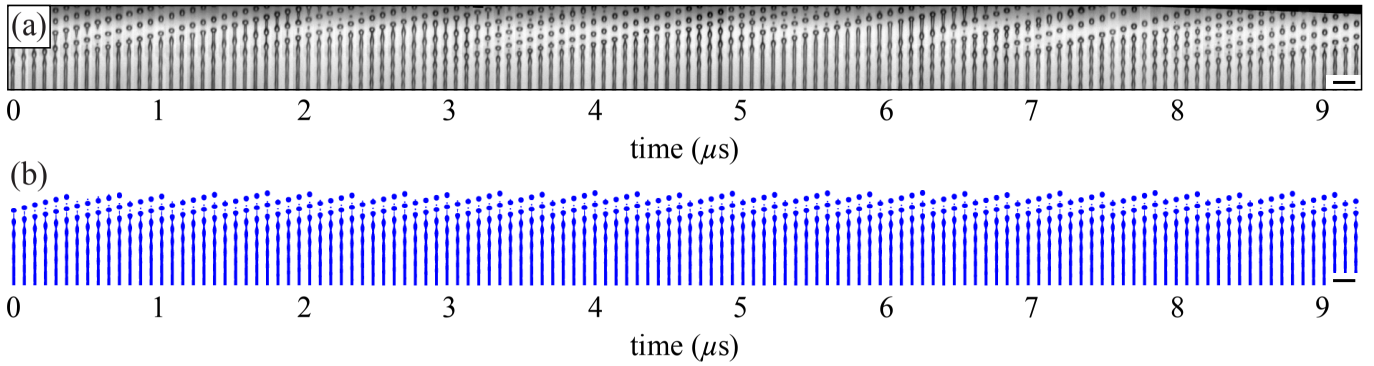

Figure 6.8: Time series of the ultra high-speed imaging results recorded at 13.76 Mfps (a) and the accompanying prediction from the lubrication approximation model (b) showing the breakup of a 1.25 μm liquid jet into droplets. The period in droplet formation is approximately 300 ns. The interframe time is 73 ns. The high-speed image frames are displayed in greater detail in Fig. 6.9. The scale bar in the lower right corner of both panels denote 20 μm.

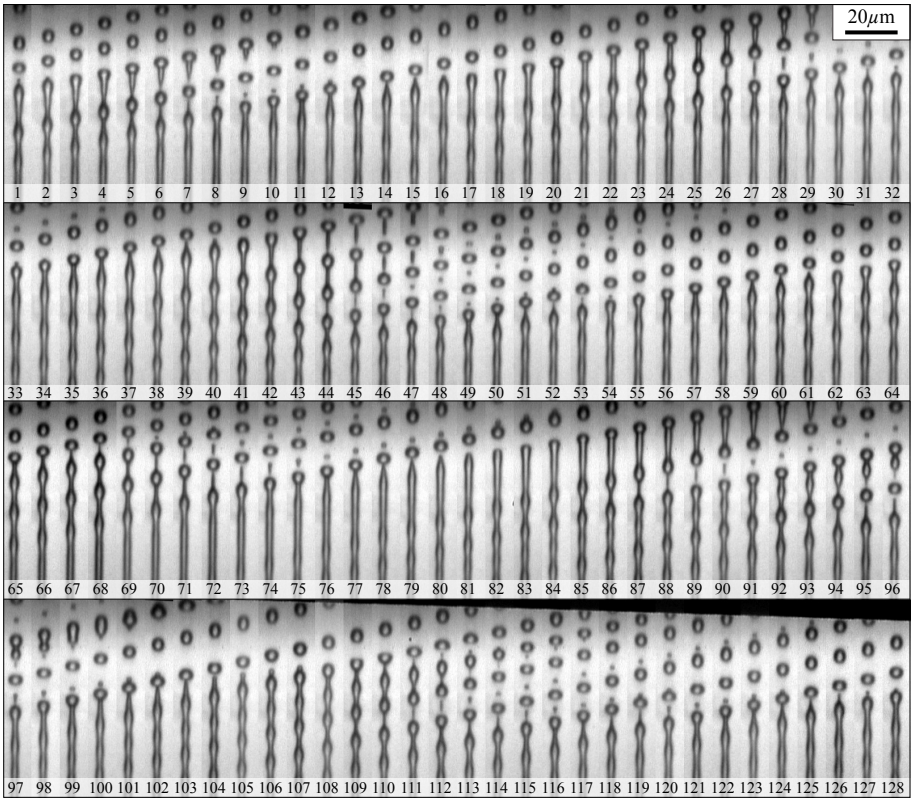

Figure 6.9: A sequence of 128 image frames recorded at 13.76 Mfps showing the breakup of a 1.25 μm radius liquid jet into microdroplets. The liquid used was a 0.9% saline solution, with density $\rho = 1003\,\mathrm{kg/m^3}$, surface tension $\gamma = 72\,\mathrm{mN/m}$, and viscosity $\eta = 1\,\mathrm{mPa{\cdot}s}$. The frame number is indicated in the bottom of each frame. The interframe time is 73 ns.

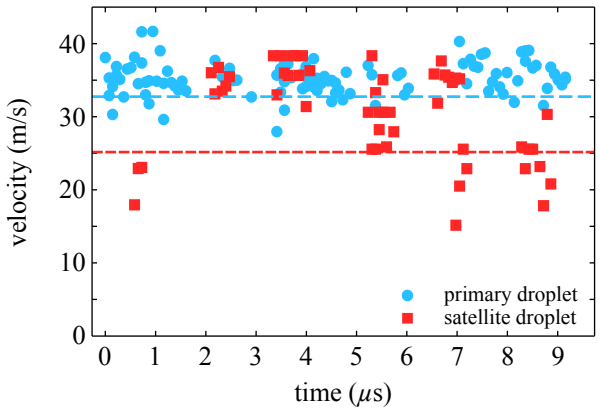

Figure 6.10: Experimental droplet velocity obtained from the 13.76 Mfps recording of the primary droplet (blue online) and the satellite droplet (red online) as a function of time. The velocity of the primary droplet $v_{\mathrm{prim}} = 35 \pm 2\,\mathrm{m/s}$; the velocity of the satellite droplet $v_{\mathrm{sat}} = 30 \pm 10\,\mathrm{m/s}$ shows a wide velocity distribution. The predicted velocity by the lubrication approximation model for the primary droplet is $32.8 \pm 0.2\,\mathrm{m/s}$ and for the satellite droplet $25.2 \pm 0.1\,\mathrm{m/s}$ (dashed lines).

microjet shows more irregularities in comparison to droplet formation from a 18.5 μm jet (*cf.* Fig. 6.3(a)). Two possible explanations can be given for this phenomena. First, it can be a nozzle shape effect. In case of the 18.5 μm jet the rectangular nozzle shape and oscillations at the nozzle exit may advance the breakup process by stimulating the jet breakup through non-linear interaction. Stimulated jet breakup results in a more reproducible droplet formation. In contrast, the shape of the nozzle for the for the case of the 1 μm jet is circular, and, consequently, no oscillations are present. Knowledge of the influence of the nozzle shape on the droplet formation process requires further investigation. Second, it can be a thermal noise effect. The 1 μm liquid jet may experience a relatively high contribution of thermal noise that would promote a more irregular droplet formation. The more irregular droplet formation process is best witnessed by the variation in droplet and satellite droplet spacing and the diversity in droplet pinch-off location in Fig. 6.9.

This is also expressed in the droplet velocity distribution. In Fig. 6.10 the droplet and satellite droplet velocity as a function of the time is shown. The velocity of the droplets is obtained by tracking the center of mass of each droplet throughout the high-speed imaging recording using digital image processing. The experimental velocity of the primary droplet and

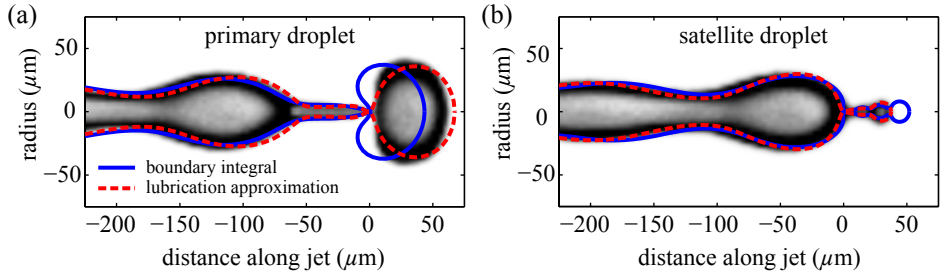

Figure 6.11: Comparison between the inviscid, axisymmetric boundary-integral simulation and the one-dimensional lubrication approximation including viscosity. Here, the jet radius is 18.5 μm and the jet velocity is 5.4 m/s. A 40% glycerol-saline solution was used, with density $\rho_\ell = 1098\,\mathrm{kg/m^3}$, viscosity $\eta = 3.65\,\mathrm{mPa{\cdot}s}$, and surface tension $\gamma = 67.9\,\mathrm{mN/m}$. While the boundary-integral approach can model the overturning of the pinching drop (a), it does not accurately capture the formation of satellites (b).

satellite droplet are $35 \pm 2\,\mathrm{m/s}$ and $30 \pm 10\,\mathrm{m/s}$. The velocity of the satellite droplet shows a wide variation. The velocity predicted by the lubrication approximation model for the primary droplet is 33 m/s.

6.5 Boundary integral

The one-dimensional nature of the lubrication approximation model implies that it cannot describe the concave curvature, or 'overturning', of the droplet at pinch-off. Droplet overturning typically occurs for low-viscosity liquids, but it is also observed experimentally for more viscous liquids.[43] The shape of an inviscid liquid droplet at pinch-off exhibits droplet overhang with a unique characteristic angle of 112.8°.[44] In Wilkes *et al.*[31] a numerical study is presented on the influence of liquid viscosity on the angle of droplet overhang. Droplet overturning is suppressed when the liquid viscosity is sufficiently large such that viscous shear stress is efficiently dissipated into the liquid. Droplet overturning is suppressed for Oh typically around 0.01 and 0.1. In this work we are close to the critical viscosity (Oh = 0.1 in both studies) and overturning could occur. However, from the high-speed (shadow) images in Fig. 6.5 and Fig. 6.9 it is not clear whether the droplet shows some overhang. The amount of droplet overhang, if exists, is of the same order of the pixel size and can not be quantified.

Here we make a comparison between an axisymmetric boundary integral (BI) calculation, which can describe droplet overhang, and the one-dimensional lubrication approximation model (which includes viscosity, in

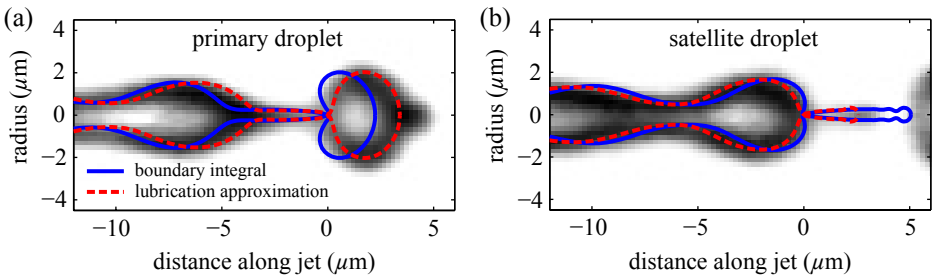

Figure 6.12: Comparison between the boundary-integral simulation and the one-dimensional lubrication approximation for the breakup of a 1.25 μm jet. The jet velocity 35 m/s. A 0.9% normal saline solution was used, with density $\rho_\ell = 1003\,\mathrm{kg/m^3}$, viscosity $\eta = 1\,\mathrm{mPa{\cdot}s}$, and surface tension $\gamma = 72\,\mathrm{mN/m}$.

contrast to BI). In Fig. 6.11 and Fig. 6.12 we show boundary-integral numerical simulations for the same cases as studied above experimentally and within the lubrication approximation. The drawback is that BI methods are only applicable in the inviscid limit (Oh = 0) due to the potential flow description. Details of the implementation of the BI scheme are given in Gekle *et al.*[45]

Fig. 6.11 and Fig. 6.12 shows a comparison of droplet pinch-off obtained from the BI simulation and the lubrication approximation. As can be seen in Fig. 6.11(a), the BI simulation indeed displays the overturning of the main droplet just before pinch-off, in contrast to the one-dimensional lubrication theory. However, the size of the predicted overturning is clearly inconsistent with the experimental observations. The experimental results for the droplet is in between the BI and lubrication predictions. In addition, Fig. 6.11(b) reveals some deviations in the shape and size of the satellite droplet. We attribute this to the missing viscosity in the BI method as satellite formation is closely connected to viscous effects.

6.6 Discussion & conclusion

In spite of its limitations the one-dimensional lubrication approximation model predicts the formation of the microdroplets and satellite droplets and their sizes with great accuracy. The advantage of a one-dimensional approach is the limited time required to perform a complete calculation. This makes it possible to perform a parameter study. In Fig. 6.13 a phase diagram is shown, indicating the effect of the jetting velocity and viscosity

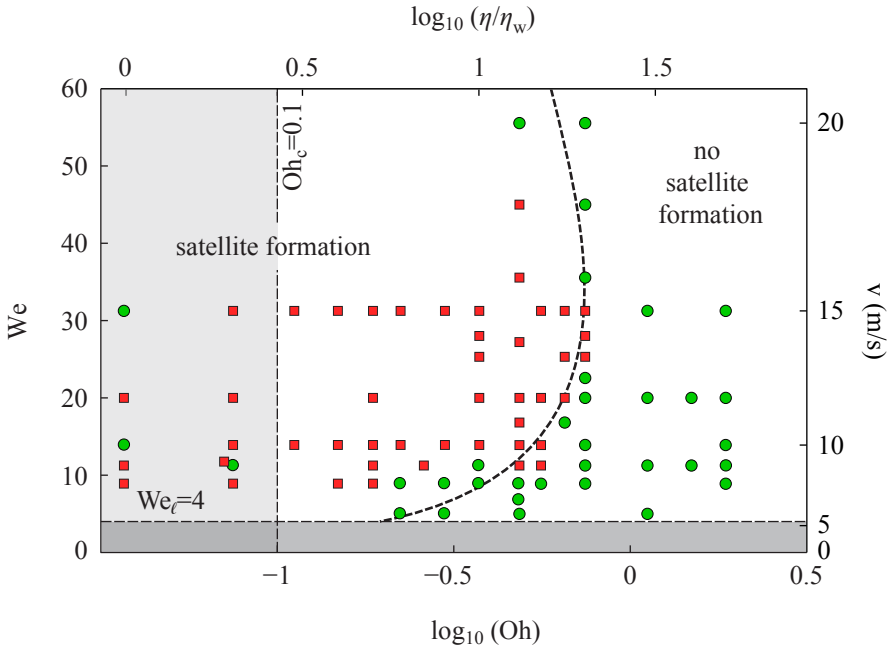

Figure 6.13: Phase diagram of satellite droplet formation regimes for various viscosity liquids and jetting velocities. Squares denote cases where our lubrication approximation calculation predicts satellite droplets, circles denote cases without satellite droplets. On the horizontal axis the logarithm of the Ohnesorge number $\log \mathrm{Oh} = \eta/\sqrt{\rho r \gamma}$ (at the bottom) and the logarithm of the relative viscosity $\log \eta/\eta_\mathrm{w}$ (at the top), with $\eta_\mathrm{w} = 1\,\mathrm{mPa{\cdot}s}$ the viscosity of water at 20°C, are shown. The vertical axis shows the Weber number $\mathrm{We} = \rho v^2 r/\gamma$ (at the left) and the jetting velocity v (at the right). The lower critical velocity for jet formation is indicated by the horizontal dashed line. Droplet 'overhang' is suppressed in the region right of the vertical dashed line, with $\mathrm{Oh_c} = 0.1$. The curved dashed line is a guide to the eye. Right of this line the formation of satellite droplets is suppressed. The radius of the jet, liquid density, and surface tension are kept constant ($r = 10\,\mu\mathrm{m}$, $\rho_\ell = 1000\,\mathrm{kg/m^3}$, and $\gamma = 72\,\mathrm{mN/m}$).

on the formation of satellite droplets. The jetting velocity is expressed in the Weber number, the viscosity in the Ohnsesorge number. A clear region is found for which the formation of satellite droplets is suppressed. In this regime the driving frequency and the amplitude of the modulation are kept constant. It is well known that the amplitude and the wavelength-to-diameter ratio affect the formation and behavior of satellite droplets.[29] To get a complete picture the phase diagram should be extended so that it includes these parameters.

In conclusion, the extremely fast droplet formation process from the spontaneous breakup of a liquid microjet is resolved at a high spatial and temporal resolution using ultra high-speed imaging up to 14 Mfps. A direct comparison is made between the experimental results and those obtained from a one-dimensional (1D) model based on the lubrication approximation. A 1D model is limited by the fact that it can not describe the complex shape of the droplet at the final moment of pinch-off, *e.g.* droplet 'overhang', which typically occurs for low-viscosity liquids. We made a comparison between the lubrication approximation and a boundary integral calculation. The lubrication approximation predicts the shape of the droplet at pinch-off to be closer to its most favorable state—a perfect sphere—hence it is less subject to shape oscillations. Inspite of this discrepancy it is shown that the lubrication approximation can predict the size of the droplets, its velocity, and the formation of satellite droplets, with great accuracy. The 1D origin of the lubrication approximation makes it computationally less demanding in comparison to two-dimensional models, which makes it highly interesting to be used to investigate parameter space in droplet formation, also for diminutive Rayleigh jets.

References

[1] T. Thorsen, R. W. Roberts, F. H. Arnold, and S. R. Quake, "Dynamic pattern formation in a vesicle-generating microfluidic device," *Phys. Rev. Lett.* **86**, 4163–4166 (2001).

[2] V. van Steijn, C. R. Kleijn, and M. T. Kreutzer, "Predictive model for the size of bubbles and droplets created in microfluidic T-junctions," *Lab Chip* **10**, 2513–2518 (2010).

[3] E. Castro-Hernández, V. Gundabala, A. Fernández-Nieves, and J. M. Gordillo, "Scaling the drop size in coflow experiments," *New J. Phys.* **11**, 075021 (2009).

[4] S. L. Anna, N. Bontoux, and H. A. Stone, "Formation of dispersions using flow focusing in microchannels," *Appl. Phys. Lett.* **82**, 364–366 (2003).

[5] A. S. Utada, E. Lorenceau, D. R. Link, P. D. Kaplan, H. A. Stone, and D. A. Weitz, "Monodisperse double emulsions generated from a microcapillary device," *Science* **308**, 537–541 (2005).

[6] A. M. Gañán-Calvo, R. González-Prieto, P. Riesco-Chueca, M. A. Herrada, and M. Flores-Mosquera, "Focusing capillary jets close to the continuum limit," *Nature Phys.* **3**, 737–742 (2007).

[7] D. B. Bogy, "Drop formation in a circular liquid jet," *Annu. Rev. Fluid Mech.* **11**, 207–228 (1979).

[8] D. M. Mitchell, M. A. Solomon, S. E. J. Tolfree, M. Short, and S. G. Spiro, "Effect of particle size of bronchodilator aerosols on lung distribution and pulmonary function in patients with chronic asthma," *Thorax* **42**, 457–461 (1987).

[9] W. D. Bennett, J. S. Brown, K. L. Zeman, S.-C. Hu, G. Scheuch, and K. Sommerer, "Targeting delivery of aerosols to different lung regions," *J. Aerosol Med.* **15**, 179–188 (2002).

[10] A. M. Gañán-Calvo, "Generation of steady liquid microthreads and micron-sized monodisperse sprays in gas streams," *Phys. Rev. Lett.* **80**, 285–288 (1998).

[11] O. A. Basaran, "Small-scale free surface flows with breakup: Drop formation and emerging applications," *AIChE J.* **48**, 1842–1848 (2002).

[12] O. A. Basaran and R. Suryo, "Fluid dynamics: The invisible jet," *Nature Phys.* **3**, 679–680 (2007).

[13] H. P. Le, "Progress and trends in ink-jet printing technology," *J. Imaging Sci. Technol.* **42**, 49–62 (1998).

[14] Q. Xu and O. A. Basaran, "Computational analysis of drop-on-demand drop formation," *Phys. Fluids* **19**, 102111 (2007).

[15] H. Wijshoff, "The dynamics of the piezo inkjet printhead operation," *Phys. Rep.* **491**, 77–177 (2010).

[16] K. Tang and A. Gomez, "Generation by electrospray of monodisperse water droplets for targeted drug delivery by inhalation," *J. Aerosol Sci.* **25**, 1237–1249 (1994).

[17] D.-R. Chen, D. Y. H. Pui, and S. L. Kaufman, "Electrospraying of conducting liquids for monodisperse aerosol generation in the 4 nm to 1.8 m diameter range," *J. Aerosol Sci.* **26**, 963–977 (1995).

[18] M. P. Brenner, J. Eggers, K. Joseph, S. R. Nagel, and X. D. Shi, "Breakdown of scaling in droplet fission at high reynolds number," *Phys. Fluids* **9**, 1573–1590 (1997).

[19] B. Ambravaneswaran, S. D. Phillips, and O. A. Basaran, "Theoretical analysis of a dripping faucet," *Phys. Rev. Lett.* **85**, 5332–5335 (2000).

[20] B. Ambravaneswaran, H. J. Subramani, S. D. Phillips, and O. A. Basaran, "Dripping-jetting transitions in a dripping faucet," *Phys. Rev. Lett.* **93**, 034501 (2004).

[21] P. Coullet, L. Mahadevan, and C. S. Riera, "Hydrodynamical models for the chaotic dripping faucet," *J. Fluid Mech.* **526**, 1–17 (2005).

[22] H. H. Chen and M. P. Brenner, "The optimal faucet," *Phys. Rev. Lett.* **92**, 166106 (2004).

[23] S. P. Lin and R. D. Reitz, "Drop and spray formation from a liquid jet," *Annu. Rev. Fluid Mech.* **30**, 85–105 (1998).

[24] J. A. F. Plateau, *Statique expérimentale et théorique des liquides soumis aux seules forces moléculaires* (Gauthier-Villard, Paris, 1873).

[25] Lord Rayleigh, "On the capillary phenomena of jets," *Proc. R. Soc. London* **29**, 71–97 (1879).

[26] A. H. Lefebvre, *Atomization and Sprays* (Hemisphere Pub. Corp., New York, 1989).

[27] A. Kalaaji, B. Lopez, P. Attané, and A. Soucemarianadin, "Breakup length of forced liquid jets," *Phys. Fluids* **15**, 2469–2479 (2003).

[28] H. González and F. J. García, "The measurement of growth rates in capillary jets," *J. Fluid Mech.* **619**, 179–212 (2009).

[29] W. T. Pimbley and H. C. Lee, "Satellite droplet formation in a liquid jet," *IBM J. Res. Develop.* **21**, 385–388 (1977).

[30] J. Eggers and E. Villermaux, "Physics of liquid jets," *Rep. Prog. Phys.* **71**, 036601 (2008).

[31] E. Wilkes, S. D. Phillips, and O. A. Basaran, "Computational and experimental analysis of dynamics of drop formation," *Phys. Fluids* **11**, 3577–3598 (1999).

[32] J. H. Hilbing and S. D. Heister, "Droplet size control in liquid jet breakup," *Phys. Fluids* **8**, 1574–1581 (1996).

[33] M. Moseler and U. Landman, "Formation, stability, and breakup of nanojets," *Science* **289**, 1165–1169 (2000).

[34] J. Eggers and T. F. Dupont, "Drop formation in a one-dimensional approximation of the Navier-Stokes equation," *J. Fluid Mech.* **262**, 205–221 (1994).

[35] X. D. Shi, M. P. Brenner, and S. R. Nagel, "A cascade of structure in a drop falling from a faucet," *Science* **265**, 219–222 (1994).

[36] B. Ambravaneswaran, E. D. Wilkes, and O. A. Basaran, "Drop formation from a capillary tube: Comparison of one-dimensional and two-dimensional analyses and occurrence of satellite drops," *Phys. Fluids* **14**, 2606–2621 (2002).

[37] O. E. Yildirim, Q. Xu, and O. A. Basaran, "Analysis of the drop weight method," *Phys. Fluids* **17**, 062107 (2005).

[38] E. P. Furlani and M. S. Hanchak, "Nonlinear analysis of the deformation and breakup of viscous microjets using the method of lines," *Int. J. Numer. Meth. Fluids*(2010), doi:\bibinfo{doi}{10.1002/fld.2205}.

[39] E. J. Gutmark and F. F. Grinstein, "Flow control with noncircular jets," *Annu. Rev. Fluid Mech.* **31**, 239–272 (1999).

[40] C. T. Chin, C. Lancée, J. Borsboom, F. Mastik, M. E. Frijlink, N. de Jong, M. Versluis, and D. Lohse, "Brandaris 128: A digital 25 million frames per second camera with 128 highly sensitive frames," *Rev. Sci. Instrum.* **74**, 5026–5034 (2003).

[41] D. Leppinen and J. R. Lister, "Capillary pinch-off in inviscid fluids," *Phys. Fluids* **15**, 568–578 (2003).

[42] P. K. Notz, A. U. Chen, and O. A. Basaran, "Satellite drops: Unexpected dynamics and change of scaling during pinch-off," *Phys. Fluids* **13**, 549–552 (2001).

[43] A. Chen, P. Notz, and O. A. Basaran, "Computational and experimental analysis of pinch-off and scaling," *Phys. Rev. Lett.* **88**, 174501 (2002).

[44] R. F. Day, E. J. Hinch, and J. R. Lister, "Self-similar capillary pinchoff of an inviscid fluid," *Phys. Rev. Lett.* **80**, 704–707 (1998).

[45] S. Gekle, J. M. Gordillo, D. van Der Meer, and D. Lohse, "High-speed jet formation after solid object impact," *Phys. Rev. Lett.* **102**, 034501 (2009).

Chapter 7 Conclusions & Outlook

In this thesis we studied the formation and pinch-off of microdroplets and microbubbles both experimentally using high-speed microscopic imaging and numerically within the lubrication approximation. Microdroplets were formed through the spontaneous breakup of a microscopically thin liquid jet, whereas microbubbles were produced in various types of planar microfluidic devices operated in different regimes.

In *Chapter 2* we studied the influence of the channel geometry on the microbubble pinch-off in flow-focusing devices. Various microfluidic devices were fabricated in PDMS with different channel widths and heights. The time evolution of the minimum radius of the gaseous neck was obtained experimentally using high-speed imaging. For elongated rectangular channels, where the channel height is much smaller than the channel width, we revealed two distinct regimes of the collapse, namely, a quasi two-dimensional lateral collapse followed by an extremely fast 3D pinch-off. During the initial stage of the collapse the minimum radius of the neck decreases linearly in time as $h_{\mathrm{m}} \propto \tau$. During this stage the gaseous thread is stable against perturbations of the interface due to its strong confinement by the channel's top and bottom surfaces.[1] Hence, the neck is 'squeezed' in the lateral direction only and proceeds through a series of equilibria[2] which makes bubble formation in this regime highly controllable. A transition to the next collapse regime sets in when the gaseous thread separates from the channel walls. As a result the gas-liquid interface becomes unstable against perturbations.[1] In this final stage an extremely fast radial collapse sets in that ultimately leads to microbubble pinch-off. It was experimentally found that the radius of the neck goes to zero as $h_{\mathrm{m}} \propto \tau^{\alpha}$, with power law scaling exponent $\alpha \approx 1/3$ suggesting that gas inertia is important.[3] Thus, the overall bubble breakup shows that elongated rectangular channels favors high monodispersity, whereas the highest frequency of bubble production is achieved in square geometries.

In *Chapter 3* we focused on the ultimate stage of microbubble pinch-off within a square cross-sectional flow-focusing channel using ultra high-speed imaging. We captured the complete bubble contour at high spatial and high temporal resolution such that the final moment of pinch-off could be approached to within 1 μs. The camera's wide field of view (200 μm $\times$ 175 μm at 1 Mfps) enabled us to measure the volume of the bubble and both the radial and axial length scales of the neck during the entire collapse process. It was found that the radius of the neck goes to zero as $h_{\mathrm{m}} \propto \tau^{\alpha}$, with $\alpha = 0.41 \pm 0.01$ spanning almost 2 decades. From the volumetric expansion of the bubble an estimate of the gas velocity through the neck was obtained. It was found that the gas velocity was too low for gas inertia, *i.e.* Bernoulli suction, to be the dominant effect. However, we showed that both the radial and axial length scales of the neck play important roles during the collapse. The axial length scale of the neck diminishes more rapidly than the radial length scale, and consequently, the neck becomes *less slender* approaching pinch-off. This behavior is in contrast to results previously reported by Bergmann *et al.*[4], Thoroddsen *et al.*[5], and Gekle *et al.*[6], among others, where the neck becomes *more slender*. This 3D character suggest that the liquid flows spherically inward towards the collapsing neck. We describe this collapse using the Rayleigh-Plesset equation for spherical bubble collapse[7] and recover a 2/5 power law exponent which agrees surprisingly well with our experimental findings. Thus, the final moment of microbubble pinch-off in a flow-focusing system is purely liquid inertia driven.

In *Chapter 4* we studied monodisperse microbubble formation in a co-flow device operated in a new regime. This new regime allowed us to produce microbubbles in a controlled and reproducible way by employing a strong pressure gradient in the entrance region of the microfluidic channel. The monodisperse size of the bubbles could be varied by adjusting the gas and liquid flow rates such that microbubbles with a radius $r_{\mathrm{b}} < 5\,\mu$m could be precision produced. Note that r_{b} is considerably smaller than the channel width, which was tens of microns wide. Furthermore we have theoretically accounted for this new regime and derived the correct scaling laws for the microbubble size as function of the control parameters. This new regime offers a robust method to accurately produce monodisperse microbubbles at a high production rate which avoids clogging problems within the microfluidic system. This is an important step forwards for industrial applications such as ultrasound contrast agent microbubble formation for

medical diagnostic imaging.

In *Chapter 5* a prediction of the size of droplets and bubbles produced in the 'jetting' regime in a co-flow geometry was derived in detail. A description of the inner jet's radius based on the system's control parameters was obtained for two distinct cases. In the first case we consider droplet formation for two co-flowing viscous fluids, where the inner and outer velocity profiles were assumed to be fully developed Poiseuille flows[8] and the radius of the inner jet scales as $r_j \propto (Q_i/Q_o)^{\alpha}$. A transition in the scaling exponent α between 1/2 and 1/4 occurs for decreasing viscosity ratio. Previously a scaling exponent of 1/4 was observed experimentally in *Chapter 4*. In the second case for bubble formation, the viscosity of the inner phase was neglected and the flow was assumed to exhibited a flat velocity profile. The radius of the inner jet was found by minimization of the energy dissipation at the interface. It was shown that for small gas fractions $Q_i \ll Q_o$ the influence of the inner flow conditions on the jet radius was marginal. Further investigation using a Rayleigh-Plateau type of stability analysis is required to predict the exact relation between the radius of the inner jet and the actual droplet (and bubble) size within confined geometries.

In *Chapter 6* the extremely fast droplet formation process from the natural breakup of a microscopically thin liquid jet into droplets was investigated. This was done experimentally using ultra high-speed imaging and numerically by means of a 1D model based on the lubrication approximation.[9,10] A liquid emanating from a nozzle at sufficiently large velocity forms a jet that is inherently unstable and spontaneously breaks up into droplets to minimize its surface energy. In the analyzed low Reynolds number regime the breakup is driven by surface tension forces only. Instabilities govern, and therefore strongly influence, the controllability and reproducibility of the droplet formation process. Here, ultra high-speed imaging at 14 Mfps was used to visualize the breakup of a 1 μm liquid jet. A direct comparison between the experimental results and those obtained from the lubrication approximation showed that the model could predict the size of the droplets, its velocity, and the formation of satellite droplets, with great accuracy. This direct comparison confirmed a universal scaling law also for diminutive Rayleigh jets.

References

[1] P. Guillot, A. Colin, A. S. Utada, and A. Ajdari, "Stability of a jet in confined pressure-driven biphasic flows at low reynolds numbers," *Phys. Rev. Lett.* **99**, 104502 (2007).

[2] P. Garstecki, H. A. Stone, and G. M. Whitesides, "Mechanism for flow-rate controlled breakup in confined geometries: A route to monodisperse emulsions," *Phys. Rev. Lett.* **94**, 164501 (2005).

[3] J. M. Gordillo, "Axisymmetric bubble collapse in a quiescent liquid pool. I. theory and numerical simulations," *Phys. Fluids* **20**, 112103 (2008).

[4] R. Bergmann, D. van der Meer, M. Stijnman, M. Sandtke, A. Prosperetti, and D. Lohse, "Giant bubble pinch-off," *Phys. Rev. Lett.* **96**, 154505 (2006).

[5] S. T. Thoroddsen, T. G. Etoh, and K. Takehara, "Experiments on bubble pinch-off," *Phys. Fluids* **19**, 042101 (2007).

[6] S. Gekle, I. R. Peters, J. M. Gordillo, D. van Der Meer, and D. Lohse, "Supersonic air flow due to solid-liquid impact," *Phys. Rev. Lett.* **104**, 024501 (2010).

[7] H. N. Oğuz and A. Prosperetti, "Dynamics of bubble-growth and detachment from a needle," *J. Fluid Mech.* **257**, 111–145 (1993).

[8] A. S. Utada, E. Lorenceau, D. R. Link, P. D. Kaplan, H. A. Stone, and D. A. Weitz, "Monodisperse double emulsions generated from a microcapillary device," *Science* **308**, 537–541 (2005).

[9] J. Eggers and T. F. Dupont, "Drop formation in a one-dimensional approximation of the Navier-Stokes equation," *J. Fluid Mech.* **262**, 205–221 (1994).

[10] X. D. Shi, M. P. Brenner, and S. R. Nagel, "A cascade of structure in a drop falling from a faucet," *Science* **265**, 219–222 (1994).

Summary

The formation of microscopically small droplets and bubbles with an accurately controlled and narrow size distribution is crucial in a wide variety of products and applications. For example, in medical applications such as diagnostic ultrasound imaging, targeted drug delivery, and drug inhalation therapy, but also in inkjet printing, cosmetics and in the modern food industry. The typical size of the droplets and bubbles investigated in this thesis are much smaller than the thickness of a human hair (100 μm) and the time scale of the formation process is of the order of several microseconds or less. Approaching the singularity that arises when the droplet or bubble detaches from its source, the time and length scales become ever smaller. Hence, to capture the final moment of pinch-off experimentally, ultra high-speed microscopic imaging is required. The research presented in this thesis discusses various aspects of droplet and bubble formation in different microfluidic systems both experimentally and numerically.

In *Chapter 1* a general introduction to the research area of droplet and bubble formation both historically and more recently using microfluidic techniques is presented.

In *Chapter 2* the role of the channel's dimensions on the microbubble pinch-off in a rectangular cross-sectional flow-focusing channel is investigated. It is experimentally shown that the channel aspect ratio AR $= H/W$, with H and W the height and width of the channel respectively, strongly influence the dynamics of the bubble pinch-off. For a low aspect ratio channel, where $H \ll W$, two distinct collapse regimes exist, as is shown in Fig. 2.3 on page 13. In the initial stage the strongly confined gaseous neck is squeezed by the outer liquid in the lateral direction only. When the size of the neck becomes smaller than the height of the channel an extremely fast radial collapse sets in that ultimately leads to bubble pinch-off. In this final stage it is experimentally found that the pinch-off yields a scaling $r_{\mathrm{m}} \propto \tau^{1/3}$ between the neck radius r_{m} and the time τ until

pinch-off. From stability analysis it is found that the confined quasi two-dimensional neck is always stable against surface perturbations, whereas the unconfined three-dimensional collapsing neck is always unstable giving rise to more irregularities. Therefore, high monodisperse microbubble formation is achieved in low aspect ratio channel geometries ($H \ll W$), whereas square geometries ($H = W$) favor high bubble production rate.

The 1/3 power law scaling that was measured previously during the final stage of bubble pinch-off can possibly be explained due to an accelerated gas flow through the neck. In *Chapter 3* this final stage is investigated in more detail using ultra high-speed imaging at 1 million frames per second (Mfps) enabling the singularity to be approached to within 1 μs. The camera's wide field of view allows to capture the complete contour of the expanding bubble including both the radial and axial variation of the neck. The gas velocity through the neck is calculated from the bubble's volumetric expansion over time divided by the cross-sectional area of the neck. It is found that the initially low velocity gas flow reverses direction and gradually accelerates until it reaches its maximum velocity ($u \approx 23\,\mathrm{m/s}$) at bubble pinch-off. Despite this strong acceleration, gas inertia only plays a marginal role during the entire collapse process. However, it is found that both the radial and axial length scale of the neck are important. In Fig. 3.5 on page 30 it is shown that the axial length scale of the neck goes to zero more rapidly than the radial length scale, which implies that the neck becomes less slender approaching pinch-off. This gives the collapse a three-dimensional character in which the liquid flows spherically inward towards the neck via a purely liquid inertia driven collapse. A description using the Rayleigh-Plesset equation for spherical bubble collapse reveals that the radius of the neck must scale as $r_\mathrm{m} \propto \tau^{2/5}$ which agrees surprisingly well with the experimentally measured scaling exponent of 0.41 ± 0.01.

In *Chapter 4* a microfluidic co-flow device is employed in which microbubbles with diameters substantially smaller than the channel width are formed, *i.e.* $d_\mathrm{b}/W < 0.1$. The device is operated in a new regime in which a strong pressure gradient is responsible for the formation of a gas ligament that forms bubbles at its tip. The precisely controlled size of these bubbles is predicted by a scaling theory, in which $d_\mathrm{b}/W \propto (\mu_\mathrm{g}/\mu_\mathrm{l})^{1/12}\,(Q_\mathrm{g}/Q_\mathrm{l})^{5/12}$, where μ_g and μ_l indicate, respectively, the gas and liquid viscosities and Q_g and Q_l are the gas and liquid flow rates. Fig. 4.2 on page 45 shows microbubble formation for different gas and liquid flow-rate ratios. Under the right conditions monodisperse bubbles are formed with a size smaller

than 5 μm and a production rate exceeding 10^5 Hz. This is an important step forwards for industrial applications where high throughput and low chance of system failure due to clogging of the microchannels is essential.

In *Chapter 5* a theoretical description of the size of the bubbles formed through the breakup of a gaseous jet that is surrounded by a co-flowing liquid is presented. The size of the bubbles is governed by the radius of the inner gas jet and the frequency in which the jet breaks up into bubbles, thus is purely based on the system's control parameters. The size of the gas jet is solved using the Navier-Stokes equations for low Reynolds number flows. Two distinct cases are studied dependent on whether high-molecular-weight surfactants are present or not. In the absence of high-molecular-weight surfactants the velocity profile in the gas is parabolic, whereas in the presence of surfactants the gas-liquid interface becomes rigidified giving rise to a flat velocity profile. In this latter case minimization of the dissipation energy is used to close the system of equations. For a very low gas-to-liquid flow rate ratio the bubble radius scales as $r_\mathrm{b}/R \propto \sqrt{Q_\mathrm{i}/Q_\mathrm{o}}$, independent of the inner-to-outer viscosity ratio and of the type of the velocity profile in the gas. However, in the case in which the gas velocity profile is parabolic and the viscosity ratio is sufficiently low the bubble radius scales as $r_\mathrm{b}/R \propto (Q_\mathrm{i}/Q_\mathrm{o})^\beta$, with β smaller than 1/2, as is shown in Fig. 5.4 on page 67.

Finally, in *Chapter 6*, droplet formation from the breakup of a liquid microjet emanating from a circular nozzle is investigated both experimentally using ultra high-speed imaging and numerically within a lubrication approximation model. A liquid emanating from a nozzle at sufficiently large velocity forms a jet that is inherently unstable and spontaneously breaks up into droplets to minimize its surface energy. In the analyzed low Reynolds number regime the jet breakup is driven by surface tension forces only. The breakup mechanism in this regime is referred to as "Rayleigh breakup" and the relevant time scale is given by the capillary time $\tau_\mathrm{c} = \sqrt{\rho r^3/\gamma}$, with liquid density ρ, surface tension γ, and radius of the jet r. Here, the dynamics of the breakup of a 18.5 μm jet into droplets is resolved at high spatial and temporal resolution, such that the smallest structures such as the satellite droplets can be studied in great detail. The behavior of the liquid during breakup and beyond using is numerically studied using a one-dimensional model that is based on the lubrication approximation. In Fig. 6.5 on page 88 a direct comparison between the experimental results and those obtained using the lubrication approximation model is shown. In spite of its limitations the one-dimensional lubrication approximation model predicts the

formation of the microdroplets and satellite droplets and their sizes with great accuracy. Moreover, it offers fast computational methods that make it possible to perform parameter studies in which the influence of, for example, liquid viscosity and jet velocity on the formation of satellite droplets can be investigated (see Fig. 6.13 on page 96). A further study was carried out to compare the numerics to experimental data. This was done at the experimental limit using the Brandaris 128 for ultra high-speed imaging to visualize the breakup of a 1 μm diminutive jet at 14 Mfps. The high-speed imaging results and those from the model calculation agree perfectly, confirming that the "standard" dimensionless analysis indeed carries on down to the microscale.

The thesis ends with a general conclusion and outlook in *Chapter 7*.

Samenvatting

De vorming van microscopisch kleine druppels en bellen met een nauwkeurig bepaalde grootte is essentieel in een groot aantal producten en toepassingen. Bijvoorbeeld in medische toepassingen, zoals diagnostische echoscopie of locale medicijntoediening, maar ook in inkjettechnologie, cosmetische producten en in de moderne levensmiddelenindustrie. De typische grootte van de druppels en bellen die in dit proefschrift bestudeerd worden, is 10 μm (ter vergelijking, de dikte van een haar is ongeveer 100 μm) en de typische tijdschaal van het vormingsproces is in de orde van enkele microseconden of minder. Wanneer een druppel of bel afbreekt van haar bron, wordt de tijd- en lengteschaal nog veel kleiner. Om het laatste moment van de druppelvorming vast te leggen, is daarom gebruik gemaakt van een ultrahogesnelheidscamera. Dit proefschrift beschrijft experimenteel en numeriek onderzoek naar diverse aspecten van druppel- en belformatie in verschillende microfluïdische systemen.

In *Hoofdstuk 1* wordt een algemene introductie van de historische ontwikkeling van het onderzoek naar druppel- en belformatie gegeven.

In *Hoofdstuk 2* wordt de invloed van de kanaalafmetingen van het "flow-focusing" apparaat op de belformatie bestudeerd. Het is experimenteel aangetoond dat de aspect ratio van het kanaal $\mathrm{AR} = H/W$, waarbij H en W respectievelijk de hoogte en breedte van het kanaal zijn, sterk de dynamica van de belformatie beïnvloedt. Voor een kanaal waarbij de hoogte veel kleiner is dan de breedte ($H \ll W$), zijn twee verschillende regimes te onderscheiden in het opbreken van de bel, zoals te zien is in Fig. 2.3 op pagina 13. In de eerste fase, waarin de nek sterk ingeklemd is door de boven- en onderzijde van het kanaal, wordt de nek in de zijdelingse richting samengeknepen door de vloeistofstroom. Zodra de nek dunner is dan de hoogte van het kanaal, begint de nek zeer snel in radiale richting in te snoeren, wat uiteindelijk resulteert in het ontstaan van een bel. In deze laatste fase van het opbreken van de nek is gemeten dat de relatie tussen

de minimale radius van de nek (r_m) en de tijd tot het moment van opbreken (τ), wordt gegeven door een power law, met $r_\mathrm{m} \propto \tau^{1/3}$. Bovendien is door middel van een stabiliteitsanalyse aangetoond dat een ingeklemde quasi tweedimensionale nek ongevoelig is voor kleine verstoringen aan het gas-vloeistof oppervlak, terwijl een vrije jet juist altijd onstabiel is. Een willekeurige verstoring leidt dan meteen tot het opbreken van de nek. Deze laatste fase in het opbreken, is een ongecontroleerd proces en geeft daarom meer onregelmatigheden in de belformatie. Microbellen met een smalle grootteverdeling worden bij voorkeur gemaakt in kanalen met een lage aspect ratio ($H \ll W$), terwijl een hoge bellenproductie bereikt wordt in kanalen met een vierkante dwarsdoorsnede.

Het 1/3 power law gedrag dat gemeten is tijdens de laatste fase van het afbreken van de bel, kan mogelijk worden verklaard door een sterk toenemende gassnelheid door de nek. In *Hoofdstuk 3* wordt daarom deze laatste fase in meer detail bestudeerd door middel van hogesnelheidsvideografie met een snelheid van 1 miljoen beelden per seconde (Mbps), zodat de singulariteit tot op $1\,\mu$s benaderd kan worden. Het wijde gezichtsveld van de camera maakt het mogelijk om de volledige groei van de bel te filmen, inclusief de verandering van de radiale en axiale lengte van de nek. Door analyse van deze beelden is de snelheid van het gas te berekenen. Hieruit blijkt dat tijdens het opbreken van de bel de in eerste instantie lage gassnelheid van richting verandert en geleidelijk versnelt, totdat een maximale snelheid bereikt wordt ($u \approx 23\,\mathrm{m/s}$) op het laatste moment van opbreken. Ondanks de sterke versnelling speelt de massatraagheid van het gas een verwaarloosbare rol tijdens het gehele opbreekproces. De verandering van de radiale en axiale lengteschaal van de nek is daarentegen wel belangrijk. In Fig. 3.5 op pagina 30 is te zien dat de axiale lengteschaal sneller kleiner wordt dan de radiale lengteschaal. Dit betekent dat de nek steeds minder slank wordt in de loop van het opbreekproces. Dit geeft het opbreken een driedimensionaal karakter, waarbij de vloeistof sferisch in de richting van de opbrekende nek stroomt. Door de insnoering van de nek te beschrijven met de Rayleigh-Plesset vergelijking voor een sferisch caviterende bel is te zien dat de nek moet schalen volgens $r_\mathrm{m} \propto \tau^{2/5}$. De exponent komt verbazend goed overeen met de gemeten waarde van 0.41 ± 0.01.

In *Hoofdstuk 4* is een microfluïdisch "co-flow" apparaat gebruikt om bellen te maken met een diameter d_b die aanzienlijk kleiner is dan de breedte van het kanaal waarin ze worden gevormd, namelijk $d_\mathrm{b}/W < 0.1$. Het apparaat wordt op een nieuwe manier gebruikt, waarbij een

sterke drukgradiënt in het kanaal ontstaat. Hierin ontwikkelt zich een gasvormige draad die opbreekt in bellen met een gecontroleerde grootte. Deze wordt voorspeld door een schalingstheorie, waarbij de diameter van de bel $d_\mathrm{b}/W \propto (\mu_\mathrm{g}/\mu_\mathrm{l})^{1/12}\,(Q_\mathrm{g}/Q_\mathrm{l})^{5/12}$, met μ_g en μ_l de viscositeit van respectievelijk het gas en de vloeistof en Q_g en Q_l het gas- en vloeistofdebiet. Fig. 4.2 op pagina 45 laat deze nieuwe manier van microbelformatie zien voor verschillende verhoudingen tussen het gas- en vloeistofdebiet. Onder de juiste condities is het mogelijk om microbellen te produceren die kleiner zijn dan $5\,\mu$m in een kanaal van wel $50\,\mu$m met een productieaantal van meer dan 10^5 bellen/s. Dit is een grote verbetering voor industriële toepassingen waarbij een hoge productie en een kleine kans op verstopping van de microkanalen belangrijk is.

In *Hoofdstuk 5* is een theoretische beschrijving gegeven van bellen die gevormd zijn door het opbreken van een gasvormige draad, omringd door een meestromende vloeistof. De grootte van deze bellen wordt bepaald door de straal van de binnenste gasdraad en de frequentie waarin deze draad opbreekt in bellen en is dus volledig afhankelijk van de regelparameters van het "co-flow" apparaat. De grootte van de gasdraad wordt bepaald door gebruik te maken van de Navier-Stokes-vergelijkingen voor stromingen met kleine Reynoldsgetallen. Twee verschillende situaties waarbij er wel of geen oppervlakteactieve stoffen met een hoog molecuulgewicht aanwezig zijn, worden bestudeerd. Als er geen oppervlakteactieve stoffen aanwezig zijn, is het snelheidsprofiel in het gas parabolisch. Wanneer deze stoffen wel aanwezig zijn, krijgt het gas-vloeistof oppervlak een star karakter en dit geeft een vlak snelheidsprofiel. In dit laatste geval wordt gebruik gemaakt van minimalisering van de dissipatie-energie om het stelsel van vergelijkingen op te lossen. Voor een kleine verhouding tussen het gas- en vloeistofdebiet schaalt de radius van de bel met $r_\mathrm{b}/R \propto \sqrt{Q_\mathrm{i}/Q_\mathrm{o}}$ onafhankelijk van de viscositeitsratio en het type snelheidsprofiel in het gas. Echter, in het geval dat het snelheidsprofiel in het gas parabolisch is en de viscositeitsratio voldoende klein, dan schaalt de radius van de bel als $r_\mathrm{b}/R \propto (Q_\mathrm{i}/Q_\mathrm{o})^{\beta}$, met β kleiner dan $1/2$, zoals is te zien in Fig. 5.4 op pagina 67.

Tenslotte wordt in *Hoofdstuk 6* het opbreken van een microscopisch kleine vloeistofstraal in lucht experimenteel onderzocht door middel van hogesnelheidsvideografie. Een vloeistof die met voldoende snelheid uit een opening stroomt, vormt een straal die van zichzelf onstabiel is en spontaan opbreekt in druppels, om zo de oppervlakte-energie te minimaliseren. In het geanalyseerde regime, waarbij de Reynoldsgetallen laag zijn, is het

opbreken van de straal volledig gedreven door oppervlaktespanning. Dit opbreekmechanisme wordt "Rayleigh breakup" genoemd, waarvoor geldt dat de tijdschaal gegeven wordt door de capillaire tijd $\tau_c = \sqrt{\rho r^3/\gamma}$, met ρ de dichtheid van de vloeistof, γ de oppervlaktespanning en r de radius van de vloeistofstraal. In deze studie is de dynamica van de vorming van microdruppels door middel van het opbreken van een 18.5 μm vloeistofstraal gevisualiseerd bij een hoge ruimtelijke en temporele resolutie, zodat zelfs de kleinste structuren zichtbaar gemaakt kunnen worden. Deze manier van druppelvorming wordt bovendien numeriek beschreven door middel van een eendimensionaal model gebaseerd op de lubricatiebenadering. In Fig. 6.5 op pagina 88 worden deze numeriek verkregen resultaten één op één vergeleken met de beelden van de hogesnelheidsopname. Ondanks de beperkingen van een eendimensionale numerieke benadering, is het model in staat om de primaire druppels en de satellietdruppels en hun grootte met grote nauwkeurigheid te voorspellen. Bovendien biedt het model een snelle berekeningsmethode die het mogelijk maakt om uitgebreide parameterstudies uit te voeren, bijvoorbeeld om de invloed van de viscositeit en de vloeistofsnelheid op de mogelijke vorming van satellietdruppels te onderzoeken (zie Fig. 6.13 op pagina 96). Een nadere studie is uitgevoerd om de numerieke berekeningen verder te toetsen aan experimentele resultaten voor de vorming van nog kleinere druppels. Onder deze zeer moeilijke experimentele omstandigheden is het nog net mogelijk om de druppelvorming uit een 1 μm dikke waterstraal zichtbaar te maken bij 14 Mbps. Het model komt ook goed overeen met deze hogesnelheidsopname, dat bevestigt dat de "standaard" dimensieloze analyse geldig blijft tot op de microschaal.

Dit proefschrift eindigt met een algemene conclusie in *Hoofdstuk 7*.

Acknowledgement

Many people were involved in the process of completing this thesis, academically or otherwise. Since this thesis is based on fluid dynamics and microfluidic devices it seems suitable to categorize my thanks accordingly.

The microfluidic lab. – The research described in this thesis has been carried out in the Physics of Fluids group of the Faculty of Science and Technology of the University of Twente. It has been made possible by the financial support of the MicroNed technology program of the Dutch Ministry of Economic Affairs through its agency SenterNovem, and by the Netherlands Organisation for Scientific Research (NWO) via the Spinoza Prize awarded to prof. dr. Detlef Lohse in 2005. I gratefully acknowledge the financially support from these organizations that allowed the building of such an excellent research environment.

Flow-focusing. – I would like to thank my supervisor prof. dr. Detlef Lohse and my assistant-supervisor dr. Michel Versluis for giving me the opportunity to work with a great group of excellent and enthusiastic people within PoF. Detlef, your ambitious, determined, and dedicated nature helped drive me to achieve my goals. I would particularly like to thank you for always being there, including midnight meetings when necessary. Michel, your skills to see the essential parts and ability to listen brought structure to my research and made sure that I was always heading in the right direction. Another important person that gave my Ph.D. a flying start was Benjamin Dollet. Your enthusiastic and stimulating discussions have always been very helpful, thank you for being a good friend. I am honored that Leen van Wijngaarden will be the chairman of my Ph.D. committee. Further I would like to thank Jacco Snoeijer, Deveraj van der Meer, Chao Sun, Gerrit de Bruin, and Andrea Prosperetti for both useful and fun discussions that guided me through. Thank you all for focusing my research into creating this thesis.

High-speed cameras. – I highly appreciate the skillful technical assistance and the careful eye for detail of Gert-Wim Bruggert, Martin Bos, and Bas Benschop. For each experimental challenge I posed you always resolved the problem fast and efficiently. I would like to thank Joanita Leferink for all the administrative work throughout the years, your ability to organize and find solutions is invaluable. Wietze Nijdam (Medspray), Hao Gu, David Fernandez Rivas, and Lingling Shui, thank you all for the patient supply of spray nozzles, masks, microfluidic devices, and technical advice on fabrication methods. David, thanks for the passionate insights into Cuba.

Co-flowing stream. – Without the excellent contributions and enthusiasm of many people this thesis would not have been possible. These people, whom I worked alongside, made the research flow in the right direction. I would like to thank, in no particular order, Benjamin Dollet, Jan-Paul Raven, Philippe Marmottant, Stephan Gekle, Michael Brenner, Theo Driessen, Roger Jeurissen, Jos de Jong, Lingling Shui, Volkert van Steijn, Albert Poortinga (Friesland Campina), Herman Wijshoff and Hans Reinten (Océ), Jeroen Wissink, Wietze Nijdam, Iwan Heskamp, and Wilbur de Kruijf (Medspray). Wilbur, thank you for your help on the cover illustration. I would also like to thank José Gordillo for sharing his broad knowledge of published research and deep understanding of its physics with me. Elena de Castro, it was a pleasure working with you fighting the many hours of frustrations in the lab. Outside the lab I enjoyed the cultural exchange of you learning to cope with cold wet Enschede and your guidance around sunny warm Sevilla. I am grateful to Arjan van der Bos, my long-term lab comrade, for his constructive ideas and all the good laughs. Furthermore I would like to thank Álvaro Marín for our fun times in the lab and Spanish translations when they were most crucial.

Satellite droplets. – The extra's that come with a Ph.D. include teaching and working with students. The ones I worked closely with and would like to thank are Anne Maas, Jarich van der Molen, Hans Kroes, Diederik Keij, Pascal Sleutel, Tim Segers and Vincent Kamphorst.

The surfactants. – Friends and colleagues who are always around to reduce the pressure. I would like to thank all my past and present colleagues for making working in PoF so enjoyable. Special thanks to Arjan van der Bos & Marlies Overvelde, Hanneke Bleumink, Bram Borkent, Elena de Castro, Rory Dijkink & Anja Eijk, Benjamin Dollet, Peter Eshuis, Valeria

Garbin, Erik Gelderblom & Lonneke Griep, Henk-Jan van Gerner, Kristján Gudmundsson, Tess Homan, Sylvain Joubaud, Álvaro Marín, James Seddon, Jeroen Sijl, Laura Stricker, Chao & Vivian Sun, Peichun Amy Tsai, Koen Winkels, and Aaldert Zijlstra. I would also like to say thank you to all my friends outside of work, in particular for the sailing trips, food, beer drinking, cycling and holidays that helped me through this all. Thanks mostly to Cees Maris, Sander Brouwer, Claas Willem Visser, Harmen Stormink, Jenneke Jonk, Maarten & Marjon van Zalk, and Johan & Hesther Hemssems. And, of course, my good friends and former housemates at Primer Plato and De Kadullen.

Pinch-off. – Ik wil mijn beide paranimfen bedanken voor hun hulp en steun tijdens de verdediging van mijn proefschrift. Claas Willem, ik wens je heel veel succes en vooral plezier tijdens jouw promotie. Bedankt dat jij mijn paranimf wilt zijn. Suzanne, mijn enige zus, ik kan mijn promotieverdediging niet anders voorstellen dan met jou aan mijn zijde. Dankjewel voor alles wat je voor mij betekent. Tom, bedankt voor je betrokkenheid, jouw hartelijkheid maakt je een belangrijk deel van de familie. In het bijzonder wil ik mijn ouders, Johan en Lia, bedanken voor alle liefde en aanmoediging die ze mij van het begin af aan gegeven hebben. Zonder jullie zou ik dit nooit hebben kunnen doen. Ten slotte wil ik Katharine bedanken voor haar grote steun, liefde en begrip bij het afronden van dit proefschrift. Dit is mijn *'t Ruischt alomme.*

Wim van Hoeve
Enschede, March 2011

About the author

Wim van Hoeve was born on the 27th April 1980 in Noordoostpolder, The Netherlands. He received his high school education at Emelwerda College in Emmeloord and graduated in 1999. In the same year he started studying Applied Physics at the University of Twente in Enschede. During this period he did a numerical study on heat transport in oxygen sensors as part of a three months internship at Robert Bosch GmbH in Stuttgart, Germany. Besides studying Applied Physics, Wim also completed a minor program at the International Institute for Geo-Information Science and Earth Observation in Enschede and was an active member of university life including participating on the boards of Alpha and P.K.v.V. Fact. In December 2006, he obtained his MSc. degree at the Physics of Fluids group, where he studied monodisperse microbubble formation in microfluidic flow-focusing devices. Afterwards, he continued his research as a Ph.D. student within the same group under the supervision of prof. dr. Detlef Lohse and dr. Michel Versluis. In August 2008 he received the IUTAM Young Researcher Award in Fluid Mechanics at the 22nd International Congress of Theoretical and Applied Mechanics in Adelaide, Australia.

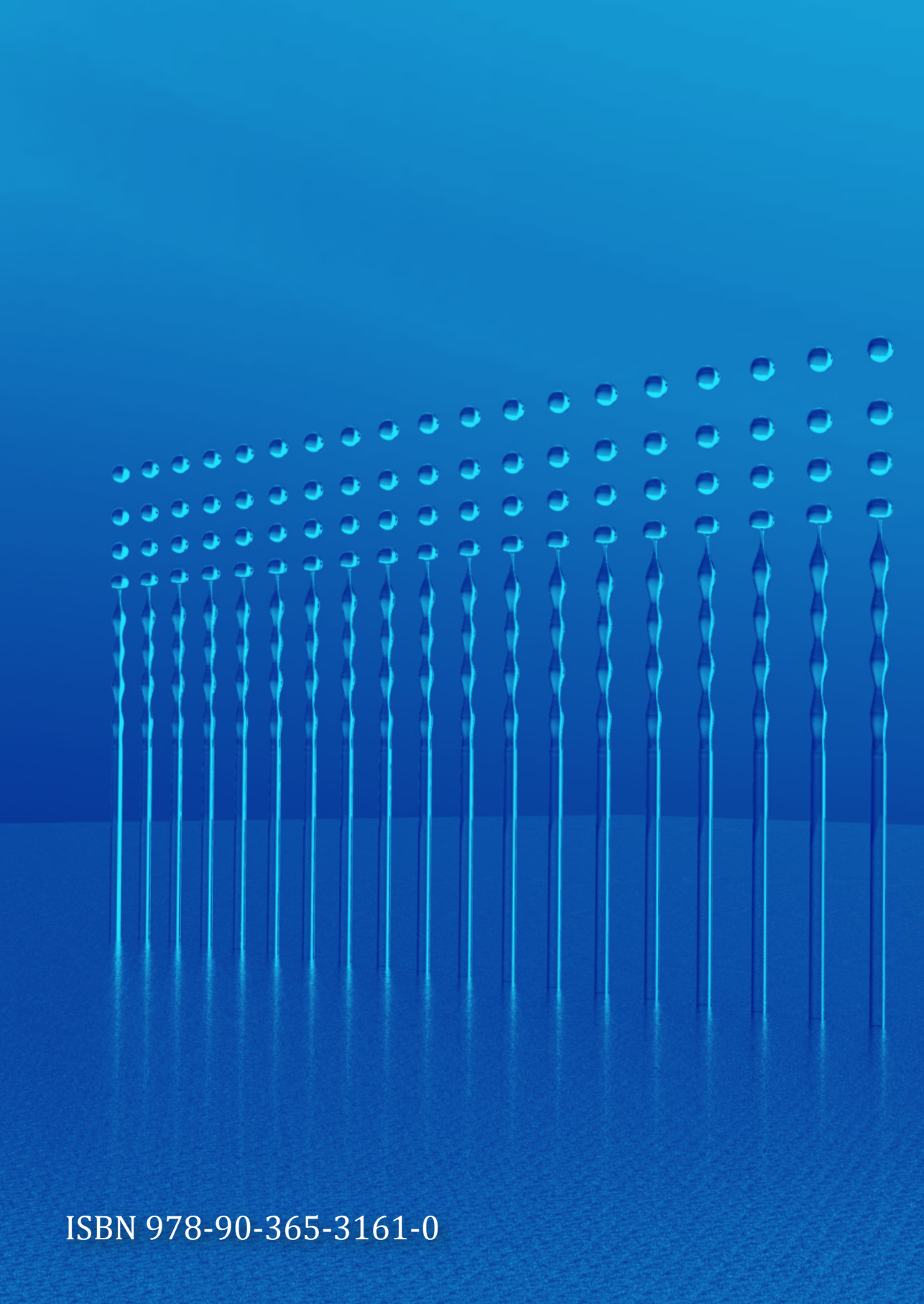

ISBN 978-90-365-3161-0